CZECH TECHNICAL UNIVERSITY IN PRAGUE

FACULTY OF NUCLEAR SCIENCES AND PHYSICAL ENGINEERING

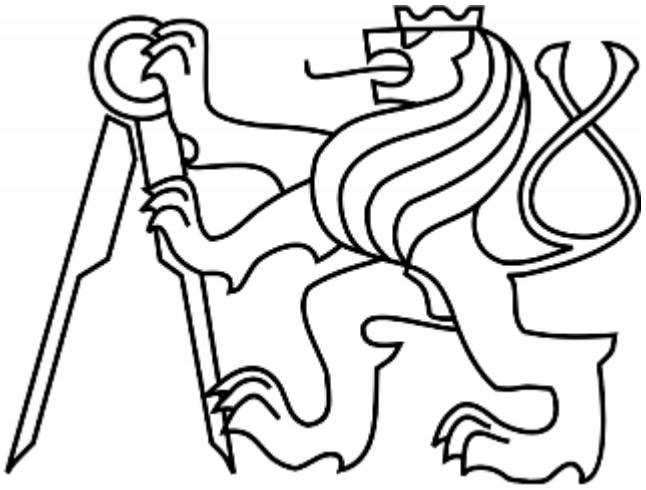

DOCTORAL THESIS

Design Study and Optimization of Irradiation Facilities for Detector and Accelerator Equipment Testing in the SPS North Area at CERN

Prague 2016 **Bartoloměj Biskup**

Bibliografický záznam

Autor	Bartoloměj Biskup České vysoké učení technické v Praze Fakulta jaderná a fyzikálně inženýrská Katedra dozimetrie a aplikace ionizujícího záření
Název práce	Návrh a optimalizace ozařovacích pracovišť pro testování detektorů a zařízení urychlovačů v Severní oblasti SPS v CERN
Studijní program	Aplikace přírodních věd
Studijní obor	Jaderné inženýrství
Školitel	Doc. Ing. Ivan Štekl, CSc. České vysoké učení technické v Praze Ústav technické a experimentální fyziky
Školitel specialista	Dr. Ilias Efthymiopoulos CERN, Švýcarsko
Akademický rok	2015/2016
Počet stran	112
Klíčová slova	FLUKA; ozařovací oblasti; fluence vysokoenergetických hadronů; fluence tepelných neutronů; dávka; Si 1 MeV neutronová ekvivalentní fluence; kalibrování radiačních polí; RadMon; BLM; testování detektorů; testování zařízení LHC; Medipix; Timepix

Bibliographic Entry

Author	Bartoloměj Biskup Czech Technical University in Prague Faculty of Nuclear Sciences and Physical Engineering Department of Dosimetry and Application of Ionizing Radiation
Title of Dissertation	Design Study and Optimization of Irradiation Facilities for Detector and Accelerator Equipment Testing in the SPS North Area at CERN
Degree Programme	Application of Natural Sciences
Field of Study	Nuclear Engineering
Supervisor	Doc. Ing. Ivan Štekl, CSc. Czech Technical University in Prague Institute of Experimental and Applied Physics
Supervisor specialist	Dr. Ilias Efthymiopoulos CERN, Switzerland
Academic Year	2015/2016
Number of Pages	112
Keywords	FLUKA; Irradiation Facilities; High Energy Hadron Fluence; Thermal Neutron Fluence; Dose; Si 1 MeV Neutron Equivalent Fluence; Mixed-Field Calibration; RadMon; BLM; Detector testing; LHC equipment testing; Medipix; Timepix

Abstract

Due to increasing performance of LHC during the last years, the strong need of new detector and electronic equipment test areas at CERN appeared from user communities. This thesis reports on two test facilities: GIF++ and H4IRRAD. GIF++, an upgrade of GIF facility, is a combined high-intensity gamma and particle beam irradiation facility for testing detectors for LHC. It combines a high-rate ^{137}Cs source, providing photons with energy of 662 keV, together with the high-energy secondary particle beam from SPS. H4IRRAD is a new mixed-field irradiation area, designed for testing LHC electronic equipment for radiation damage effects. In particular, large volume assemblies such as full electronic racks of high current power converters can be tested. The area uses alternatively an attenuated primary 400 GeV/c proton beam from SPS, or a secondary, mainly proton, beam of 280 GeV/c directed towards a copper target. Different shielding layers are used to reproduce a radiation field similar to the LHC “tunnel” and “shielded” areas in test zones around the target. In the first part of the thesis, the motivation for creating these two facilities along with an outline of the radiation damage effects on detectors and electronics is presented. An overview of similar facilities follows. In the next sections a detailed specification of the two facilities is given with emphasis on the description of the FLUKA Monte Carlo design and optimization studies. The commissioning and operation of the H4IRRAD facility is described next together with benchmark comparison between FLUKA simulations and measurements with beam. As a last part, the Medipix/Timepix detector measurement in H4IRRAD and its comparison with the Monte Carlo prediction are presented.

Abstrakt

Kvůli zvyšujícímu se výkonu LHC v průběhu posledních let se mezi uživateli v CERN objevila potřeba nových pracovišť pro testování detektorů a elektronických zařízení. Tato disertace pojednává o dvou takových pracovištích: GIF++ a H4IRRAD. GIF++, upgrade pracoviště GIF, je ozařovací oblastí pro testování detektorů pro LHC. Kombinuje gama zdroj ^{137}Cs s vysokou intensitou fotonů o energii 662 keV a sekundární svazek vysokoenergetických částic z SPS. H4IRRAD je nová ozařovací oblast pro testování elektronických, zejména velkých zařízení používaných v LHC, jako jsou např. vysokoproudové měniče výkonu. Toto pracoviště využívá radiačních polí tvořených interakcí zeslabeného primárního svazku protonů o hybnosti 400 GeV/c, nebo alternativně sekundárního svazku převážně protonů o hybnosti 280 GeV/c z SPS s měděným terčem. Různé vrstvy stínění pomáhají v testovacích zónách kolem terče vytvořit radiační pole podobné typickým polím v tunelu a stíněných oblastech LHC. První část disertace čtenáře seznamuje s motivací k vytvoření těchto dvou pracovišť spolu s přehledem možných radiačních poškození detektorů a elektroniky. Následuje výčet podobných pracovišť. V další kapitole je podána detailní specifikace dvou oblastí s důrazem na optimalizační studie provedené Monte Carlo kódem FLUKA. Následně je popsáno uvedení do provozu a samotný provoz oblasti H4IRRAD společně se srovnáním výsledků simulací a naměřených hodnot. Jako poslední jsou prezentovány výsledky měření v H4IRRAD s detektory Medipix/Timepix a jejich srovnání s hodnotami simulovanými metodou Monte Carlo.

Acknowledgement

I would like to express my gratitude to my supervisors Dr. Ilias Efthymiopoulos and Doc. Ing. Ivan Štekl, CSc. for their continuous guidance, encouragement and support during my PhD work.

Additionally, I am grateful to the Institute of Experimental and Applied Physics, especially to our former director Prof. Ing. Stanislav Pospíšil, DrSc, to the Department of Dosimetry and Application of Ionizing Radiation, CTU in Prague, and to CERN EN/MEF department for their not only financial support, but also for the opportunity to work within a professional environment on very interesting subjects.

I would also like to thank to all my colleagues, especially to Nikolaos Charitonidis and Ole Martin Hansen for long fruitful discussions about physics.

In particular, I give special thanks to my parents, brothers and sisters for their support throughout my studies.

Contents

Introduction

The operation of the Large Hadron Collider (LHC) since 2008 has proven to be highly successful, with a relatively high uptime for physics. This achievement has nevertheless been accompanied by system and control failures of the electronic equipment along the LHC tunnel due to radiation, mainly in the form of Single Event Effects (SEE). However, going further and with increased machine luminosity, the subsequent risk from the failures of equipment due to the integrated radiation has to be minimized. The lack of experimental data concerning these radiation-induced failures on specific and mostly commercial equipment required the existence of a dedicated facility where such studies can be performed in a well-controlled environment and in a sufficiently short time schedule. At the same time, the operation of LHC particle detectors is characterized by permanent high hit rate. Therefore, a precise understanding of possible ageing of detector materials under sustained particle bombardment and a detailed knowledge of the performance of detectors under high particle fluxes are crucial for their design optimization and efficient operation mode.

For the purpose of detector testing, the Gamma Irradiation Facility (GIF) [1, 2] was built in the CERN SPS West Area already in 1997. It combined irradiation by a high-rate ^{137}Cs gamma source together with the availability of a secondary particle beam from SPS. This facility has been used extensively for many years and the gamma irradiation part has been continued even after the SPS beam lines were decommissioned from the West Area in 2004. However, there has been a need for a stronger gamma source and for regaining the possibility to carry out simultaneous detector performance tests with a high-energy particle beam. Due to CERN's obvious need for new irradiation infrastructures, the Working Group on Future Irradiation Facilities at CERN [3] was created in December 2007. As a part of its mandate, the Working Group has conducted a broad web-based enquiry on users needs for irradiation facilities at CERN. Among other future irradiation facilities, the enquiry included questions about gamma irradiations with and without a beam. As a result of the input from the users, implementation plans have been prepared for a future Gamma Irradiation Facility, called GIF++ [4], at the SPS H4 beam line in the North Experimental Area of CERN [5].

Given the large amount of electronics being installed in the LHC underground areas, a CERN wide project called R2E [6] (Radiation To Electronics) has been initiated in 2007 to quantify the danger of radiation-induced failures and to minimize all radiation-induced failures in the LHC. In particular, effort has been undertaken for identifying equipment which

allows LHC operation with a ‘Mean-Time Between Failures’ (MTBF) greater than or equal to one week for a peak luminosity of $2 \cdot 10^{34}$ $cm^{-2}s^{-1}$ and a yearly integrated luminosity of 50 fb^{-1}, but also taking into account the LHC performance expected after the High Luminosity upgrade (HL-LHC), therefore assuming a peak luminosity of $\sim 5 \cdot 10^{34}$ $cm^{-2}s^{-1}$ for a yearly integrated luminosity of up to 200 fb^{-1} [7]. At the first place it is crucial to perform irradiation tests to determine the failure cross-sections of specific LHC equipment due to different types of radiation. For this purpose only parasitic testing at CERN or facilities outside CERN were available. There was therefore a strong need for a new dedicated test area, especially for large volume assemblies such as full electronic racks of high current power converters. As a result of this need, a new test area, called H4IRRAD [8], was proposed and has been set up in the SPS H4-beamline in the North Experimental Area of CERN.

The original task of this thesis was to contribute to the design of two irradiation facilities, GIF++ and H4IRRAD, by performing Monte-Carlo studies. The purpose of these studies was to optimize the geometry of the facilities in order to maximize their performance according to the user community requests while maintaining their radiation safety. For the H4IRRAD facility also characterization of the radiation field during the operation was requested for the purpose of the radiation tests and benchmarks with detectors.

1. Radiation Damage Effects

The complicated radiation field in and around the LHC, including almost all kinds of particles, interacts with the LHC equipment and instrumentation by many different ways. This chapter will give an overview of the most important radiation effects, especially destructive, on particle detectors and electronic devices, without going deep into details.

1.1 Aging

Aging of gaseous particle detectors, a permanent degradation of operating characteristics under sustained irradiation, has been observed since the early development of Geiger and proportional counters and attributed to the formation of polymeric deposits in the avalanche processes. With the introduction of multiwire chambers in the 1970s, and their wide use in experiments operating at high rates, radiation-induced degradation became a common observation. Since the effect of aging has been and still remains the main limitation to the long-term use of gaseous detectors in high-rate experiments, it has been extensively studied during the past decades [9].

Aging phenomena is a very complex field of study. The causes of the gas detector degradation are varied and sometimes not fully understood. Studies performed under laboratory conditions have often offered irreproducible or only partial results, mainly because the contributions to the aging process are numerous and related to both gas mixture, detector design and used materials. Even a detector with a suitable non-polymerizing gas mixture can fail due to a gas contamination by reactive products created in the avalanche process, by outgassing of materials used in the detector assembly or in the gas system [10].

The observed appearance of local damages detected as self-sustained discharges, gradual loss of energy resolution, excessive currents and decrease and non-uniformity of the gas gain have been associated with the presence of layers on the detector electrodes (see Figure 1), induced by pollution by materials used in the gas system or chamber construction, impurities in the gas itself, or by the polymerization process caused by species produced in the avalanche. The main known mechanisms leading to the gaseous detector aging are following:

1. Formation of polymers in the avalanche plasma from the cloud of the gas filling ions and radicals. This process can be triggered or accelerated by pollutant molecules.

2. Direct gas pollutant deposition on the surface of electrodes and insulators due to electrostatic forces. The pollutants can originate in outgassed vapours from organic materials, from a reaction of some reactive gases incompatible with chamber materials and plumbing, or from structural changes induced by ionizing radiation. The new outgassed pollutants can promote polymerization.

3. Because of the species created around the wire in the avalanche process, some initially neutral gases can become reactive. New reactive species can also remove layers of some materials, causing mechanical damages of the detector and polluting the filling gas [11].

The probability of above mentioned mechanisms to occur depends on a large number of factors as gas flow, gas gain, the geometry and electric field configuration, presence of additives and many other parameters. It is therefore necessary to select proper detector materials and filling gas mixture and perform tests for the full-size detector assemblies [11].

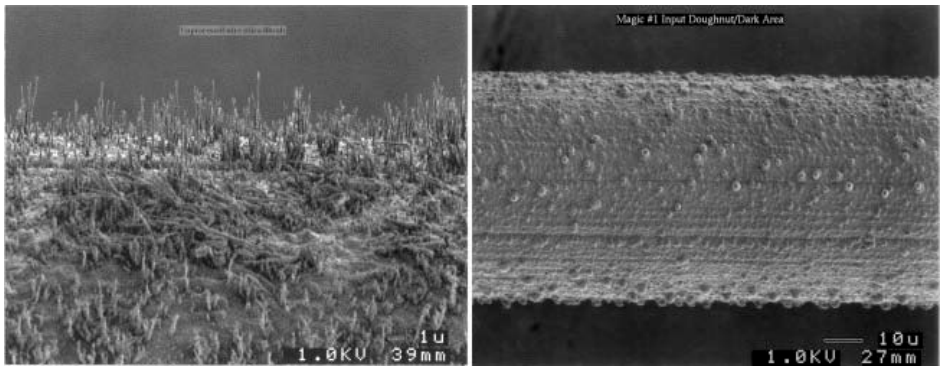

Figure 1: Examples of deposits on the electrode wires [12].

1.2 Radiation Effects on Electronics

There have been observed three different types of radiation damage on electronic components and systems exposed to a mixed radiation field. Damage from Total Ionizing Dose (TID) and Displacement Damage (DD) have cumulative nature, where the possible device failure is caused by the steady accumulation of defects, while so-called Single Event Effects (SEE) are stochastic and caused by a single high energy particle [7].

1.2.1 TID

This kind of damage is measured through total ionizing dose (i.e. energy absorbed locally in a medium due to ionization per unit mass) in Greys (Gy). The ionization radiation can create electron-hole pairs in the solids. The valence electrons excited to the conduction band are highly mobile in an electric field. Also the positively charged holes are mobile. As a

consequence, an electric conductivity of any solid (including insulators) is increased. A serious degradation of semiconductor device properties is caused by the production and subsequent trapping of the holes in its oxide films. This effect particularly strongly impacts the performance of metal–oxide–semiconductor (MOS) and bipolar devices. The electron-hole pair production ionization energy loss, E_p, depends primarily on the target material and is independent of the ionizing particle type. The number of created pairs depends on the energy of the ionizing radiation, but since the energy required to produce an electron-hole pair is relatively low (e.g. for SiO_2 only 18 eV), the energy of the ionizing radiation is not as qualitatively important (if higher than E_p) as for displacement damage. Therefore ionization effects caused by high energy particles can be simulated by lower energy beams of electrons, gamma of X-rays [13, 14].

Table 1: Effects on technologies susceptible to TID [15].

Technology category	Effects
MOS (metal oxide semiconductor) (NMOS; PMOS; CMOS; CMOS/SOS/SOI)	Threshold voltage shift Decrease in drive current Decrease in switching speed Increased leakage current
BJT (bipolar junction transistor)	h_{FE} (current gain of a bipolar transistor in common-emitter configuration) degradation, particularly for low-current conditions
JFET (junction field-effect transistor)	Enhanced source-drain leakage currents
Analogue microelectronics (general)	Changes in offset voltage and offset current Changes in bias-current Gain degradation
Digital microelectronics (general)	Enhanced transistor leakage Logic failure from (1) reduced gain (BJT), or (2) threshold voltage shift and reduced switching speeds (CMOS)
CCDs (charge-coupled devices)	Increased dark currents Effects on MOS transistor elements (described above) Some effects on CTE (charge transfer efficiency)
APS (active pixel sensor)	Changes to MOS-based circuitry of imager (as described above) – including changes in pixel amplifier gain
MEMS (micro-electromechanical structure)	Shift in response due to charge build-up in dielectric layers near to moving parts
Quartz resonant crystals	Frequency shifts
Optical materials (cover glasses; fibre optics; optical components, coatings, instruments and scintillators)	Increased absorption Variation in absorption spectrum (coloration)
Polymeric surfaces (generally only important for materials exterior to spacecraft)	Mechanical degradation Changes to dielectric properties

The insulator films used in solid-state electronic and optoelectronic devices as barriers to block charge motion between two layers of semiconductor or conductor can be affected by radiation by several ways. The most important effects are (a) temporary lowering the barrier; (b) producing a semi-permanent charge sheet by catching some charge travelling across the

oxide, which affects also conductivity of charge sensitive layers around it and (c) disturbing the interface bonds especially between insulator and semiconductor. These effects depend on many factors, including especially type of dielectric, trapping and excitation level, depth in the material and electric field. The depth of the charge capture is crucial for the degradation duration. The holes near the interface can be quickly annihilated by electrons. Electronic exchange is fast within an atomic bond length, while at the greater distances it is slower. Some degradations can be very long-lived (the trapped charge can be measured in the oxide even several decades after irradiation) [13].

An overview of the most important radiation effects on technologies susceptible to TID is given in Table 1.

1.2.2 DD

Displacement effect, also referred to as “bulk damage” or “non-ionizing energy loss” (NIEL) is a cumulative damage process caused by energetic particles colliding with atoms in crystal lattices and displacing them from their normal position, creating vacancies (unoccupied lattice sites) and interstitials (extra atoms inserted between the atoms occupying lattice sites). Both the interstitials and vacancies are mobile and can rearrange back (by annealing, i.e. the rearrangement of atoms or charges in a material with time after irradiation; usually activated thermally, sometimes even at room temperature and lower), but they can also react with impurities in the lattice or cluster together creating stable defect centres. The overall displacement damage results in a minority carrier lifetimes change in semiconductors, and coloration and increased light absorption in crystalline optical materials. The specific effects for particular technologies are listed in Table 2 [14, 15].

Table 2: Effects on technologies susceptible to displacement damage effects (for abbreviation meaning see Table 1) [15].

Technology category	Sub-category	Effects
General bipolar	BJT Integrated circuits	h_{FE} degradation in BJTs, particularly for low-current conditions (PNP devices more sensitive to DD than NPN)
	Diodes	Increased leakage current Increased forward voltage drop
Electro-optic sensors	CCDs	CTE degradation Increased dark current Increased hot spots Increased bright columns Random telegraph signals
	APS	Increased dark current Increased hot spots Random telegraph signals Reduced responsivity
	Photo diodes	Reduced photocurrents Increased dark currents
	Photo transistors	h_{FE} degradation Reduced responsivity Increased dark currents
Light-emitting diodes	LEDs (general)	Reduced light power output
	Laser diodes	Increased threshold current
Opto-couplers		Reduced current transfer ratio
Solar cells	Silicon GaAs, InP, etc.	Reduced short-circuit current Reduced open-circuit voltage Reduced maximum power
Optical materials	Alkali halides, Silica	Reduced transmission
Radiation detectors	Semiconductor γ-ray & X-ray detectors: Si, HPGe (high-purity germanium), CdTe, CZT (cadmium zinc telluride)	Reduced charge collection efficiency (calibration shifts, reduced resolution) Poorer timing characteristics HPGe shows complex variation with temperature
	Semiconductor charged-particle detectors	Reduced charge collection efficiency (calibration shifts, reduced resolution)

The NIEL is generally quantified through accumulated 1 MeV neutron equivalent fluence (Φ_{neq}) producing the same damage as an arbitrary beam with fluence Φ:

$$\Phi_{neq} = \kappa\Phi\,, \tag{1}$$

where κ is the hardness parameter defined as:

$$\kappa = \frac{EDK}{EDK(1MeV)}. \tag{2}$$

EDK is the energy spectrum averaged displacement KERMA:

$$EDK = \frac{\sum_i \int D_i(E)\phi_i(E)dE}{\sum_i \int \phi_i(E)dE}, \quad (3)$$

where $\Phi(E)$ is the differential flux and $D(E)$ is the displacement KERMA or the damage function for the energy E of the incident particle (for particle type i):

$$D_i(E) = \sum_k \sigma_k(E) \int dE_R \, f_k(E, E_R) P(E_R), \quad (4)$$

where σ_k is the cross section for reaction k, $f_k(E, E_R)$ is the probability density of the incident particle to produce a recoil of energy E_R in reaction k, and $P(E_R)$ is the partition function (the part of the recoil energy deposited in displacements). $EDK(1\ MeV)$ is equal to 95 MeV·mb [16].

The displacement damage function in silicon for different particles as a function of incident particle energy is displayed in Figure 2. The minimal neutron energy for displacement by elastic scattering is 190 eV. The damage cross section below this energy is caused by neutron capture resulting in a recoil energy from emitted gamma rays, of approximately 1 keV. This energy is much higher than the minimal displacement energy for silicon of about 25 eV. The nuclear reactions start to play an important role for neutrons in MeV range and above. The damage cross section for protons is much higher than for neutrons at lower energies due to domination of Coulomb interactions. For higher energies the Coulomb contribution becomes less important, while the dominating nuclear reactions in this range are comparable for protons and neutrons, therefore also the damage functions are similar. The pion damage function reaches values of about 2/3 of the neutron and proton ones for the high energies due to quark weighting factor and around a few hundred MeV is affected by a delta resonance [17].

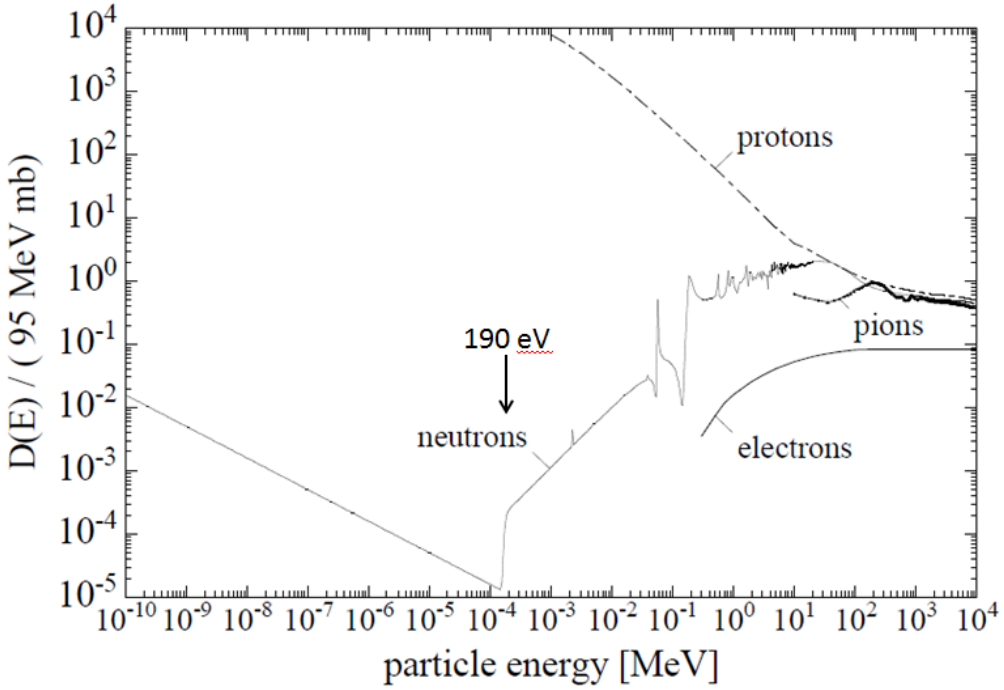

Figure 2: Displacement damage function *D(E)* in silicon for neutrons, protons, pions and electrons [17].

1.2.3 SEE

Single Event Effects (SEEs), as opposed to TID or DD with cumulative nature, are induced by the interaction of a single incident particle with electronic components. If the incident particle is a heavy ion, the process occurs by direct ionization, while for protons and neutrons, the effects are caused by secondary particles (recoils) created by nuclear interactions of the proton or neutron with an atom of the semiconductor die. The collected charge fraction liberated by the primary or secondary ionizing particle has to be larger than the electric charge stored on a sensitive node (a node in a circuit whose electrical potential can be modified by collection of electrical charges or by internal injection) to allow SEE. These effects become an increasing limitation of the reliability of electronic components, circuits, and systems, and have been extensively studied in recent years [18].

SEE phenomena can be divided into two subgroups: destructive and non-destructive. The effects, which have the potential to destroy the device, include Single Event Latch-up (SEL), Single Event Snapback (SESB), Single Event Gate Rupture (SEGR), Single Event Dielectric Rupture (SEDR), and Single Event Burnout (SEB). Non-destructive effects, which corrupt data or place the device in a different operational state, include Single Event Upset (SEU), Multiple-Cell Upset (MCU), Single-word Multiple-bit Upset (SMU), Single Event Functional Interrupt (SEFI), Single Event Hard Error (SEHE), Single Event Transient (SET), and Single Event Disturb (SED) [19].

The probability that SEE will occur is expressed as a cross-sectional area, measured in general through cm^2/device, but for SEUs, MCUs, and SMUs usually in cm^2/bit. The SEE cross section depends on incident particle species and its energy. However, for heavy ions, the cross section is often expressed as a function of linear energy transfer (LET), the amount of energy deposited in the track per unit pathlength, typically measured in MeV · cm^2/mg. The LET concept is not proper for very small sensitive devices and high energy particles, because different ions with the same LET can produce different charge distribution along the track and therefore different charge can be collected particularly in small devices [15, 19].

SEL is a destructive triggering of a real or parasitic PNPN thyristor structure in the device. Due to a latch-up the current increases and the device can be destroyed by thermal effects, if the power supply is not shut down quickly. This can be assured by use of a current monitoring and a power control circuit. Up to now, only CMOS and BiCMOS devices have been found to be susceptible to a latch-up [19].

SESB is also a destructive high-current mode SEE, similar to SEL, but occurs in single MOS transistor structures. If the field across the drain region is sufficiently high, the snapback can be triggered by a single high-energy particle. The parasitic bipolar transistor between the drain and the source of a MOS transistor amplifies avalanche current caused by the heavy ion, resulting in a very high current between the drain and source region, and subsequently causing localised heating. SESB affects SOI (Silicon On Insulator) devices and N-channel MOSFET structures [19].

SEGR is the formation of a conducting path in a high-field region of a gate oxide triggered by a single ionizing particle. **SEDR** is a similar effect but applies to dielectric generally e.g. in antifuses of FPGAs (Field-Programmable Gate Arrays). The electric field across the dielectric exceeds a critical value (breakdown voltage) due to a collection of the charges created by the heavy ion in the semiconductor and its propagation up to the insulator interface. The only way to protect a component is to use electrical conditions which prevent from the SEGR/SEDR to occur (i.e. derating). The sensitive devices include linear devices, capacitors with very thin gate oxide, N and P-channel power MOSFETs, non-volatile NMOS structures, high-density memories and ICs (Integrated Circuits) [19].

SEB is the destructive triggering of a vertical n-channel transistor which is accompanied by regenerative feedback. If a device, particularly N-channel Power MOSFET, BJT (Bipolar Junction Transistor) and IGBT (Insulated-Gate Bipolar Transistor), is biased in

the OFF state (a high drain source voltage is blocked), a heavy ion can deposit enough charge to turn the device on [19]. An example of a burnout MOSFET is given in Figure 3.

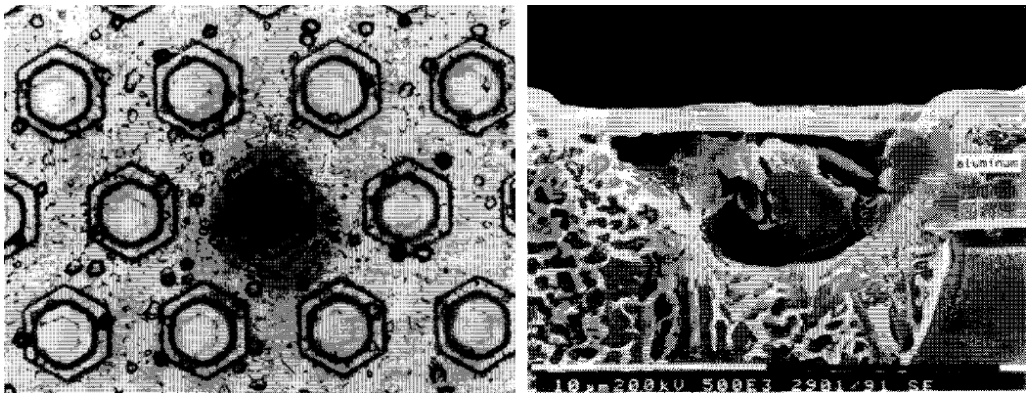

Figure 3: SEB on a surface of hex power MOSFET: optical view and 5000× magnified [20].

SEU is a single bit flip induced in a digital element by direct ionization or by recoil nucleus from a nuclear reaction, leading to a change of stored information. The element can be rewritten with the correct value and no damage is induced by SEU. It occurs in both VLSI (Very-Large-Scale Integration) logic devices and memory circuits and most of the technologies are sensitive to this effect (Si CMOS and bipolar, SOI and GaAs) [19].

During **MCU** two or more bits become corrupted by a primary or secondary particle. Physically adjacent corrupted bits are called clusters of errors. If the bits are logically related (word/bit line errors or several corrupted bits within a common word), we speak about **SMU**. MCU/SMU are characteristic for circuits sensitive to charge collection by diffusion, or charge sharing from a single ion, especially for high levels of integration (e.g. in DRAM/SRAM with complex operation modes) [19].

SEFI is a temporary non-functionality or interruption of normal operation of the affected device. It can last as long as the power is maintained or a reset is sent to resume the normal operation, because SEFI is not accompanied by a high current condition. This phenomenon affects complex devices with embedded state machine/control sections used in many modern memories (flash-EPROMs, EEPROM, DRAMs, SDRAMs), FPGAs, ADCs (Analog-to-Digital Converters), Processors, DSPs (Digital Signal Processors) [19].

SEHE (sometimes called a “stuck” bit error or hard fault) is an unalterable change of state that is associated with semi-permanent damage to a memory cell and is related to a micro-dose circuit effect. It can occur in resistive-load SRAM devices and DRAMs [19].

SET or **SED** is a momentary voltage spike (excursion) at a semiconductor node, formed by the electric field separation of the charge generated by an ion passing through or near a circuit junction. Depending on several factors, as a moment and place of a spike occurrence, it can have several consequences. If the spike is absorbed by local RC elements, it has no impact. It can be propagated up to at least one output of the component, or can be converted to an SEU when the signal reaches a latch. In some cases the signal perturbation can propagate through the whole system. All linear circuits (operational amplifiers, ADCs, comparators, voltage regulators, pulse-width modulators) are sensitive to SET. Due to a very low power used in photo-detector optical signals, opto-electronic devices (e.g. CCDs, IR arrays, opto-couplers, fibre-optic data links) are very sensitive. SEDs can also affect fully combinatorial logic devices (e.g. switches, logic gates, bus line drivers), clocks and PLLs (Phase-Locked Loops) and asynchronous control signals such as ASIC (Application-Specific Integrated Circuit), processors, memories or FPGAs [19].

Multiple Bit Upset (**MBU**) is a general term referring to the principle of a single strike causing corruption of several memory elements in memories and logic devices [21].

1.2.4 Radiation Effects in LHC

The mixed particle and energy field encountered in LHC is caused by particles generated by proton-proton or ion-ion collisions in the LHC experimental areas, distributed beam losses around the machine, and by beam interacting with the residual gas inside the beam pipe. The composition of the radiation field depends on the distance and on the angle with respect to the interaction point and on the potential presence and amount of shielding material. The LHC equipment failure probability depends not only on the radiation field but also on the device (used materials, architecture…). Since several areas close to the LHC tunnel (partly not sufficiently shielded) are equipped with commercial or not specifically designed electronics, the radiation levels in the LHC tunnel and in the shielded areas have been simulated and measured during the first years of LHC operation. During 2011, about 70 beam dumps were caused by radiation effects on electronic equipment resulting in a downtime for the machine of about 400 hours. The major cause of radiation-induced failures was confirmed to be due to SEEs. The most affected are the systems located close to the beam, like the beam instrumentation system, quench-protection, cryogenics and the ‘low-current’ power-converters, all critical to achieve the highest possible LHC operational efficiency [7].

2. Irradiation Facilities

There are many different irradiation test facilities all over the world, using wide range of radiation sources and dedicated to various purposes including both industrial, space, military and scientific research. Only few examples of test facilities used by CERN detector and electronics communities are presented in this chapter.

2.1 GIF

The Gamma Irradiation Facility (GIF) [2], also called X5 Irradiation Facility, is a test area dedicated to expose large area high-energy particle detectors to a high photon flux simulating their operational environment radiation background in the LHC experiments, with a possibility to simultaneously use a particle beam. The aim of the gamma irradiation is to study the detector performance and aging effects in the presence of high radiation background, while the particle beam allows calibration measurements with tracks. GIF was built in 1997 and is located downstream the final beam dump of the SPS X5-beamline in the West Experimental Area of CERN. The test zone is shielded by 8 m high and 80 cm thick concrete wall. The area layout is shown in Figure 4 [1, 2].

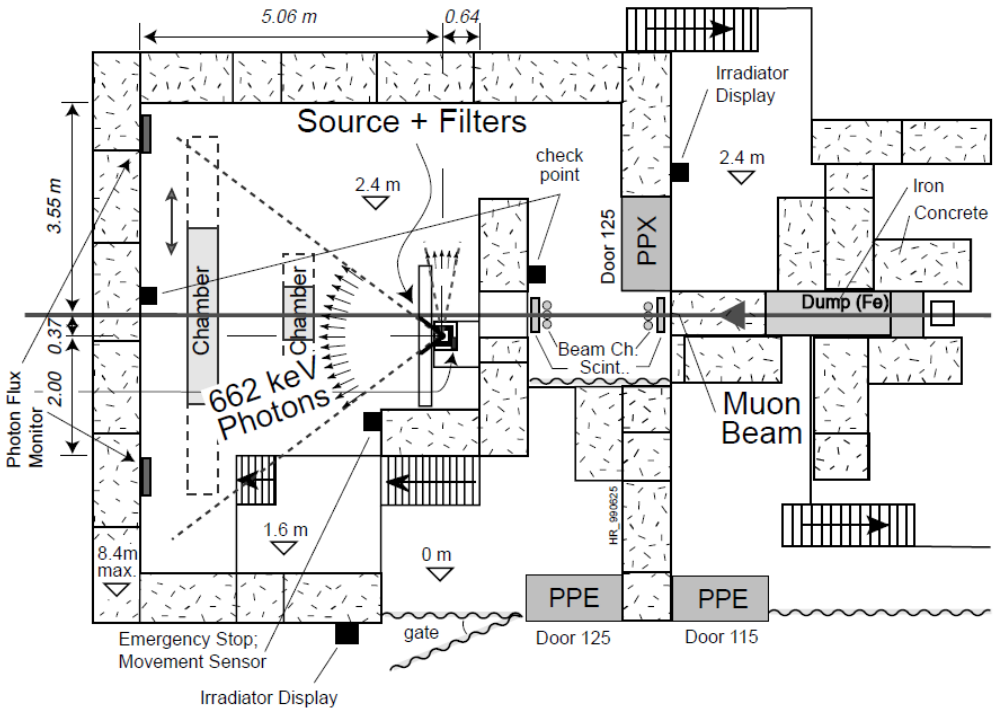

Figure 4: GIF schematic layout with the muon beam from the right side [1].

The gamma irradiator consists of a lead rectangular container with two precisely shaped collimator windows and the active element, a ^{137}Cs source with a half-life of 30 years

and activity of 740 GBq (measured in March 1997), which emits 662 keV photons with 85% emission probability. The main collimator window provides a pyramidal aperture of 74° × 74° solid angle, which permits irradiation of a 6 m^2 area at a maximum distance of 5 m from the source. The second irradiation area, defined by a smaller window of 22° × 22°, is available at 90° to the main axis and allows irradiation of smaller detectors, e.g. crystal calorimeters. A system of lead filters located directly behind the large irradiator collimator, provides an adjustable photon flux with the attenuation factor ranging from 1 to 10^4 [1].

The low intensity beam of high energy muons (during typical operation around 100 GeV) from SPS X5-beamline was available until 2004, when all beamlines were removed from the West Area. The area has been extensively used even after the beamline removal and provided useful feedback to the detector community. Nevertheless, there has been a strong need to regain the possibility to carry out simultaneous detector performance tests with a high-energy particle beam. Moreover a stronger gamma source is requested for the new generation of detector tests [1, 5].

2.2 PIF

The Proton Irradiation Facility (PIF) [22, 23] has been constructed as a part of the large research complex of the Paul Scherrer Institute (PSI) in Villigen, Switzerland, in cooperation between PSI and European Space Agency (ESA) in 1992. PIF uses a proton beam extracted from one of three PSI cyclotrons. Since this accelerator serves also facilities for cancer therapy, most of the tests are conducted during nightshifts or weekends [22, 23].

The PIF experimental set-up consists of the energy degrader, sample holder, beam collimation and monitoring devices and the run and data acquisition system (see Figure 5). The maximum allowed energy is 254 MeV, with the maximum flux of $2.5 \cdot 10^8$ $p \cdot cm^{-2} \cdot s^{-1}$, and can be decreased by PIF degrader down to 30 MeV. The maximum diameter of the irradiated area is 9 cm [22, 23].

The main disadvantages of PIF are the small beam size which limits also the size of tested component, low beam energy (in comparison with the LHC background environment), and the time schedule (weekends and nights). However, this facility remains eligible for both TID, DD and SEE tests of limited amount of small components and is used by CERN electronics community (see e.g. [24]).

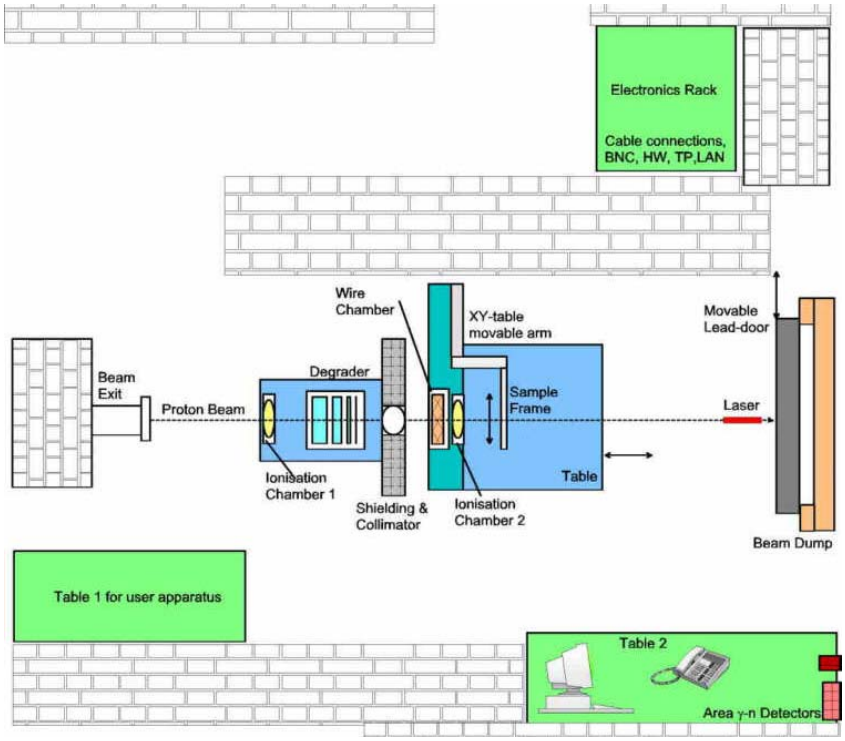

Figure 5: PIF schematic layout (not in scale) [23].

2.3 CEA Valduc

One of the nuclear research centres of Atomic Energy and Alternative Energies Commission (CEA) [25] is situated in Valduc, France. Apart from its military purposes, several facilities are also available for scientific research (via special agreement), including SAMES and ALVAREZ linear accelerators using D-D and D-T reactions, super prompt-critical reactor CALIBAN and PROSPERO [26] reactor (before the shut down in 2011 also SILENE pulsed reactor). Providing monoenergetic neutrons of 2.5 MeV and 14 MeV and broad spectrum from the reactors, these facilities are convenient for wide range of applications and research fields.

The PROSPERO air cooled reactor which operates in delayed critical state with a continuous and steady power is composed of an internal core made of High Enriched Uranium ^{235}U metal alloy, surrounded by a depleted uranium reflector (see Figure 6). The reactor is used as a fast neutron spectrum source with a possible power range varying from 3 mW to 3 kW and maximum temperature of the core of 200°. The mean energy of the leakage neutron spectrum is 0.8 MeV. The 10 m × 8 m × 6 m reactor cell, surrounded by 1.4 m thick concrete walls, offers a wide range of irradiation sites from the reflector surface to 6 m away from the reactor central axis. The flux at nominal power of 3 kW varies from 10^{7} n·cm^{-2}·s^{-1} at 5 meters from reactor axis to $5{\cdot}10^{10}$ n·cm^{-2}·s^{-1} at the reflector surface [26, 27].

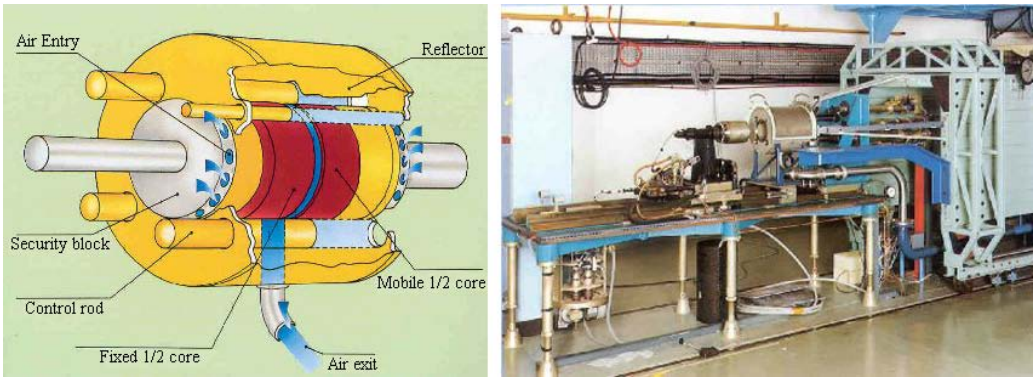

Figure 6: PROSPERO reactor assemblies [27].

This facility is suitable for displacement damage tests and has been used by CERN detector and electronics communities for the past years (see e.g. [28]). In 2009, the area usability was extended by addition of a hollow cubic box with 10 cm thick polyethylene (PE) sides, placed 1 m away from central reactor axis. This moderator is capable to thermalize the fast neutrons to energies below 0.6 eV, which brings new electronics test possibilities [27].

2.4 CNRAD

CNRAD (CNGS Radiation) [29] was a mixed field electronics test area, operating parasitically to the CNGS facility (CERN Neutrinos to Gran Sasso) [30]. CNGS used a 400 GeV/c proton beam extracted from the SPS in 10.5 µs short pulses of $2.4 \cdot 10^{13}$ protons per pulse. These two pulses, separated by 50 ms, repeated with a standard 6 s repetition cycle. The proton beam was transported through the TT41 transfer line to the CNGS target T40 which consisted of series of graphite rods, cooled by helium [30].

CNRAD was located in a large technical gallery parallel to the CNGS target station. The appropriate test locations were identified by FLUKA Monte Carlo code [32, 33] simulations and by measurements. Figure 7 gives an overview of the area together with the High Energy Hadron (HEH; E >20 MeV) fluence projection. The test area provided a stable mixed particle field with a high flux and the energy spectra comparable to the LHC ones [31].

CNRAD was eligible for both TID, DD and SEE tests of electronic components, including large volume assemblies. The main disadvantage remained the fact that the tests were parasitic, therefore the access conditions were problematic, usually only during technical stops (once per 3-6 weeks) with safety constrains. The access tunnel length of 1 km can cause problems with signals and makes cabling difficult. Also the access to cooling water, necessary for some types of equipment, was missing. CNGS operation stopped in 2012. Hence, the possibility to test the equipment in CNRAD is not available anymore.

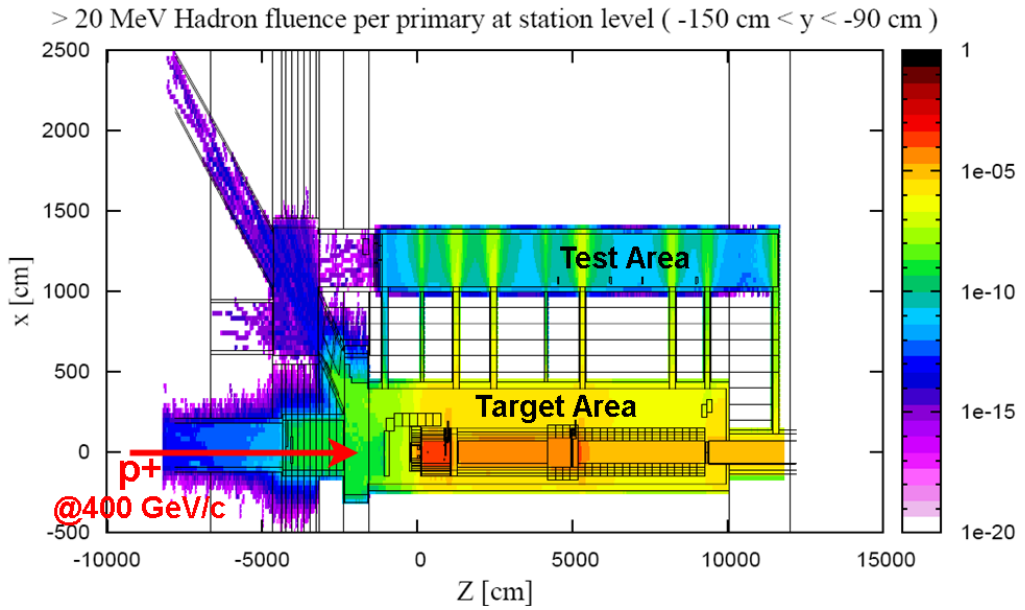

Figure 7: Horizontal layout of CNGS and CNRAD area with simulated High Energy Hadron fluence per proton on CNGS target [31].

3. Software Tools

The Monte Carlo tools have been used extensively for the studies presented in this thesis. This chapter describes the Monte Carlo codes and the most important software tools employed.

3.1 FLUKA

The FLUKA Monte Carlo code [32, 33, 34] is a well benchmarked general purpose tool for calculations of particle transport and interactions with matter, covering an extended range of applications, such as accelerator shielding, target design, calorimetry, activation, dosimetry, cosmic ray studies, detector design, Accelerator Driven Systems, radiotherapy, neutrino physics etc. About sixty different particles can be transported by the code with high accuracy, including photons, electrons and muons from 1 keV to 1,000 TeV, hadrons of energies up to 20 TeV (up to 10 PeV by linking FLUKA with the DPMJET code), neutrinos, and all the corresponding antiparticles, neutrons down to thermal energies and heavy ions. The program can transport also optical photons and polarised photons (e.g. synchrotron radiation). Tracking and time evolution of emitted radiation from unstable residual nuclei can be performed online. FLUKA can handle very complex geometries, using an improved version of the Combinatorial Geometry package, which has been designed to track correctly also charged particles, even in the presence of magnetic or electric fields. Various debugging and visualisation tools are also available [33, 34].

The history of FLUKA (FLUctuating KAskades) goes back to 1962-1967, when Johannes Ranft wrote at CERN the first high-energy Monte Carlo transport codes for hadron cascades. Along the years it is possible to distinguish three different generations of FLUKA codes and the name has been preserved only as a reminder of its historical development. The present FLUKA, mostly an effort started in 1990 in order to get a suitable tool for the LHC era, is completely different from the versions which were released before 1990. The code is widely used at CERN and in other laboratories worldwide [33].

3.2.1 Electromagnetic and Muon Transport

FLUKA has been best known for its hadron event generators in the past, but since around 1990, it can handle electromagnetic (EM) effects with similar or better accuracy. The energy range covered by this sector is very wide. Photons, electrons and muons from 1 keV up to 1 PeV can be transported in the program. The electromagnetic part is fully coupled with

the hadron sector. The electromagnetic cascade simulation is very accurate, including a special treatment of the bremsstrahlung spectrum tip and the Landau-Pomeranchuk-Migdal effect [35]. As an improvement of the common practice of using average angles, electron pairs and bremsstrahlung are sampled from the proper double differential energy-angular distributions. The 3D shape of the EM cascades is reproduced in detail by a rigorous sampling of correlated energy and angles in decay, scattering, and multiple Coulomb scattering. In 2005, data from the EPDL97 [36] photon cross section library have become the source for pair production, photoelectric and total coherent cross-section tabulations, as well as for atomic form factor data. Bremsstrahlung and direct pair production by muons are modelled, as well as muon photonuclear interactions [32].

3.2.2 Charged Particle Transport

Charged particles are transported through an original Multiple Coulomb scattering algorithm, supplemented by an optional single scattering method. The ionization energy loss treatment is based on a statistical approach alternative to the standard Landau and Vavilov ones. Multiple scattering including nuclear form factors is applied also to heavy ion transport. Modern effective charge parameterizations are used. Straggling of ion energy loss is described in "normal" first Born approximation including charge exchange effects [32].

3.2.3 FLUKA Hadronic Models

For energies below a few GeV, hadron-nucleon interactions are treated by the isobar model, through resonance production and decay, taking into account elastic, charge and strangeness exchange. For higher energies, the Dual Parton Model coupled to a hadronization scheme was implemented for elementary hadron-hadron collisions. These collisions are the basis for hadron-nucleus collisions. The Glauber-Gribov calculus is involved in multiple collisions of hadrons with the nuclear constituents. The nuclear effects on hadron propagation are of particular importance and are treated by the FLUKA nuclear interaction model called PEANUT (Pre-Equilibrium Approach to Nuclear Thermalisation). A Generalized IntraNuclear Cascade (GINC) with smooth transition to a pre-equilibrium stage performed with standard assumptions on exciton number or excitation energy is included in this model. For the details about highly sophisticated GINC modeling in PEANUT see [32]. Other implemented models include evaporation, based on the Weisskopf-Ewing approach, in competition with fission and gamma deexcitation, a Fermi break-up model for light nuclei, improvement of residual nuclei production from heavy targets, etc [32].

3.2.4 Low Energy Neutrons

A multi-group algorithm is involved in transport of neutrons with energies lower than 20 MeV. In this technique, the energy range of interest is divided into a given number of intervals (energy groups). There are 260 energy groups in the FLUKA cross section library (tabularized in [33]). A discretisation of a P5 Legendre polynomial expansion is used to obtain the angular probabilities for inelastic scattering. For a few isotopes, neutron transport can be treated also through continuous (pointwise) cross-sections. Also gamma generation by low energy neutrons is treated in the frame of a multigroup scheme. The probability that a neutron in a given group will generate a photon in each of 42 gamma energy groups (covering 1 keV – 50 MeV) is provided by a downscattering matrix. Then the generated gammas are treated as all other photons [32, 33].

3.2 FLAIR

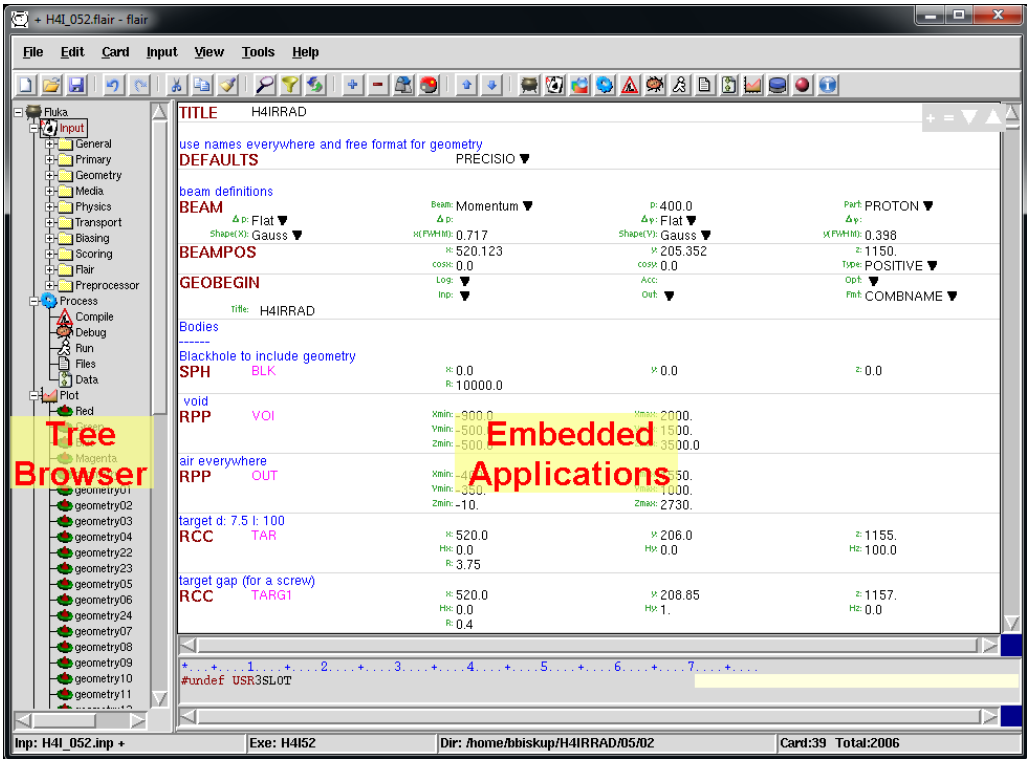

Figure 8: FLAIR main application window.

FLAIR (FLUKA Advanced Interface) [37] is an advanced user friendly graphical interface for FLUKA, to enable the user to control FLUKA jobs completely from a GUI environment. It is based entirely on python and Tkinter allowing easier portability across various operating systems. FLAIR is an integrated development environment, which provides means for the post processing of the output but also for creation and checking of error free

input files. It contains an editor (see Figure 8) for editing the input files in a human readable way with syntax highlighting and provides means for building the executable, debugging the geometry, running the code, monitoring the status of runs, inspection of the output files, post processing of the binary files and interface to plotting utilities like gnuplot and PovRay. FLAIR includes also a database of selected properties of all known nuclides as well as a database of approximately 300 predefined materials together with their Sterheimer parameters [38].

3.3 SimpleGeo

SimpleGeo [39] is an interactive 3D solid modeler which allows the user to interactively build geometries using a number of basic primitives that are connected by boolean operations. It also includes a debugging system, in order to validate the created geometry with immediate visual feedback of problematic regions. SimpleGeo currently allows for importing, viewing and editing of FLUKA, PHITS and MCNP(X) geometries, as well as creating new geometries from scratch and exporting to aforementioned Monte Carlo codes.

3.4 G4beamline

G4Beamline [40] is a particle tracking simulation tool based on the Geant4 toolkit, optimized to easily simulate beamlines and other systems using single-particle tracking. It is flexible enough to simulate complex beamlines, but because of its simple and straightforward method of specifying the system, it is also suitable for quickly answering questions about particle interactions and tracking. The notion “beamline” is more general, as a Cosmic Ray “muon beam” is included as well.

4. GIF++ Gamma Irradiation Facility

In section 2.1 there has been described the importance of the Gamma Irradiation Facility (GIF) in CERN West Area, which combined a high intensity gamma source with a particle beam. This facility has been operating since 1997 and is still fully booked for detector tests. However there has been a need for a stronger gamma source and after 2004, when the beamlines were dismantled from the West Area, also for regaining the possibility to carry out simultaneous detector performance tests with a high-energy particle beam. Given the obvious need for a new irradiation infrastructure, the Working Group on Future Irradiation Facilities at CERN [3], created in December 2007, has conducted a broad web-based enquiry on users needs for the new facility. As a results of the input from the users and the experience from the GIF, followed by design studies involving several CERN departments, implementation plans have been prepared for a future GIF upgrade, called GIF++ [4].

This chapter together with the following ones (chapters 4, 5 and 6) represent the core of the thesis, presenting the original work of the author. All the simulation studies have been performed by the author if not explicitly stated otherwise.

4.1 GIF++ Design

The GIF++ area has been planned to operate at the SPS H4 beam line in the North Experimental Area of CERN. For the implementation to the North Area see Figure 9.

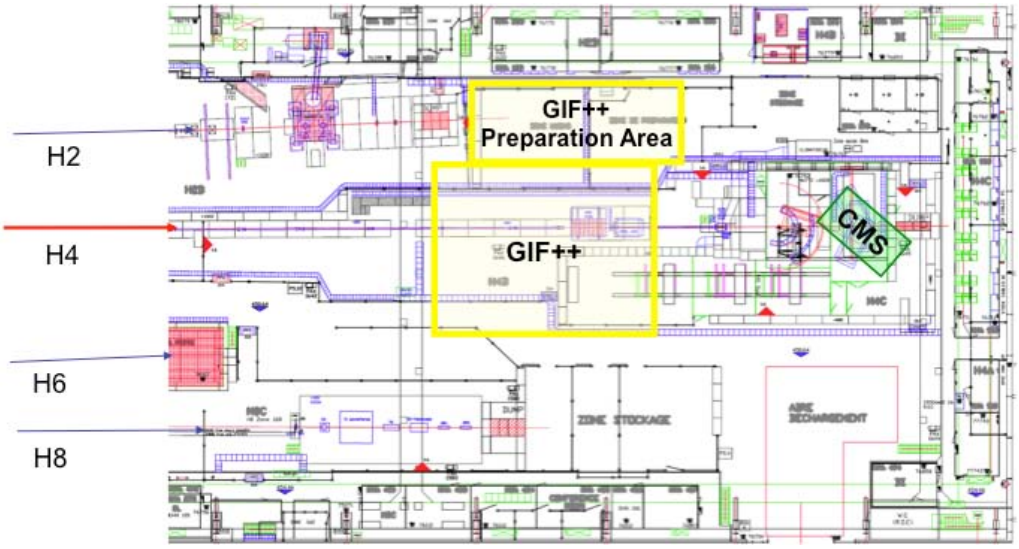

Figure 9: Floor plan of part of the H4 beam line in the EHN1 (CERN Building 887). GIF++ is located at the end of the beam line, downstream is the CMS ECAL beam test area [5].

Figure 10 shows the proposed layout of the GIF++ bunker. The floor area is approximately 170 m^2 and a total height is about 4.8 m. It is wide enough to host simultaneously very large objects with a possibility of positioning to various distances from the gamma source in order to simulate the desired background rate.

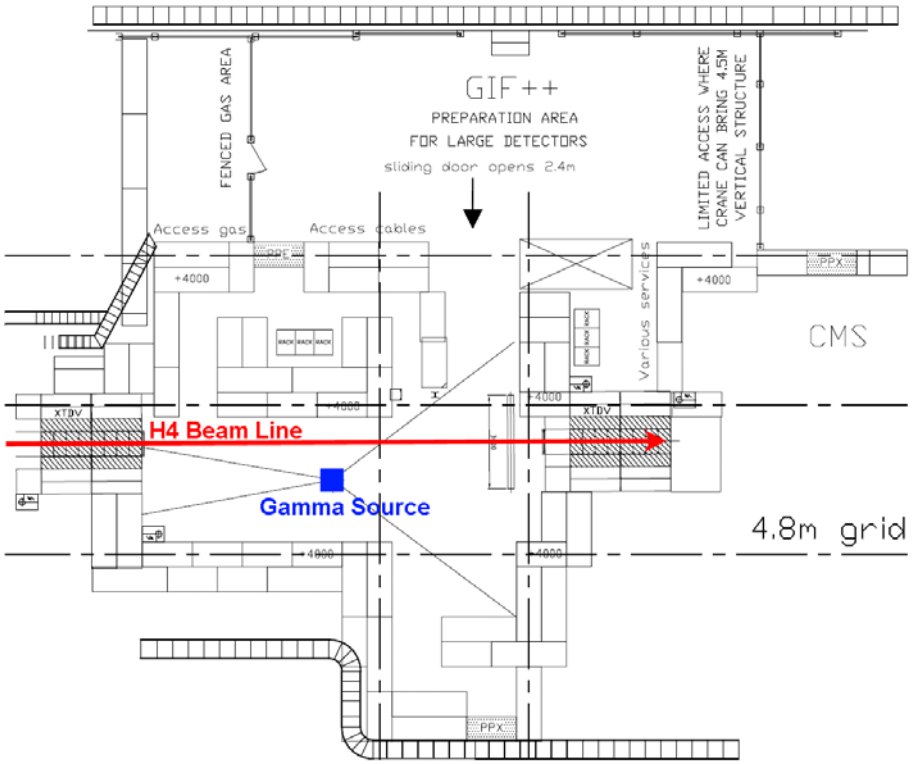

Figure 10: Layout of the GIF++ bunker and its preparation area [5].

The geometry consists of an irradiator and a concrete shielding, replaced by iron blocks around the beam-pipe. The concrete shielding is 160 cm thick in most places and the roof has a thickness of 80 cm.

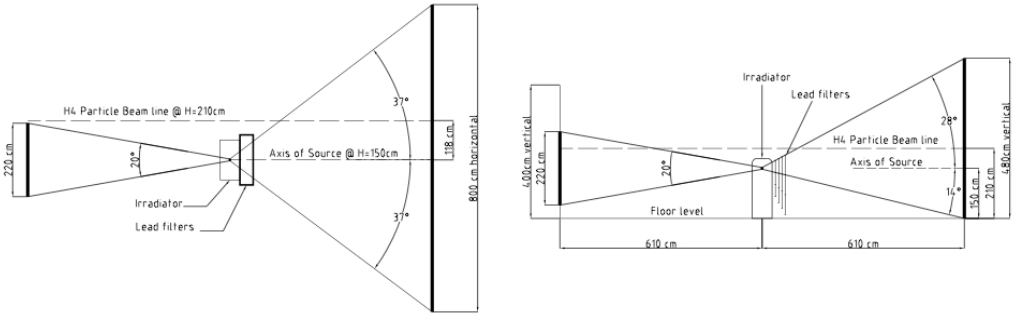

Figure 11: Top (left) and lateral (right) view of the gamma irradiator and H4 beam line [5].

The gamma source is placed 1.5 m above the floor level and the particle beam line is at the hight of 2.1 m and 1 m aside of the gamma source. The irradiator is a lead box with two irradiating windows. The bigger one towards downstream has a rectangular shape and

determines the irradiation angle of 74° on a horizontal plane and 42° on a vertical plane (28° upward + 14° downward). The smaller one provides a pyramidal aperture of 20° × 20° towards upstream (see Figure 11).

As a gamma source, ^{60}Co was preferred by some users due to its high energies of 1.17 MeV and 1.33 MeV. But since the 30 years half-life of the ^{137}Cs makes this isotope relatively stable in comparison with ^{60}Co (only 5.27 years), caesium was finally selected. With its spectrum of primary (662 keV) and scattered photons, ^{137}Cs matches reasonably well the energy spectrum of around 1 MeV expected for background in LHC muon detectors. The selected activity of 10 TBq (~13.5 × higher than in the previous GIF) should provide up to 3.68 Sv/h at a distance of 50 cm from the source.

4.2 GIF++ Optimization Studies

4.2.1 GIF++ Shielding Optimization

In order to establish the radiation field inside and outside the area, a complete geometry from the implementation proposal [5] was used. In Figure 12 is a top view of the GIF++ geometry, as used in the FLUKA [32, 33] simulations (both the irradiator and the beam-pipe are displayed, although not located at the same height).

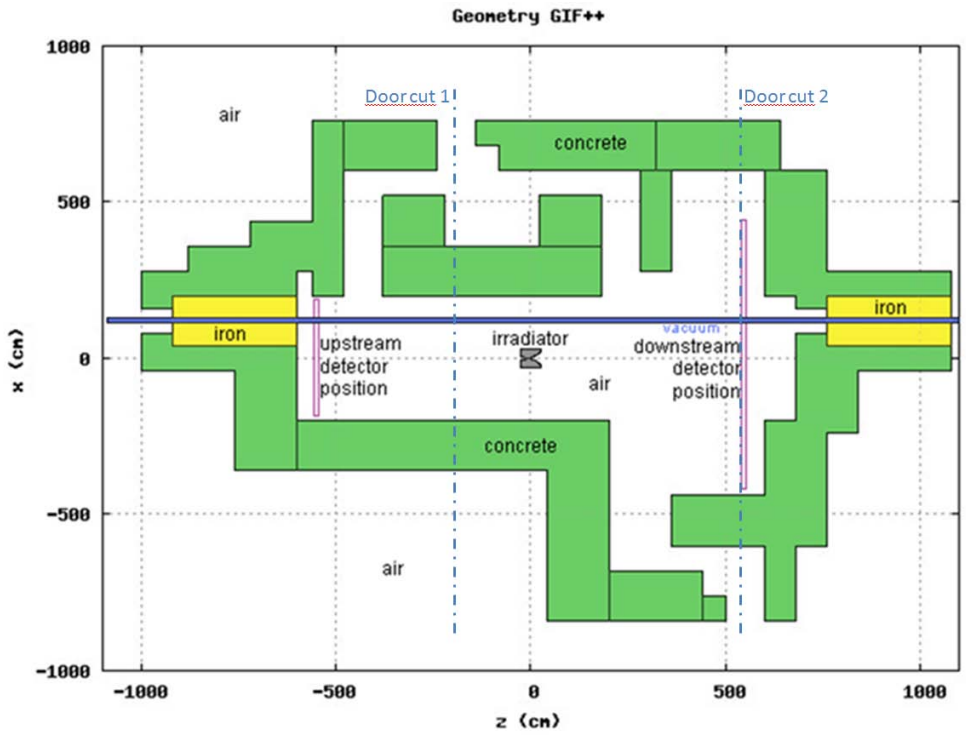

Figure 12: GIF++ geometry as used in the FLUKA simulations (gamma source plane together with the beam-plane).

The most important task of these studies was to verify if the proposed shielding is sufficient in terms of radiation protection. The North Experimental Hall is classified as a 'low-occupancy supervised radiation area' with a maximal allowed limit of 15 µSv/h [41]. The complete geometry (Figure 12) was used to obtain prompt dose equivalent. The horizontal projections of the FLUKA simulation results at the source and the beam-line height are shown in Figure 13 (top and bottom, respectively).

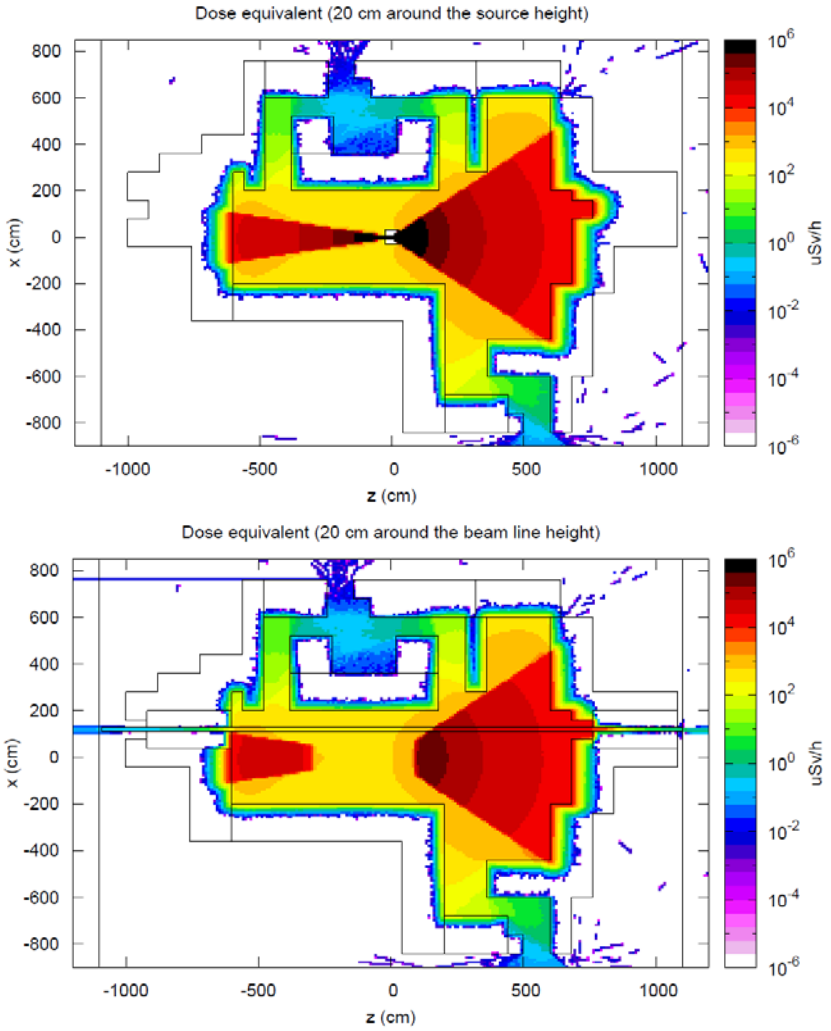

Figure 13: Horizontal cut of simulated ambient dose equivalent rate in µSv/h averaged over ±10 cm vertically around a gamma source height (top) and beam line height (bottom) for the GIF++ layout.

The most critical points proved to be the access doors. From Figure 14, which displays projections over the upstream and downstream doors, it can be noted that the dose equivalent does not exceed 1 µSv/h and thus is well below the allowed limit directly behind the doors. Streaming through the beam pipe causes the dose equivalent around 3 µSv/h behind the downstream shielding opening, but this location is inside the beam line area, thus can be interlocked and not accessible during operation.

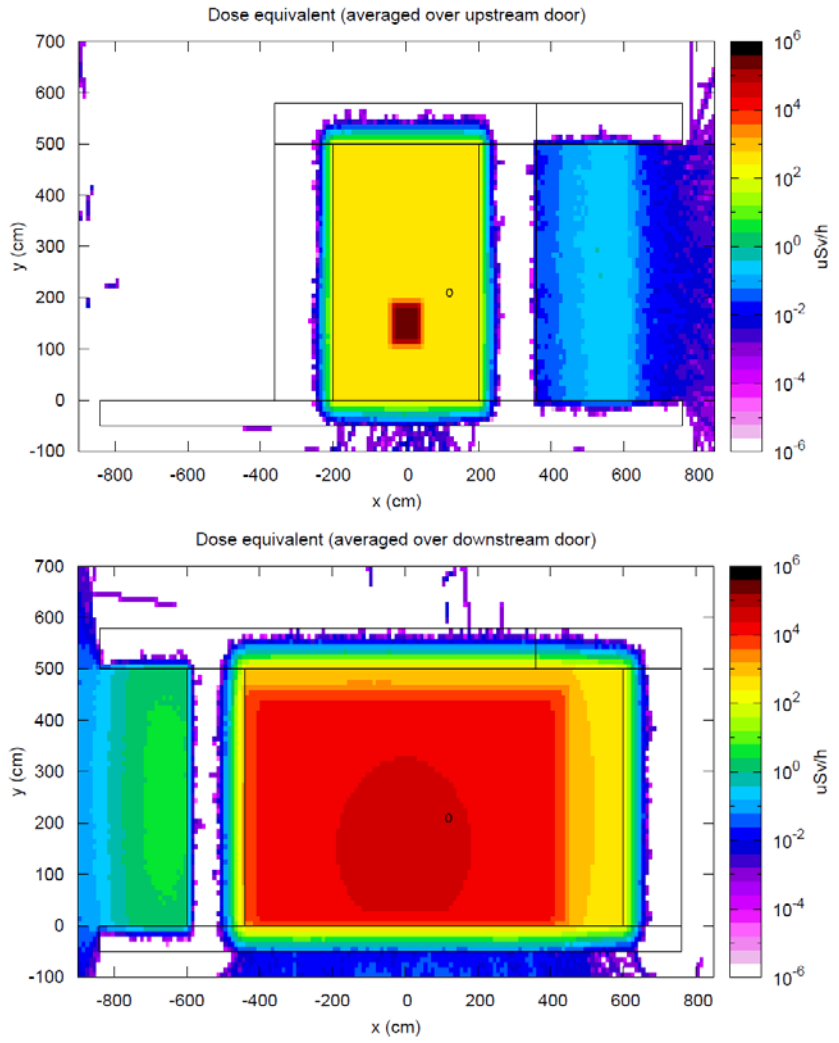

Figure 14: Vertical cut of simulated ambient dose equivalent rate in µSv/h averaged horizontally over upstream (top) and downstream (bottom) door for the GIF++ layout. For the position of these cuts see Figure 12 ("Door cut 1&2").

In the previous simulations an ideal geometry without any gaps between shielding blocks was taken into account. However, this is technically too difficult to construct. Therefore simulations to study the influence of shielding gaps to the radiation field outside the bunker have been carried out. A simplified geometry with a rectangular basis and only 80 cm thick concrete shielding was used. 3 cm thick T-shaped gaps were implemented to the roof. Circular holes with a diameter of 2 cm and 3 mm thick vertical gaps were added to the side shielding walls. As visible in Figure 15, the gaps in the shielding and in the roof have no serious influence on the radiation field outside the shielding – the dose equivalent is still below 1 µSv/h. The other outcome from this simulation is that in general the 80 cm thick shielding should be sufficient. Nevertheless the originally proposed shielding with 160 cm thick walls was maintained for static reasons. It also gives a possibility to increase the source intensity in the future.

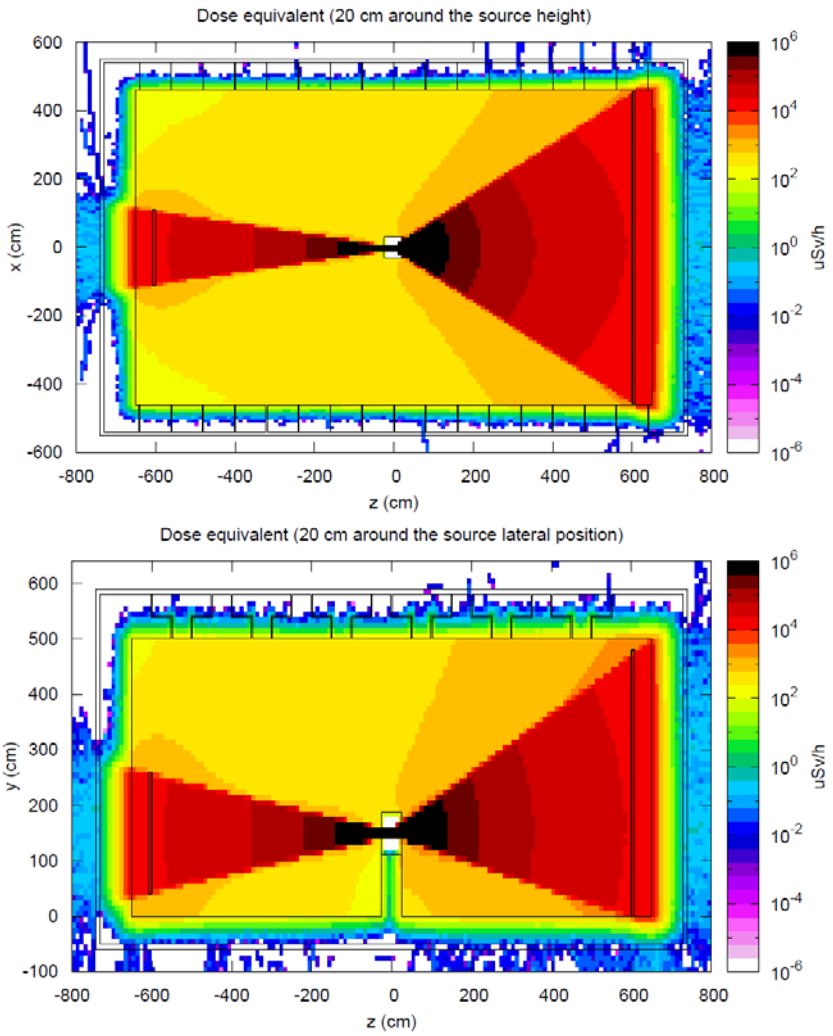

Figure 15: Horizontal (top) and vertical (bottom) cut of simulated ambient dose equivalent rate in µSv/h averaged over ±10 cm around the gamma source position for a simplified geometry with air gaps.

4.2.2 GIF++ Radiation Field

The complete GIF++ geometry model was used to determine the radiation field inside the area. It is important to know how the spectrum from the gamma source is altered by the scattering and which spectrum really reaches the tested detectors. Figure 16 shows the photon spectra at the downstream test position (marked in Figure 12) as an energy distribution of a photon current streaming from the source direction and of a photon current "backscattered" from the downstream shielding. The spectrum of photons from the source is clearly dominated by the original source energy, i.e. 662 keV, but due to the scattering from the surrounding material, mainly the irradiator box, also lower energies are represented. The spectrum of photons reaching the detector position from the downstream direction is dominated by lower energies. After a consideration and discussion with the user community whether to maintain photon fluence as high as possible or to use photons as monoenergetic as

possible by minimizing the scattered radiation, there has been decided not to block the scattered radiation by any shielding surface modifications.

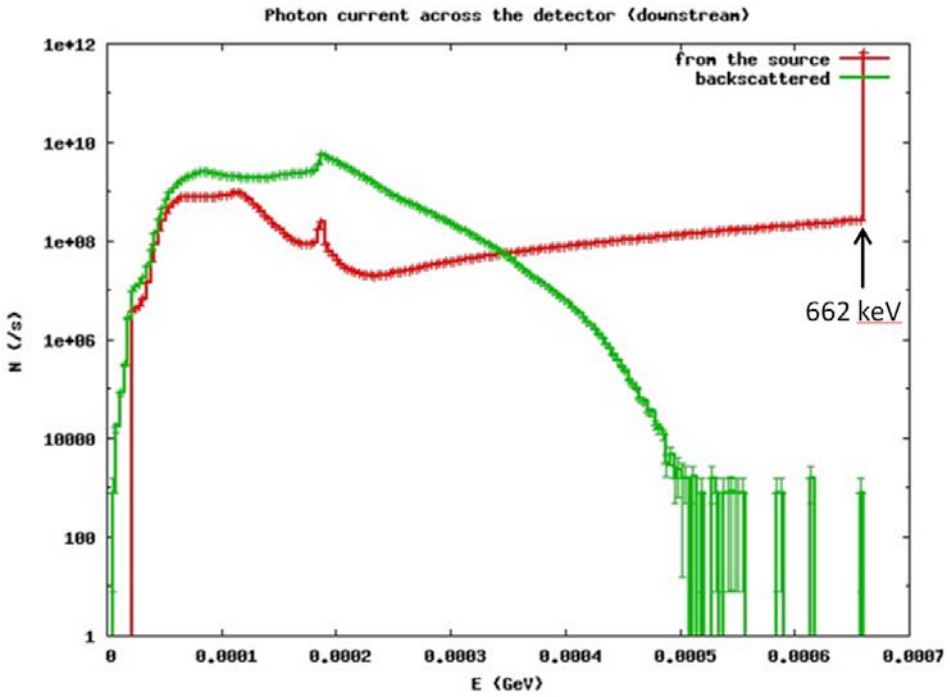

Figure 16: Photon spectra at the downstream test position (as marked in Figure 12) – current from the source direction and from the downstream shielding direction.

In Section 4.2.1 the dose equivalent downstream the GIF++ shielding caused by photon streaming through the beam pipe was mentioned. Nevertheless, for the experiments operating downstream the GIF++, it is more important to predict a fluence of escaping photons and their energy distribution. As the beam pipe diameter is relatively small (15.9 cm) compared to the irradiation solid angle, a simplified geometry was used for the technical reasons. This simplification led to slight changes in the scattered photon spectra. But since the impact of lower energy photons is not crucial for this study, this approximation gives a reasonable result. The photon current through the beam pipe is displayed in Figure 17 as a dependence on a distance from the downstream iron shielding beginning (it corresponds to z = 0 m). The last point in the chart shows the photon current 10 m behind the iron shielding termination (i.e. z = 13.2 m). The energy spectra corresponding to the beginning of the iron shielding, its middle and termination as well as 2 m, 5 m and 10 m behind the shielding end point are shown in Figure 18. The estimated rate of 1 kHz of photons at 10 m downstream GIF++ (as visible from Figure 17), should pose no problems to the operation of the downstream experiments.

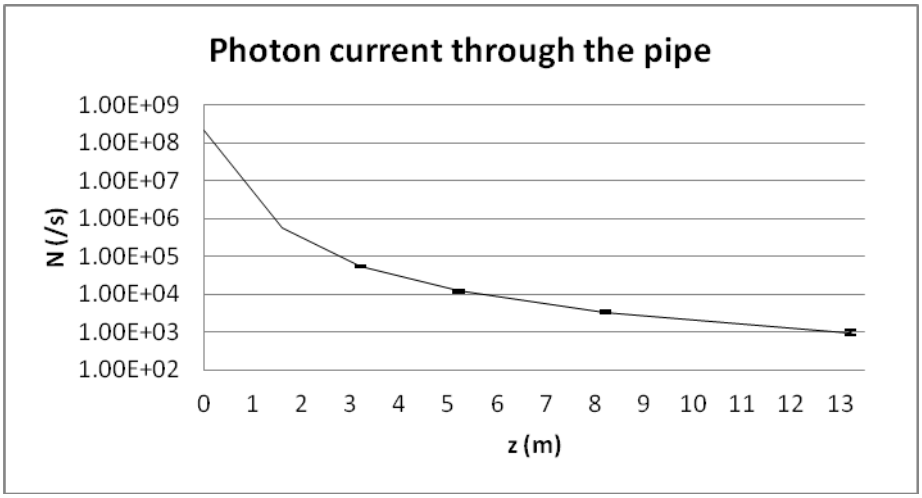

Figure 17: Photon current through the beam pipe from the beginning of the downstream iron shielding until 10 m behind the shielding termination.

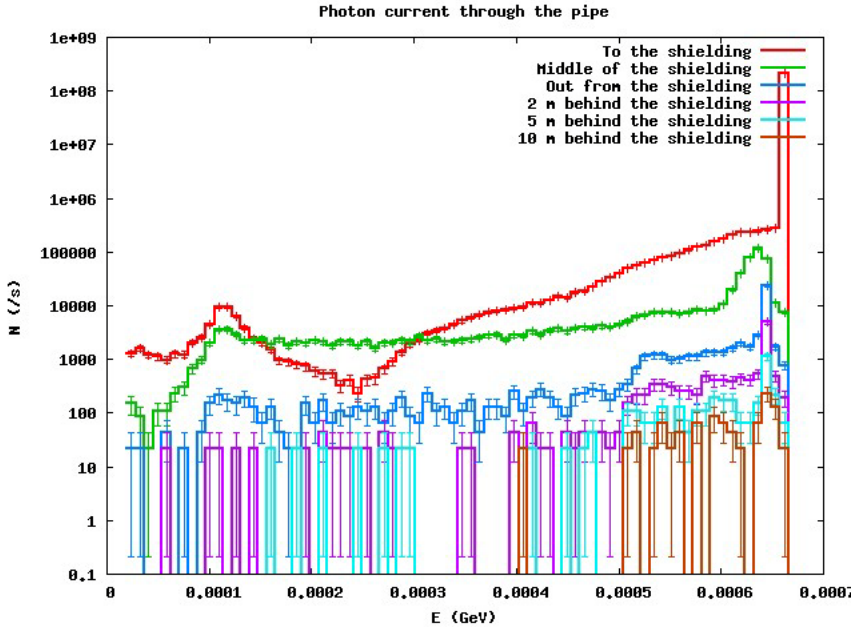

Figure 18: Energy spectra of photons streaming through the beam pipe at the beginning, in the middle and at the end of the downstream iron shielding and 2 m, 5 m and 10 m behind the shielding termination.

4.2.3 Radiation Field Gradient Optimization

Some of the test detectors have a surface of several square meters and it is highly desirable to irradiate the whole detector under the same conditions. Therefore the radiation field gradient should be as low as possible over the whole test area. The gradient was studied in upstream and downstream test locations (for the test positions see Figure 12) as photon fluence over 5 cm thick vertical cuts. It is well visible from fluence 2D projections in Figure 19 that while the delimitation of the irradiation areas (square or rectangle) is quite sharp, the radiation field over the test areas is deformed due to different path lengths from the gamma source to the different detector points.

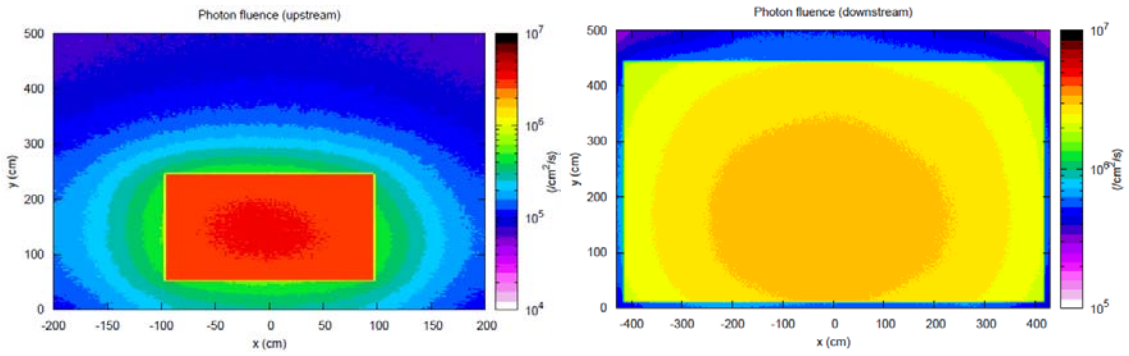

Figure 19: Photon fluence vertical cut averaged over the upstream (left) and downstream (right) test positions (for these "detector positions" see Figure 12).

For a better quantitative visualisation 1D plots are presented for horizontal and vertical axes for both test positions in Figure 20. The high gradient is much more significant for the downstream detector due to much wider irradiation angle. From the lower left chart in Figure 20 we can note the difference around 30 % between the centre and the detector side, but this difference is even higher between the detector centre and its (especially upper) corners.

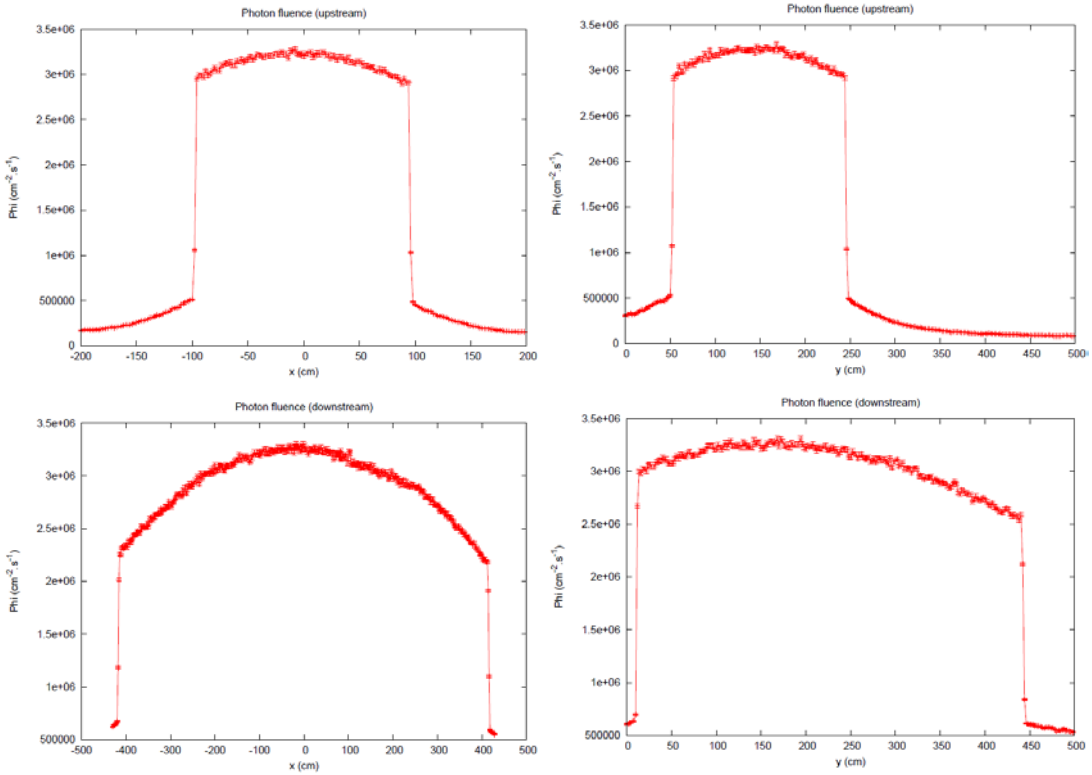

Figure 20: 1D photon fluence projections over the upstream (upper) and downstream (lower) test positions averaged over ±1 cm around horizontal (left) and vertical (right) axes.

To unify the deformed radiation field, special filters were designed using only simple shapes allowing easy manufacturing. As a simplest option, there have been studied lead filters with a flat inner part (facing the irradiator) and a spherical profile on the outer side and with squared or rectangular sharp edges to determine the irradiation shape. The filter radius was

optimized in dependence on the field gradient over the test locations. For the upstream positions, the best uniformity was reached for a sphere radius of 100 cm. The results are presented in Figure 21 as 1D projections along horizontal and vertical axes. In comparison with the setup without the lead filters (Figure 20, upper) we can note a good improvement in light of field gradient, but the maximum of fluence decreased by ~20 %.

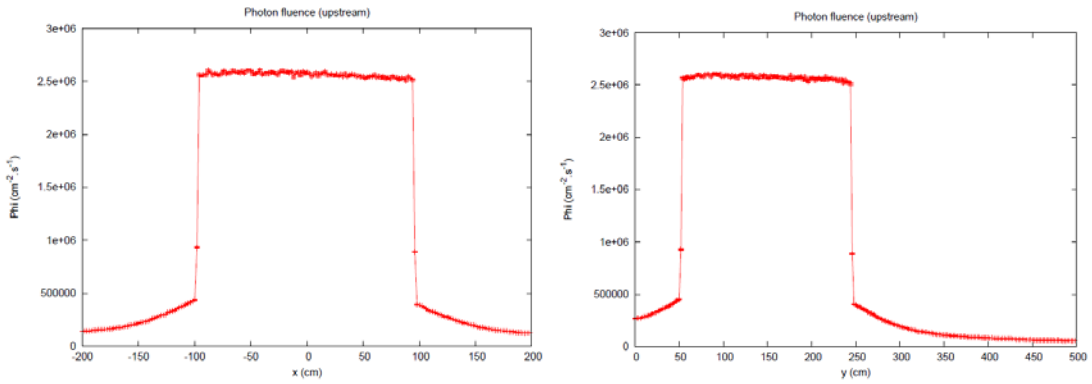

Figure 21: 1D photon fluence projections over the upstream test position averaged over 2 cm around horizontal (left) and vertical (right) axes. A lead spherical filter with a radius of 100 cm was applied.

While for the smaller upstream irradiation window, the approach with the simple spherical profile filter is fully sufficient, for the big rectangular window, the situation is more complicated. For the best compromise using a spherical profile filter, the horizontal fluence projection reaches convex profile, while the vertical one has still concave characteristic. As a more complex approach a combination of two filters with a cylindrical profile was studied. The best result was reached for the inner cylindrical filter for horizontal correction with a radius of 320 cm and the outer filter for vertical correction with a radius of 260 cm for its upper part (from the source axis upwards) and 150 cm for its lower part (see Figure 22). The 1D fluence projections after correction are presented in Figure 23. For the downstream test position the fluence maximum would drop by ~ 60 % in comparison with the setup without the lead filters (Figure 20, lower). The fluence profile is still not completely flat, but the differences are only in order of few percents, so this correction is fully sufficient for the scope of detector testing.

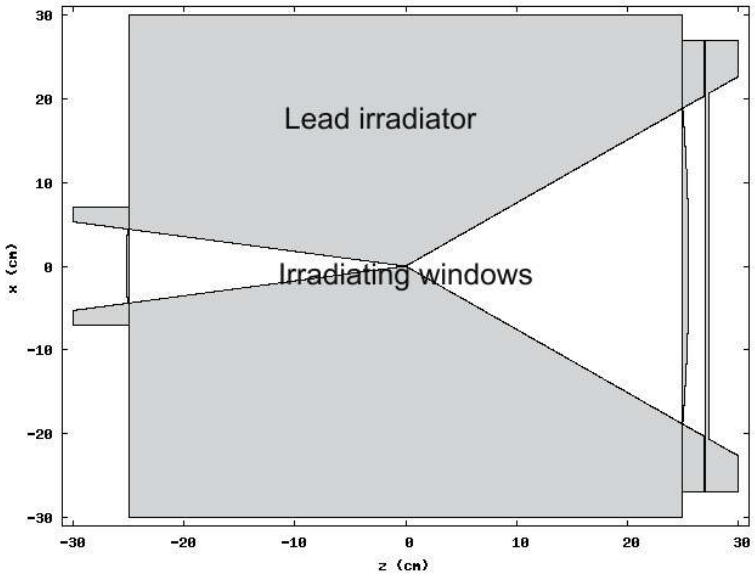

Figure 22: Gamma irradiator with the lead filters for a field gradient correction – central cut, side view.

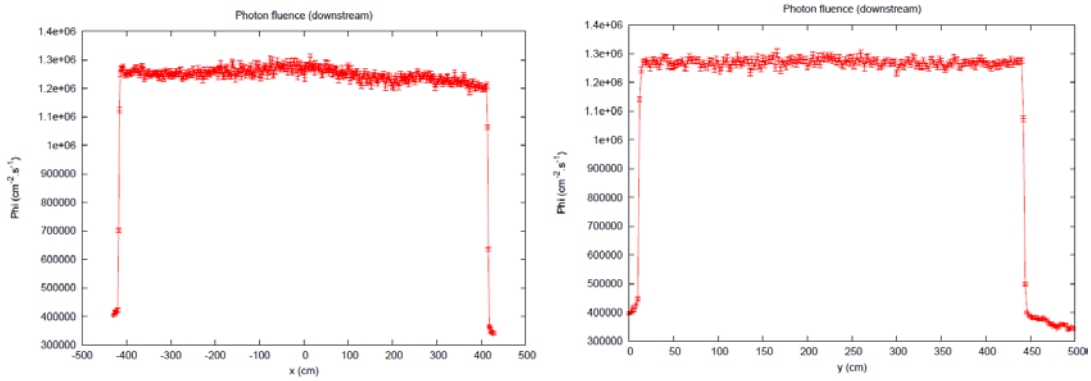

Figure 23: 1D photon fluence projections over the downstream test position averaged over 2 cm around horizontal (left) and vertical (right) axes. Lead cylindrical filters presented in previous Figure 22 were employed.

4.3 GIF++ 2013 Upgrade Optimization Studies

The studies presented in the previous sections have been completed in 2010 showing that operation of the GIF++ facility with the presented parameters is compliant with the safety limits which are applicable in a supervised radiation area. In 2012 the construction of the facility was approved and since then the layout underwent several design upgrades. As one of the last steps before initiating the construction phase, the current layout proposal has been studied again using FLUKA Monte Carlo code in order to verify radiation safety and improve potentially weak points.

4.3.1 Simulation Input and Boundaries

The simplified GIF++ footprint is displayed in Figure 24 (for details see Ref. [42]). The ^{137}Cs gamma source (marked by a red S) is placed inside a lead irradiator box with two

collimators providing a conical aperture of horizontal ±37° × vertical ±37° towards both the upstream (left) and downstream (right) direction. The nominal activity of the source is 16.65 TBq (~1.5 Sv/h in 1 m distance) with 85% gamma (at 662 keV) emission probability. The irradiation area is surrounded by 160 cm thick concrete shielding, only around the upstream and downstream beam line openings, iron shielding blocks are used.

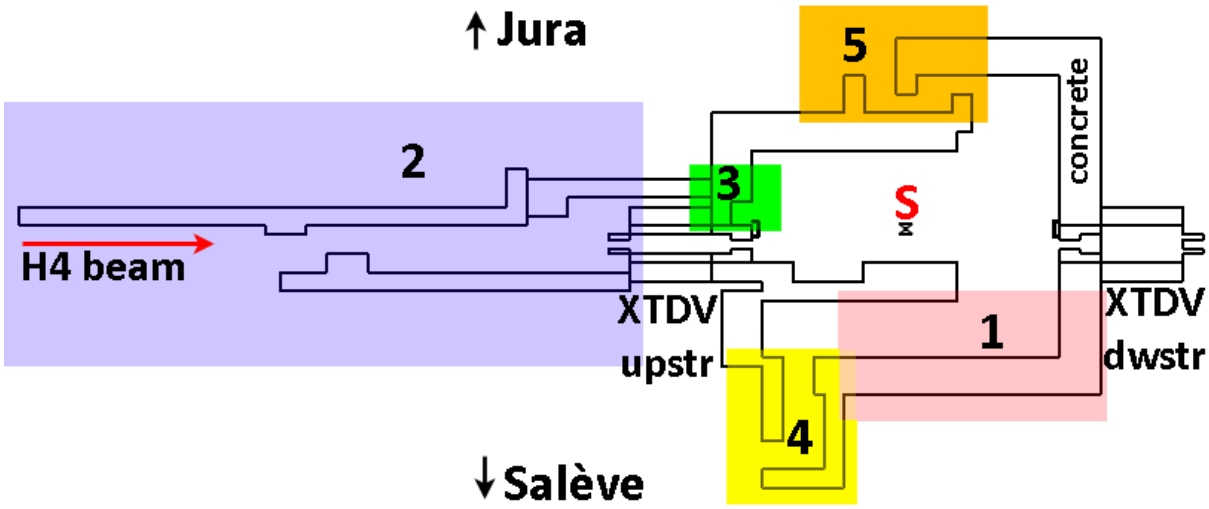

Figure 24: GIF++ footprint: top view at the source height. The coloured areas indicate the sections with detailed dose rate studies presented in the following sections. S stands for the source, XTDV is a vertically movable dump and upstr/dwstr is an abbreviation for upstream/downstream [43].

For the calculations a conservative scenario has been assumed implying several simplifications: 1) the stainless steel container (sealing) which covers the real source is not implemented. A point source in the centre of the nominal source position is used. 2) The angular correction filters, attached directly to the irradiator, are omitted (their implementation will suppress radiation intensity by about a factor of two). 3) Lead attenuation filters (with optional attenuation factors up to 510^{4}) are not taken into account. A safety margin resulting from these simplifications depends on a potential use of the attenuation filters, but is always higher than a factor of two (up to several orders of magnitude).

For the studies here the upstream vertically movable dump (XTDV) is open and the downstream one is closed. They are placed symmetrically with respect to the photon fields.

The simulation deals only with radiation caused by the gamma source. The muon beam used by GIF++ will result in an additional dose rate of approximately 1 µSv/h in forward direction. During operation of experiments located downstream of the GIF++ zone, the H4 beam line provides typically electrons for which it is designed and the contribution to the dose rate is negligible.

4.3.2 Simulation Results

The purpose of these studies is the optimization of the updated facility setup in terms of radiation safety. Following a few modifications as described here the final facility layout is fully compliant at the outside shielding boundaries in view of the acceptable radiation levels of a supervised radiation area [41] which are 3 µSv/h in permanent workplaces and 15 µSv/h in low-occupancy areas.

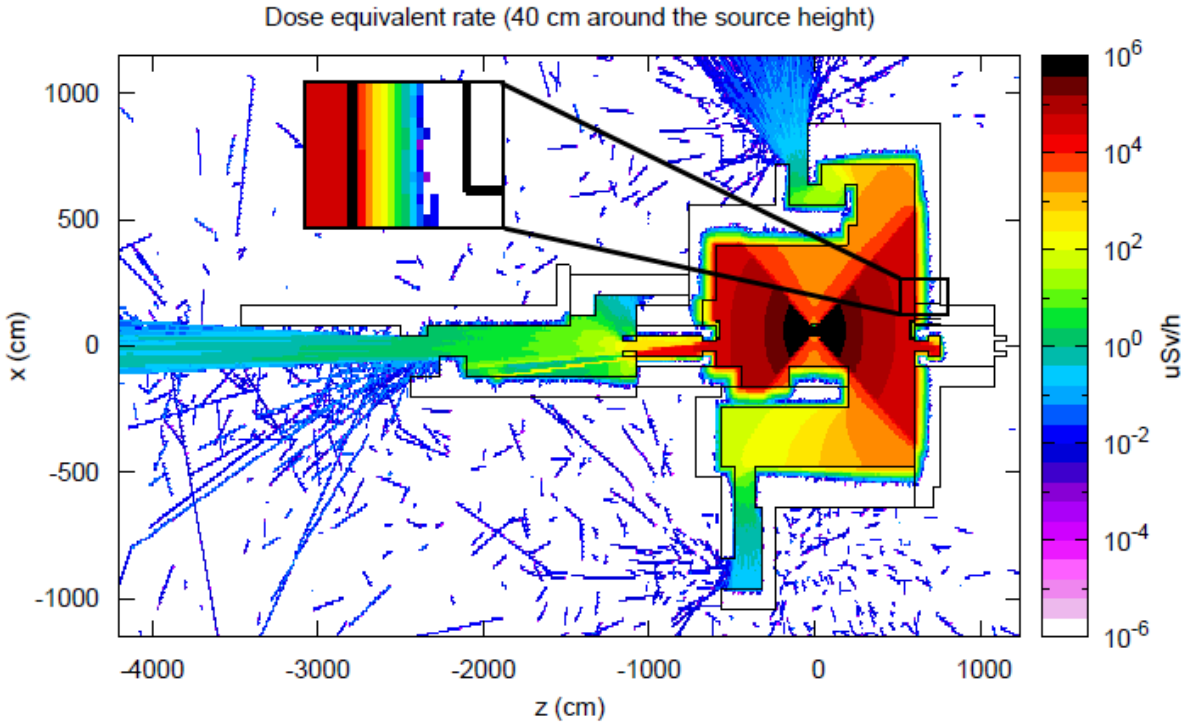

Figure 25: Ambient dose equivalent rate – horizontal cut at the source height averaged over ±20 cm vertically [43].

Figure 25 shows the ambient dose equivalent at a horizontal cut of the whole GIF++ geometry. 80 cm of concrete shielding suppresses the radiation sufficiently (see the detail in Figure 25). However, the second shielding layer is employed to shield the joints between the concrete blocks (more details in the section 4.3.5), but is also required for stability in the case of earthquakes. For the most critical areas (marked #1 – #5 in Figure 24), the detailed studies are described in the following sections.

4.3.3 Radiation Behind the Cable Passage

Cable passages from the bunker to the outside are provided by introducing 10 cm high feed-throughs just above the concrete floor without shielding (typically 1 m width). The most critical ones are located in the area #1 (see Figure 24, not visible in this geometry cut as they are located 2 m below the source). The study shows that the dose equivalent could reach

values up to around 10 µSv/h through the originally proposed passages (see Figure 26, left). Relocation of the passages decreased the value by few µSv/h. The final measure preventing excessive streaming outside the area was to add 5 cm thick and 15 cm high iron blocks around the cable maze entrance as indicated in the right plot of Figure 26. The resulting dose equivalent rate projection at the boundaries of area #1 (averaged over the cable passage height) is well below 1 µSv/h.

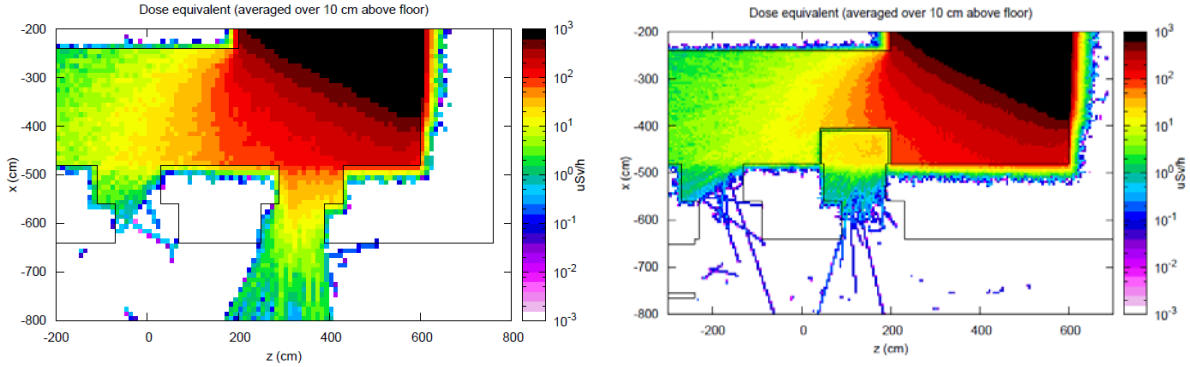

Figure 26: Ambient dose equivalent rate – horizontal cut averaged over 10 cm vertically above the concrete floor (area #1 in Figure 24) for the non-optimized layout (left) and the improved layout (right).

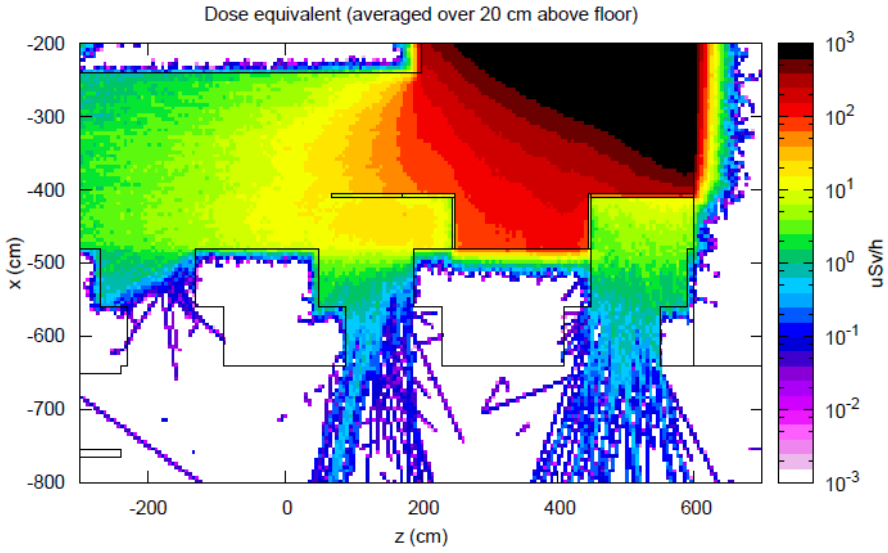

Figure 27: Ambient dose equivalent rate – horizontal cut averaged over 20 cm vertically above the concrete floor for the final improved layout (area #1 in Figure 24).

Following requests from the users, the height of the feed-throughs from the service zone to the bunker was increased to 20 cm (from previously 10 cm). The iron blocks have been rearranged such that at the most exposed region their shielding height is 30 cm, the part below the cable tray (around the middle of the passage) remains 15 cm high and the rest of this iron shielding (the least exposed area) is removed. An additional cable passage was added close to the downstream wall. Introducing the maze structure as well, it is shielded by 5 cm

thick and 30 cm high iron blocks and by a 5 cm thick iron plate from the top at a height of 30 cm. This setup preserves the radiation safety as can be seen in Figure 27.

4.3.4 Radiation Through the Movable Dump

Studying another operation scenario, the upstream dump has been assumed to be open and consequently photons can be streaming out (see Figure 28). This upstream area of the beam-line (zone PPE144) is still shielded at least along 15 m. Outside this shielding and at the boundary of the fenced area the dose rates are compliant with the limits for a supervised radiation area. Thirty meters further upstream a fence is sufficient to comply with the applicable limits, as along the beam-line axis the dose rate is well below 1 µSv/h.

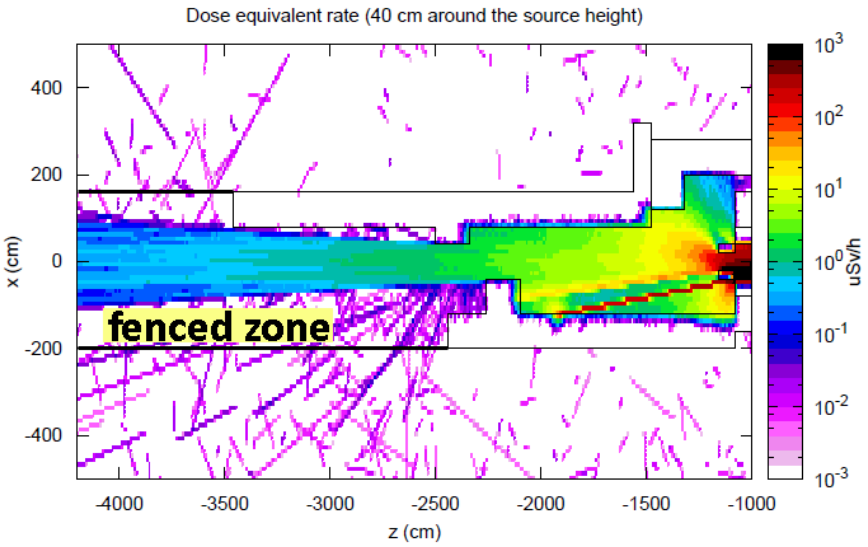

Figure 28: Ambient dose equivalent rate – horizontal cut at the source height averaged over ±20 cm vertically for the upstream zone (area #2 in Figure 24).

4.3.5 Radiation Through the Shielding Block Joints

To study the impact of the joints between blocks a representative situation was simulated. In the central forward direction of the photon source, a slit in the inner shielding layer is introduced (2 mm high, 100 cm laterally, 80 cm deep = 1 concrete layer). Figure 29 (top – dose equivalent rate in the area #3) shows that a single shielding layer is sufficient. The second concrete layer is shifted such that joints are not located at the same positions, i.e. not super-positioned.

Only at the positions where the first shielding layer has a vertical joint and the second layer has a horizontal joint (or vice versa), we can encounter a small opening through the whole shielding. To study this case a 2 mm × 2 mm gap through both layers of the

downstream shielding was implemented 40 cm aside of the source axis. Figure 29 (bottom) shows that the radiation is within acceptable limits already a few centimetres behind the first shielding layer. Taking into account these results, all potential gaps larger than 2 mm × 2 mm and penetrating the full shielding will be additionally shielded (metal sheets and/or fillings).

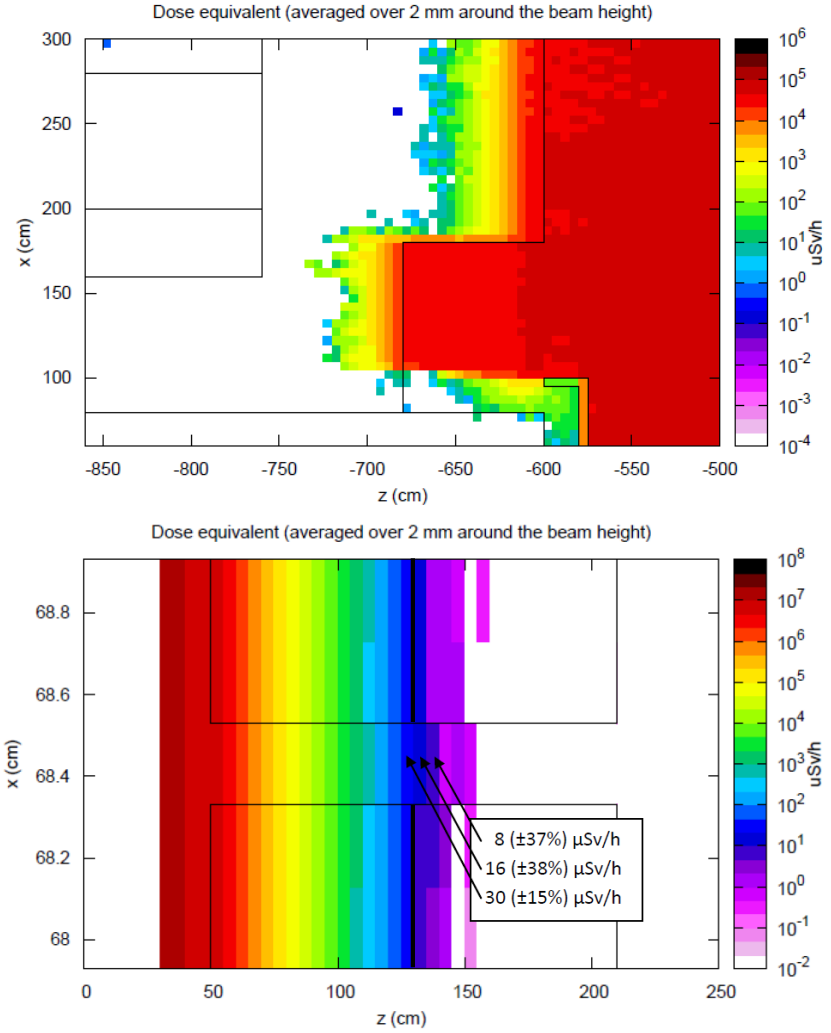

Figure 29: Ambient dose equivalent rate – horizontal cut at the source height averaged over ±1 mm vertically for the shielding block joint (top; area #3 in Figure 24) and for the 2 mm × 2 mm shielding block joint in the downstream shielding (bottom).

4.3.6 Radiation Through the Doors

For the doors, the optimization is based on the principles of distance and chicanes. To distinguish between directions in the North Hall, it is common practice to denote Salève or Jura side. The dose equivalent rate projection around the Salève door (region #4) in Figure 30 (top) confirms that the radiation is well below the limits, outside the door below 0.1 µSv/h.

Outside the Jura door (area #5) the dose rate is slightly higher than behind the Salève one, but still within the applicable limits. The ambient dose equivalent rate reaches up to 1 µSv/h at the entrance (see Figure 30, bottom).

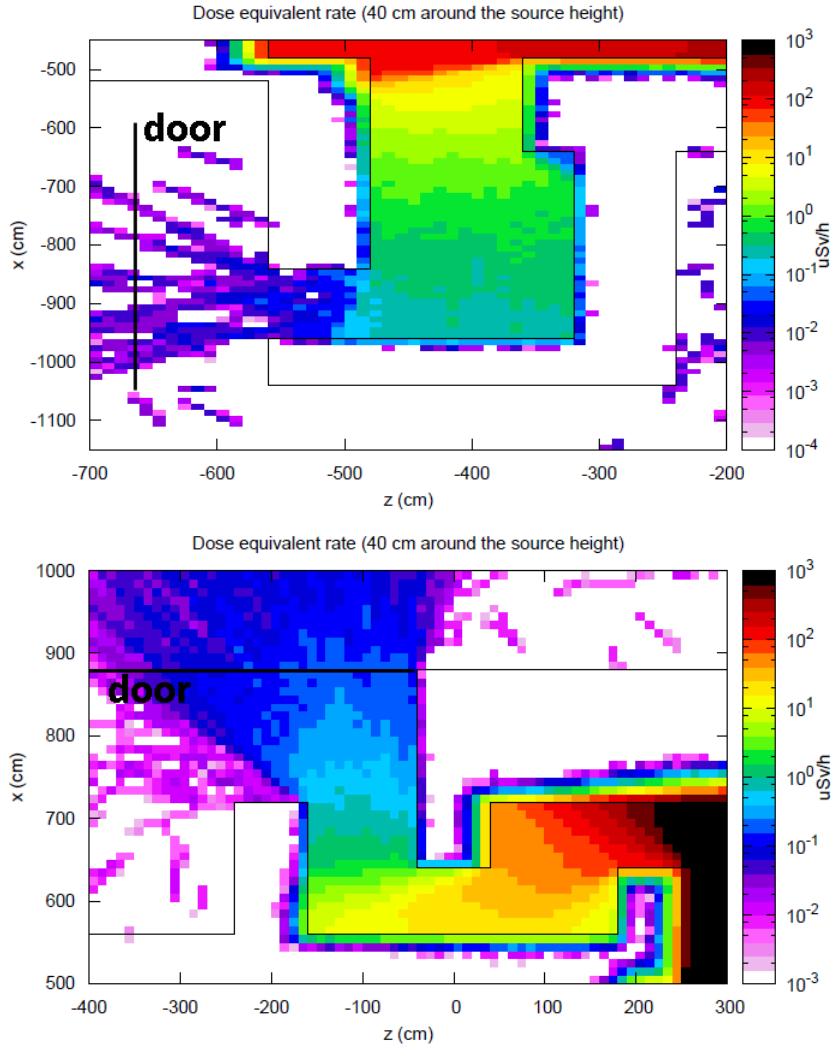

Figure 30: Ambient dose equivalent rate – horizontal cut at the source height averaged over ±20 cm vertically for the Salève door (top; area #4 in Figure 24) and for the Jura door (bottom; area #5).

4.3.7 Radiation Through the Roof

An initial choice of 40 cm roof thickness resulted in an acceptable dose at the boundaries, but a dose rate above 20 µSv/h over a very small area in the centre of the roof. With a minor additional effort, increasing the thickness to 60 cm concrete, the whole area of the roof, being a low-occupancy area, radiates with less than 1 µSv/h (see Figure 31), well within the limit of 15 µSv/h. Based on the obtained results the access to the roof will be blocked during the source operation. At an additional height of about 2 m above the roof the cabin of the overhead crane can pass and therefore the joints of the single layer concrete roof are covered with iron beams (20 cm × 20 cm).

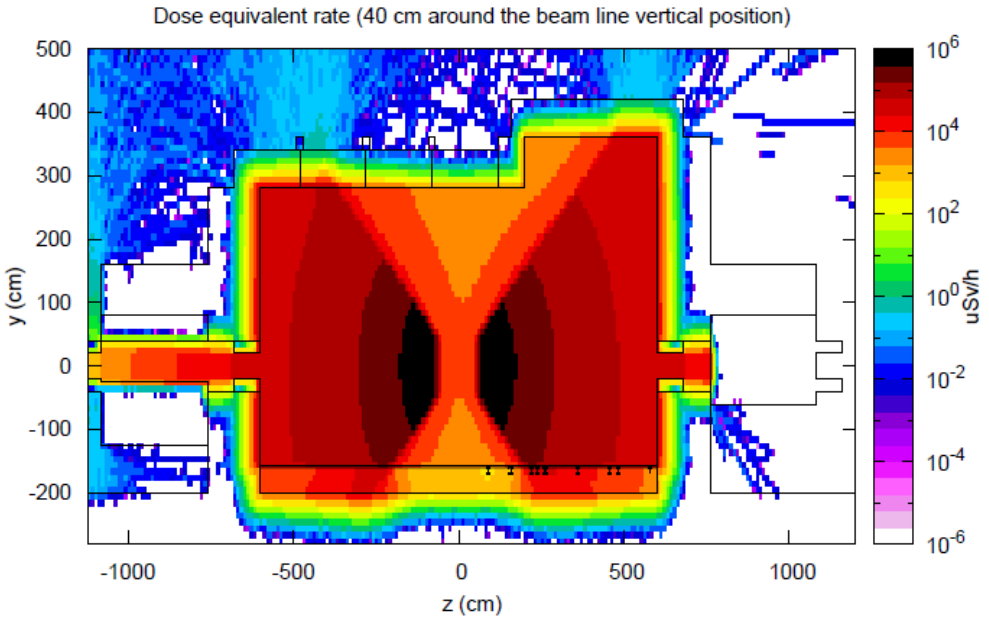

Figure 31: Ambient dose equivalent rate – vertical cut at the beam line position averaged over ±20 cm horizontally [43].

4.4 GIF++ Status and Schedule

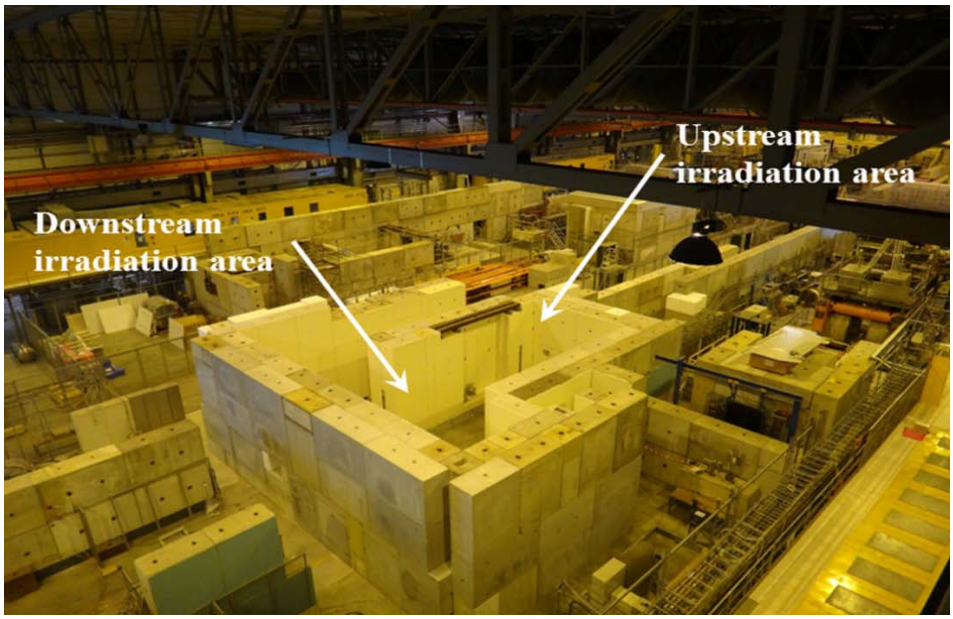

Figure 32: GIF++ concrete bunker without the roof during construction phase in April 2014.

The cleaning and old structures removal at the area allocated to the GIF++ began towards the end of 2013. The concrete bunker (see photo in Figure 32) was completed in April 2014, ready for the infrastructure (gas piping, cable trays, etc.) installation, which was finished in August. After the delivery of the irradiator in November 2014 the facility was commissioned in February 2015. The operation of GIF++ begun in March 2015 and is envisaged for several decades covering needs of diverse detector communities.

4.5 Summary

The GIF++, an upgrade of the Gamma Irradiation Facility, for testing big LHC detectors was introduced in this chapter. The motivation for building the facility and a design proposal was given. In the framework of the doctoral thesis the author modelled a full proposed GIF++ geometry, studied the radiation field inside and outside the bunker and optimized the facility shielding using the FLUKA Monte Carlo code. The main purpose of these optimization studies was to assure the radiation safety outside the shielding and the access doors. While the simulations confirmed the concrete wall thickness as sufficient even if assuming potential gaps between shielding blocks, the radiation above the proposed roof structure was found to be above the allowed limits. Therefore a roof thickness had to be increased. The principle of distance and chicanes used for doors fulfilled its purpose and the radiation at the door level is well below the safety limits. Radiation field at the test positions inside the facility was identified as well and a set of lead filters compensating the field intensity non-uniformity was optimised. Based on these studies the facility was approved, built and is operating since March 2015 with fully booked schedule.

5. H4IRRAD Mixed-Field Test Area

In the introduction, there was explained the need for a new irradiation test area for equipment for LHC, especially with its increasing intensity and luminosity. As was mentioned in the chapter 2, some tests can be carried out in external facilities (PSI, CEA and others), but these tests are usually limited by several constraints, especially by the size of the tested equipment and a beam time. CNRAD [29] was suitable in terms of possible equipment size and radiation environment, but the tests were performed parasitically and therefore there were constrains including the access conditions, unavailability of cooling water, the length of the access tunnel, etc. Moreover the area operation stopped in 2012. Therefore it was decided to build a new area which should be compliant with all the user needs.

H4IRRAD [8] is a new irradiation area, located in the H4 beam line in the North Experimental Area of CERN (for area overview see Figure 33), for testing LHC electronic equipment, especially large volume assemblies such as full-size electronics racks of high current power converters. It uses alternatively a secondary, mainly proton, beam of 280 GeV/c, or an attenuated primary 400 GeV/c proton beam slowly extracted from the CERN SPS directed towards an H4IRRAD target. The test area is separated into several locations aiming to reproduce a radiation field as similar as possible to LHC “tunnel” and “shielded” areas, taking into account the high energy hadron fluence, particle spectra shape, dose maps, 1 MeV Si neutron equivalent, etc.

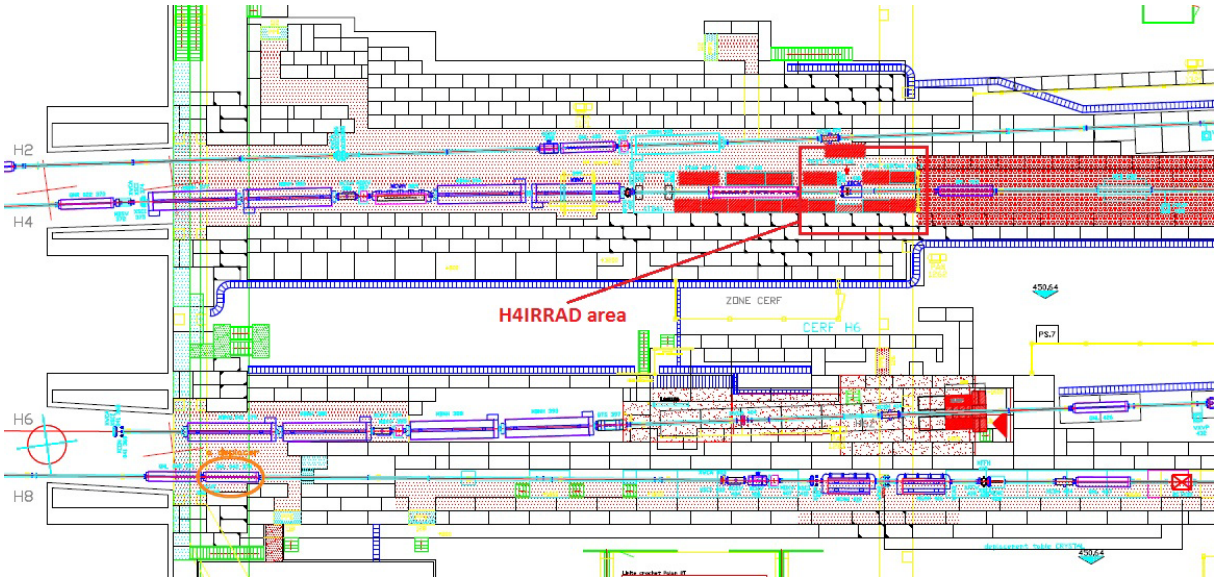

Figure 33: Layout technical drawing of a relevant part of the North Experimental Area with H4 beam line before H4IRRAD refurbishment [44].

5.1 H4IRRAD Design and Radiation Field Studies

5.1.1 Layout and Generic Studies

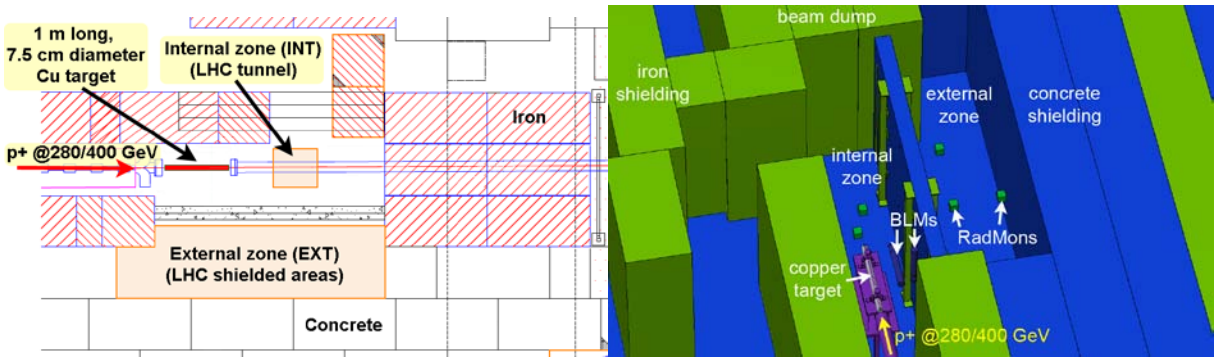

Figure 34: Layout technical drawing (left) [45] and FLUKA model (right) of the H4IRRAD irradiation area with few examples of detector position. The red hatched/green areas indicate iron blocks of the shielding while the white/blue ones are concrete blocks. The beam is arriving from the left/bottom of the picture. The overall shielding around the area is not shown in this extract.

The H4IRRAD area layout drawing and a representative FLUKA geometry are shown in Figure 34 with the two irradiation zones: the internal zone, located downstream the 100 cm long cylindrical copper target with a diameter of 7.5 cm, and the external zone, separated by a concrete wall ("inner shielding"). The internal irradiation area corresponds to the LHC "tunnel" areas, while the external area to the LHC "shielded" locations.

The aim of the design and optimization studies was to establish the radiation field and to evaluate if a reproduction of a mixed field as similar as possible to the one around the LHC is possible. For the first approach, a simplified geometry that is representative to the envisaged irradiation area in the H4 beam line was simulated by the FLUKA Monte Carlo code [32, 33], consisting of a target surrounded by a first ("inner") and second layer of shielding. The internal irradiation area within the first layer (aside and downstream the target) should be representative of LHC "tunnel" locations, while the external irradiation area between the first and second shielding should be representative of LHC "shielded" areas.

For the purpose of optimising the radiation field in the external irradiation location, the influence of the inner shielding material composition and thickness has been studied, aimed at the reproduction of condition as similar as possible to LHC shielded locations. By optimizing the neutron spectra shape with respect to LHC and maximizing the HEH (high energy hadron) fluence, the most favourable setups were found and are listed in Table 3 together with examples of the LHC tunnel and shielded areas. A beam with 10^9 protons of 320 GeV/c over 44 s (giving approximately $1.375 \cdot 10^{13}$ p/week), corresponding to an SPS supercycle, was

assumed for these studies. The beam is considered to have a Gaussian shape with a FWHM in both axis of 2 cm.

Table 3: HEH and neutron fluence fractions for various inner shielding setups (iron + concrete, concrete, polyethylene and no shielding) and examples of LHC tunnel and shielded areas. (Φ_{thn} – thermal neutron (< 0.532 eV) fluence, Φ_{HEn} - high energy (> 20 MeV) neutron fluence, $\Phi_{5\text{-}20MeV}$ – 5-20 MeV neutron fluence, Φ_{HEH} – all high energy hadrons fluence). Statistical uncertainties are not indicated as they are negligible compared to field gradients within the test racks [45, 46].

Setup	Location	Φ_{thn}/Φ_{HEn}	$\Phi_{5\text{-}20MeV}/\Phi_{HEn}$	Φ_{HEH} (/cm^2/week for H4IRRAD) (/cm^2/year for LHC)
20cm Fe + 20cm Con	INT	1.1	0.53	5.1E+10
	EXT	12.1	0.34	7.3E+08
20cm Con	EXT	5.0	0.45	2.8E+09
10cm PE	EXT	3.3	0.44	3.9E+09
No Sh	EXT	5.3	0.81	4.7E+09
LHC	IR1 Q6 - tun.	5.6	0.48	≤1E+10
	IR1-RR13/17	26.5	0.46	1.0E+08 – 1.0E+09

The inner shielding setup combining an iron and concrete lining seems to have the most similar spectrum to the LHC shielded areas such as IR1-RR13/17. However, the HEH fluence is strongly suppressed (a factor of 5 lower than for the pure polyethylene setup). Finally as the best compromise between achieving a maximal HEH fluence with a minimal HEH gradient within the test location (which is very significant especially for the setup without the inner shielding, but also for the polyethylene one) and particle spectra shape, the 20 cm concrete inner shielding was chosen for the final configuration.

5.1.2 Particle Spectra and Radiation Levels

For studies of performance of the proposed area, the complex FLUKA model of the final area layout was simulated (for a detail of the geometry see Figure 34, right). A "nominal" (for 2011 operation) H4IRRAD beam of 10^9 280 GeV/c protons per 44 s SPS supercycle is used.

The simulated energy neutron spectra in the H4IRRAD internal and external test locations are compared with examples of the LHC "tunnel" and "shielded" areas, respectively, in Figure 35. The ratio between thermal and high energy neutron fluence is well reproduced for the H4IRRAD internal zone (Figure 35, top). The thermal neutron component in the H4IRRAD external zone is lower than in the shielded LHC locations (Figure 35, bottom) due to the massive combined concrete/iron shielding employed in areas such as IR1-RR13/17, but still conformable for the requirements of the radiation tests. Nevertheless the

ratio between thermal neutron and high energy hadron fluence (so called R-factor) has to be taken into account when analysing the radiation failure test results. For the purpose of these studies, energy of ~0.532 eV (corresponding to the FLUKA energy group #239) was considered as an upper limit for the thermal neutrons.

To complete the information about radiation field around LHC, the expected integrated dose for nominal LHC operation is below 100 Gy/year for the tunnel locations and below 1 Gy/year for the shielded locations [47].

Figure 36 presents the simulated neutron spectra 1 m downstream the target directly at the beam height, above and below it (i.e. above the centre of the internal test position). The high energy tail reaches here much higher energies compared to the standard positions in both the internal and external racks. This is very convenient especially for SEE tests of small components.

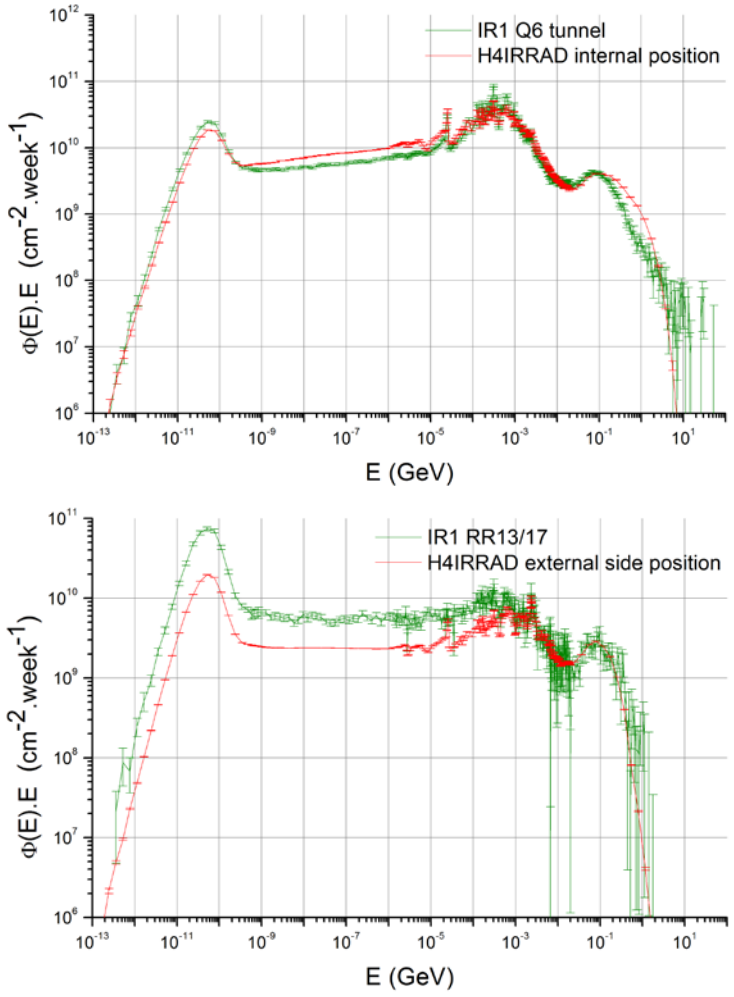

Figure 35: Simulated H4IRRAD neutron spectra in the internal (top) and external (bottom) test location in comparison with the LHC "tunnel" IR1-Q6 and "shielded" IR1-RR13/17 location, respectively. Spectra are normalized at the 100 MeV point [45].

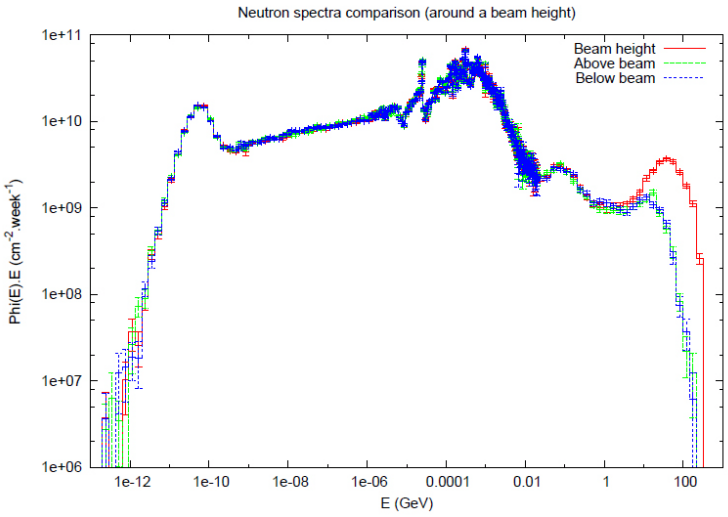

Figure 36: Simulated H4IRRAD neutron spectra at the beam height and 5 cm above and below the beam height, 1 m downstream the target.

Typical prompt dose, HEH fluence and Si 1 MeV neutron equivalent fluence for specific test locations (the external "side" location is parallel to the target position and the "downstream" one is parallel to the internal test location), simulated by FLUKA, are listed in Table 4. To have an overall view of these quantities, Figure 37 gives the horizontal and vertical projection of HEH fluence in the test locations, while Figure 38 shows the prompt dose and Si 1 MeV neutron equivalent fluence over the whole H4IRRAD area.

Table 4: Expected average prompt dose (in air), HEH fluence (Φ_{HEH}) and Si 1 MeV neutron equivalent fluence (Φ_{neq}). The values are normalized per week of operation with the nominal beam of 280 GeV. (The results are not comparable with Table 3 because the final test positions don't correspond to the ones in the first simplified model) [48].

Test location	Prompt dose (Gy/week)	Φ_{HEH} (10^9/cm^2/week)	Φ_{neq} (10^9/cm^2/week)
Internal	13.6	22.1	102
External side	2.48	6.76	30.5
External downstr.	2.57	6.22	19.9

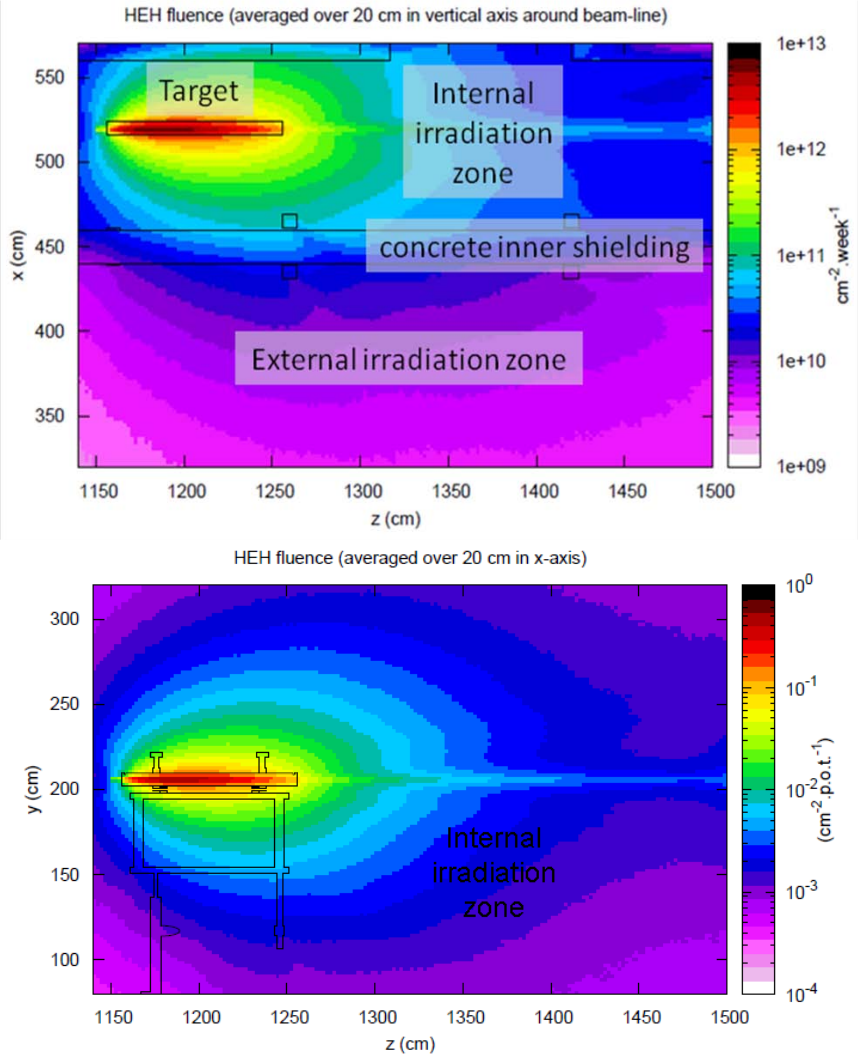

Figure 37: Horizontal and vertical cut of simulated HEH fluence at nominal beam conditions averaged over ±10 cm around beam line position for H4IRRAD test locations.

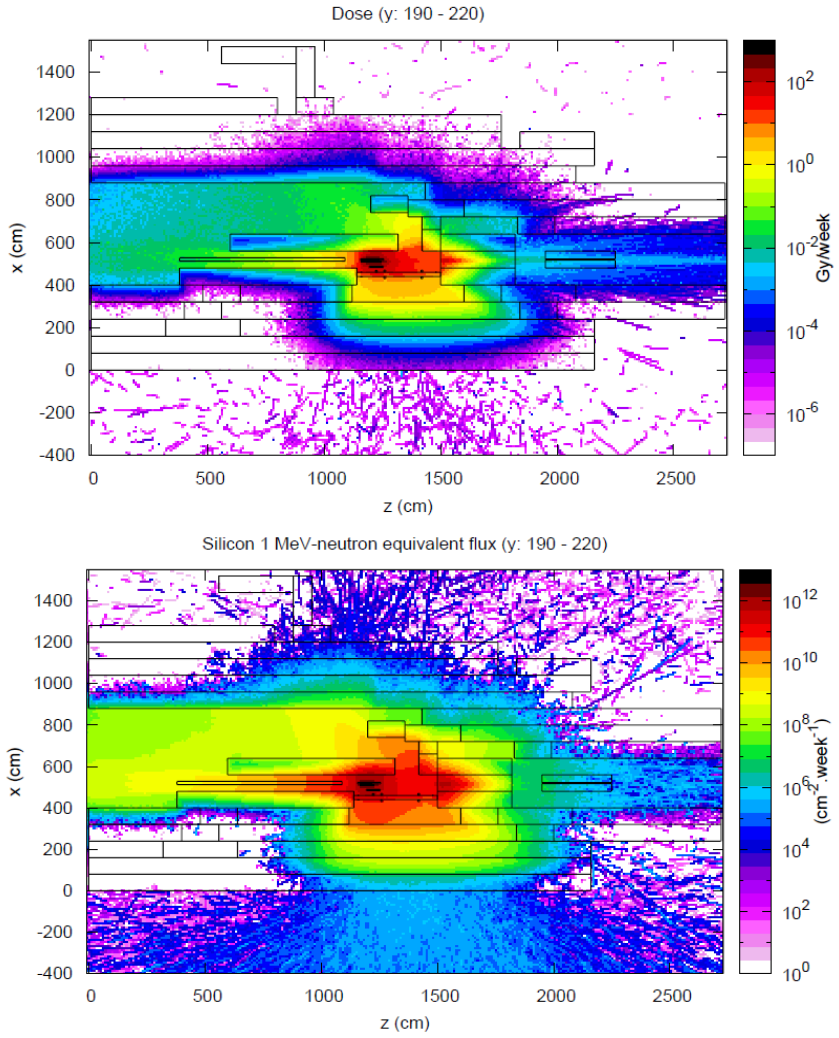

Figure 38: Horizontal cut of simulated prompt dose in air (top) and Si 1 MeV neutron equivalent fluence (bottom) at nominal beam conditions averaged over ±15 cm vertically around the beam height for the whole H4IRRAD area [48].

For the scope of equipment tests, not only the radiation level is important but also its gradient. It shouldn't be too high over the locations where the equipment is expected to be tested to allow to have a well characterised fluence within a single tested (e.g. power converter) rack. The radiation uniformity was studied in the internal and external test zone as a high energy hadron fluence profile. Figure 39, 40 and 41 present 1D projections of HEH fluence in areas of interest with marked expected positions of the tested racks and the field gradient along racks dimensions. Figure 39 represents a longitudinal projection along the beam line (averaged over 4x4 cm^2 around the beam line) and along the external location length (averaged over 20x20 cm^2 around a longitudinal axis passing through the racks centres), while Figure 40 and Figure 41 represent projections along vertical axes passing through the centre of each rack.

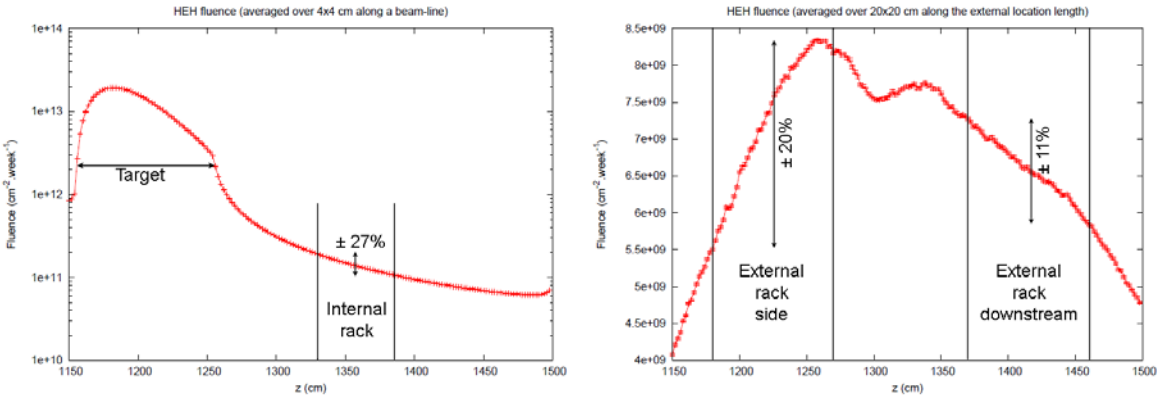

Figure 39: HEH fluence gradient along the H4IRRAD beam line and along the external test location.

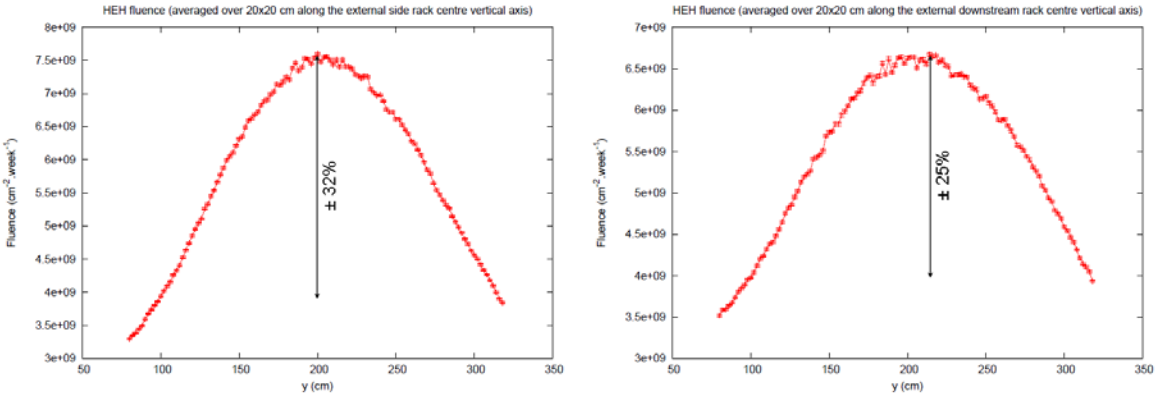

Figure 40: HEH fluence gradient along vertical axes of both external racks – side (left) and downstream (right) test position.

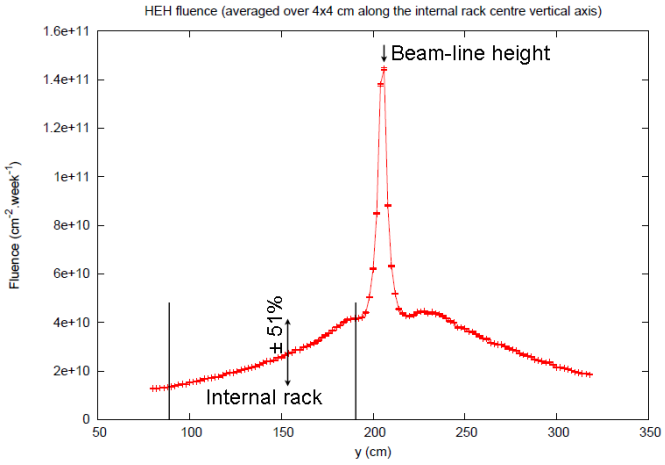

Figure 41: HEH fluence gradient along the internal rack vertical axis.

For quantification of a HEH fluence gradient in various testing locations, three regions in all three racks were selected, reflecting typical tested equipment dimensions (20 cm high in the external racks and 10 cm high in the internal one) – at the top, in the middle and at the bottom. The internal rack top is 16 cm below the beam-line axis (although equipment testing at the top of the rack in a target height is also possible). The average HEH fluences and their

standard deviations (which reflect the HEH fluence gradient) over each region are presented in Table 5. For the external side rack we reach slightly higher HEH fluence than for the downstream one (in accordance with Table 4), but also higher fluence differences. Nevertheless, the gradient in all test locations is acceptable. The information about the gradient is important for choosing the proper position for different equipment.

Table 5: Average HEH fluence within the test locations with its standard deviation (giving the field gradient).

	HEH fluence ($week^{-1}.cm^{-2}$)		
Position	**Internal**	**External Side**	**External Downstream**
Top	4.0E+10 (±18%)	5.0E+09 (±20%)	5.0E+09 (±13%)
Middle	2.4E+10 (±13%)	7.6E+09 (±27%)	6.7E+09 (±17%)
Bottom	1.5E+10 (±8%)	4.1E+09 (±25%)	4.3E+09 (±10%)

Since there is a wide range of tested equipment with various dimensions that can be installed to various parts of irradiation zones, it is necessary to determine the particle fluences and their gradient for each equipment. Values for some equipment tested during 2011 H4IRRAD operation are shown as an example. A 60A power converter (with x/y/z dimensions of 36/26/44 cm or 44/26/36 cm for the 2nd and the 1st irradiation slot, respectively) was tested in the internal location (centre approximately 45 cm below a beam line axis) during the 2nd irradiation slot and received average cumulative fluence of approximately $4.13 \cdot 10^{10}$ HEH/cm^2 with standard deviation over its volume of 14 % (with cumulative number of protons on target of $1.94 \cdot 10^{13}$ p.o.t. during the 2nd slot). The same device was tested during the 1st irradiation slot in the external location at a side (with respect to the target) position and received cumulative fluence of $8.12 \cdot 10^{9}$ HEH/cm^2 with standard deviation over its volume of 18 % (with cumulative number of protons on target during the 1st slot of $1.27 \cdot 10^{13}$ p.o.t.). At the external downstream position a 600A power convertor (with x/y/z dimensions of 60/26/84 cm) was tested during the 2nd irradiation slot and received average cumulative fluence of $9.02 \cdot 10^{9}$ HEH/cm^2 with standard deviation over its volume of 17 %. More details about equipment tests will be provided in section 5.4.

5.1.3 Radiation Protection Studies

From the radiation protection point of view the most critical points are the prompt dose outside the area in order to assess safety risks and eventually for defining the access conditions during operation; the air activation of the area and residual dose rate of equipment are also critical for specifying the access condition and for handling the equipment after the irradiation period.

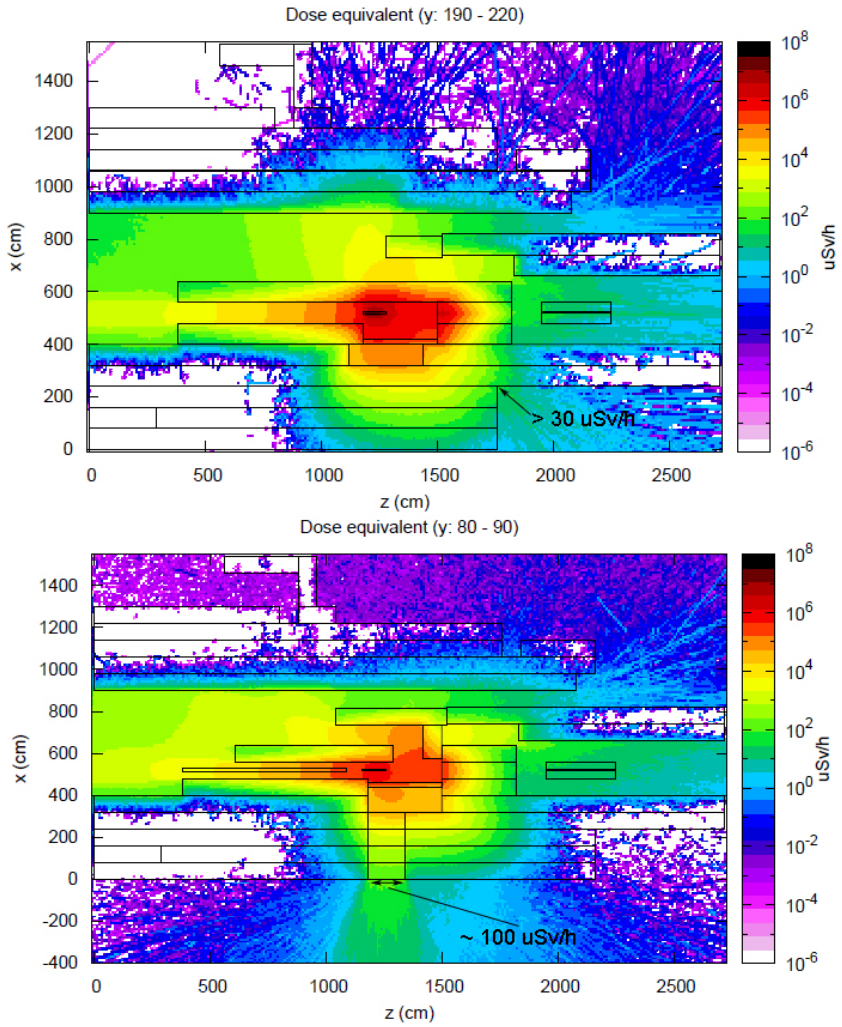

Figure 42: Horizontal cut of simulated ambient prompt dose equivalent rate in µSv/h for the first area layout concepts. Top: averaged over ±15 cm vertically around the beam height – insufficient shielding. Bottom: averaged over 10 cm vertically above the floor (the target and the beam pipe are displayed for better orientation) – cable passages danger.

As a first task, the shielding around the irradiation area had to be optimized. Some weak points of the original area layout are visible in Figure 42. The first projection of ambient dose equivalent shows that the original area shielding was not sufficient. In the marked critical point the dose equivalent would reach 30 µSv/h (for the safety limits see below), so there was the need to adjust the shielding. The second projection (at the bottom; note already prolonged shielding) displays a consequence of one of the cable passages. Some of these 10 cm high gaps above the floor are not used anymore, but the streaming through it could cause dose equivalent up to about 100 µSv/h outside the H4IRRAD shielding. This value is unacceptable, so it has been necessary to shield or displace the cable passages at least at the most exposed positions. In order to allow cabling between the testing locations and the control racks installed in the combined H4IRRAD/CERF cage (located between the H4 and the H6 lines), a 20 cm thick gap/maze in the roof has been designed. This solution is much more practical when the equipment is handled through the roof (more details in section 5.2).

Finally to improve the shielding, a part of the second (from outside) concrete shielding layer was replaced by iron.

Figure 43 gives the average prompt ambient dose equivalent for the final H4IRRAD layout (after all the iterations to satisfy safety requirements) for nominal beam of 280 GeV/c. At the position "X" (left part), located in accessible, non-permanent work area, the dose equivalent is expected to reach 0.6 ± 6 % µSv/h. This value is well below the allowed limit for a low-occupancy supervised radiation area (which is the classification of the North Area Experimental Hall) of 15 µSv/h [41]. Directly above the roof opening of the cable passage, the maximal dose equivalent is expected to reach up to around 100 µSv/h (right part of Figure 43), therefore access to the roof locations is blocked during H4IRRAD operation [48].

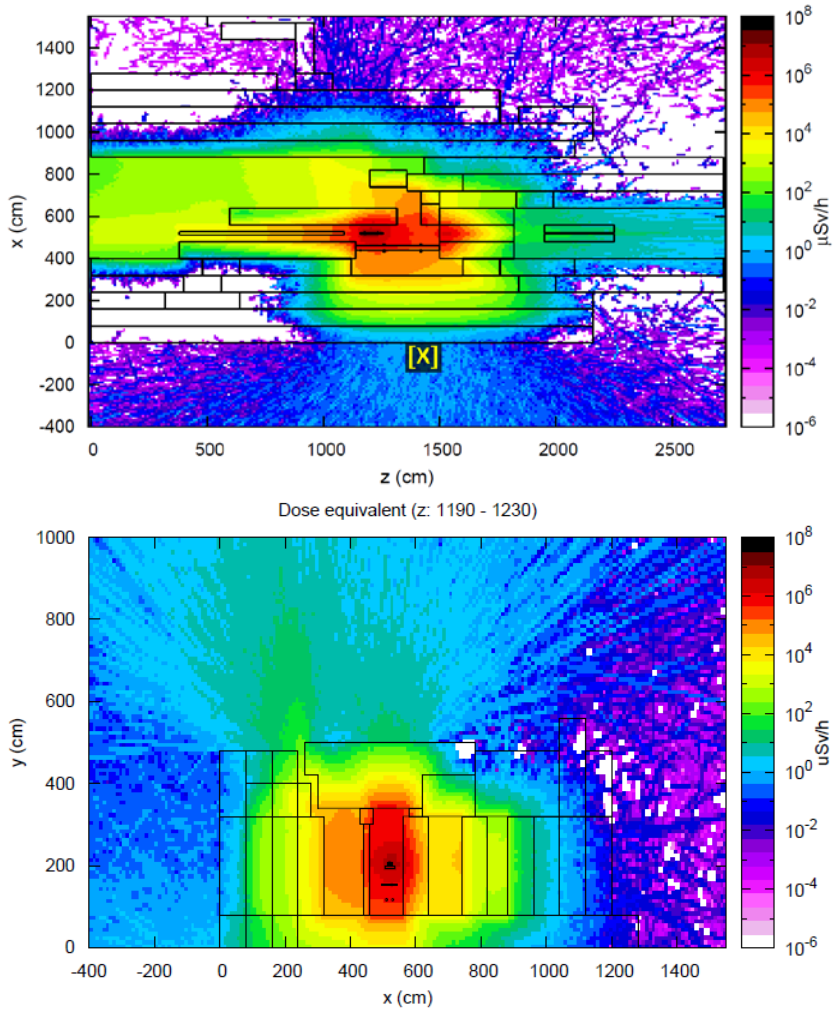

Figure 43: Horizontal (top) and vertical (bottom) cut of simulated ambient prompt dose equivalent rate in µSv/h for the final H4IRRAD installation at nominal beam conditions averaged over ±15 cm vertically around the beam height and over ±20 cm horizontally around the target centre, respectively. The dose equivalent rate was evaluated for position X and above the roof (see text) [45].

The average muon fluence directly behind the iron beam dump (3.2 m long) reaches $3.3 \cdot 10^6$ muons/cm^2/week corresponding to a dose equivalent of 6.2 µSv/h. 8.5 m further downstream, the fluence decreases to $8.6 \cdot 10^5$ muons/cm^2/week (corresponding to a dose equivalent of 1.6 µSv/h). These locations are still inside the beamline area, thus not excessible during operation.

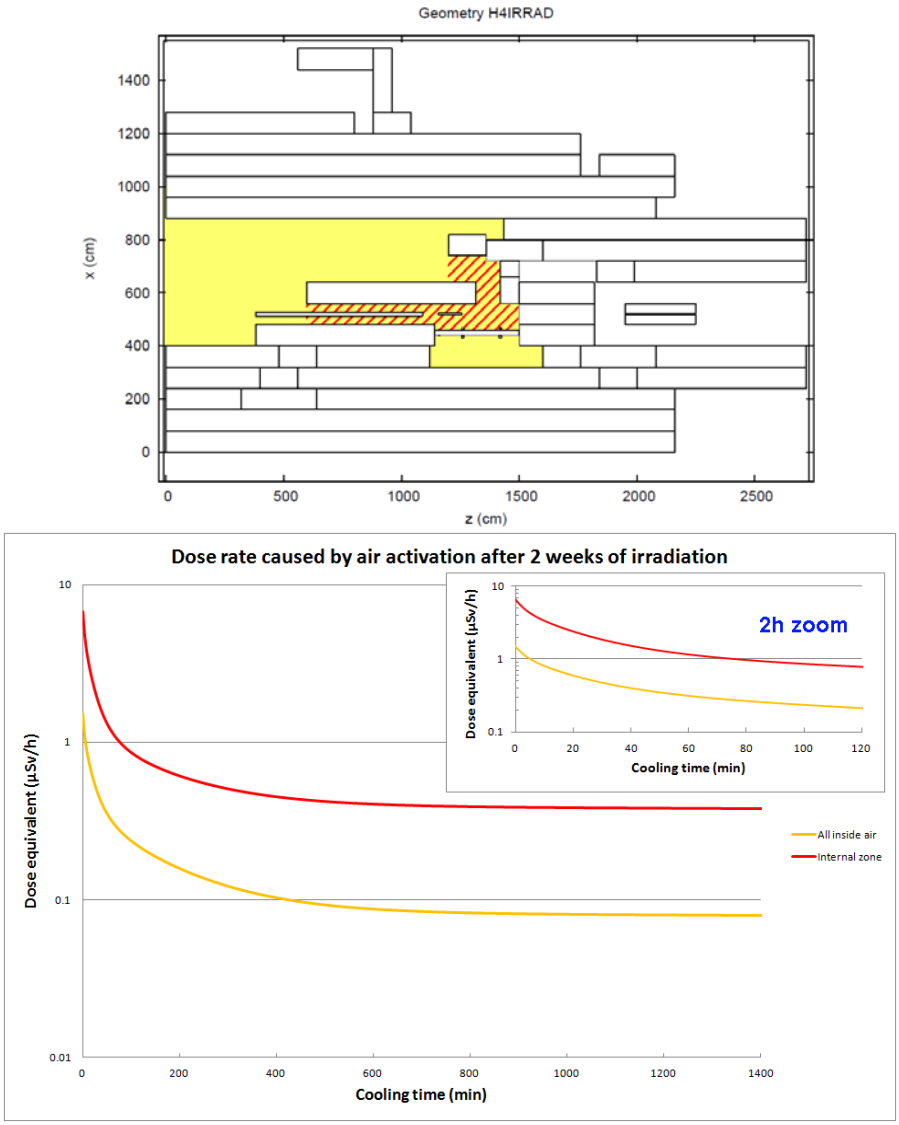

Figure 44: Subarea delimitation in H4IRRAD geometry for air activation studies (left) and rate of committed dose caused by air activation after 2 weeks of irradiation with the nominal beam of 280 GeV/c for two subareas (right) - the chart colours correspond to the area colours. The worst case scenario of no air exchange is assumed.

A conservative estimation of the air volume around the H4IRRAD target, including both test areas and the H4 beam line tunnel up to 11 m upstream from the target (yellow area in Figure 44, top), was used for the air activation studies. The yellow curve in Figure 44 (bottom) represents a decrease of the rate of committed dose, caused by air activation after two weeks of continuous operation with the nominal beam of 280 GeV/c. The worst case

scenario of no air exchange or leakage during or after the operation is assumed. Under these conditions the average air activation would decrease below 1 µSv/h after approximately 5 minutes of cooling time. Assuming only the internal test zone volume along the tunnel 5 m upstream (red hatched area in Figure 44, top) with the worst case scenario, a cooling time of 75 minutes would be needed to drop below 1 µSv/h (red curve in Figure 44, bottom). The procedure to establish the rate of committed dose due to presence in radioactive air was developed by the CERN Radioprotection group and is explained in [49].

The residual dose equivalent rate of the H4IRRAD instrumentation (the target, its table and the beam dump) and a model of the tested equipment after 20 days of operation with nominal beam of 280 GeV/c and for various cooling times is summarized in Table 6. The activation of the Cu target and its support table is not negligible, therefore special handling conditions have to be applied when target removal is requested. A model of an electronic circuit board with a typical elemental composition (according to [50], see Table 7) was implemented to the FLUKA geometry and located inside internal/external test rack (here so called internal and external circuit). However, some electronic components with non-standard content of especially heavy elements can be activated several times more. We have to count with a higher activation also for the components tested at the top of the internal rack around the beam height (this increase of activation is obvious result of spectra differences visible in Figure 35 and Figure 36).

Table 6: Residual dose equivalent rate (skin to material contact) for H4IRRAD instrumentation and test equipment after several cooling times, assuming 20 days of irradiation with nominal beam conditions. Statistical uncertainties are not indicated as they are negligible.

	Residual dose equivalent (µSv/h)		
Cooling time	**1 hour**	**1 day**	**1 month**
Target	218	104	31.1
Target table	160	52.2	0.73
Beam dump	8.66	4.38	0.79
Int. circuit	6.74	3.08	0.73
Ext. circuit	3.22	1.17	0.22

Table 7: Chemical composition of electronic circuit boards obtained from the analysis of scrap in recycling facilities. The density ρ of the material compound equals 3.37 g/cm^3 [50].

Element	Weight (%)	Element	Weight (%)
Al	5	**Ni**	1
Sn	3	**Zn**	1
Fe	5	**Au**	0.025
Cu	16	**Pb**	2
Ag	0.1		
Epoxy (C18H19O3)	66.875		

In 2012, H4IRRAD operated using an attenuated primary proton beam of 400 GeV/c instead of the secondary beam of 280 GeV/c (like in 2011) and a factor of three higher intensity. This had a significant contribution to the efficient use of the area, while impact on the radiation field spectra and the dose equivalent level outside the area is minimal. Nevertheless, the target activation increased significantly. A new study was done in the beginning of 2012, taking into account the activation from 2011 and using a 2012 SPS schedule. Already after the first 2012 irradiation slot of 19 days with the proton beam of 400 GeV/c and $3 \cdot 10^9$ protons per 44s SPS cycle, the residual dose equivalent rate was predicted to be 1.9 mSv/h for the cooling time of 1 h. Therefore a special target lead (Pb) shielding was designed and used for 2012 operation prior to interventions in the target zone to limit its contribution to the ambient dose during access.

5.2 H4IRRAD Commissioning and Operation

The H4IRRAD was built in a short period to cover the needs of LHC in testing large volume electronic assemblies (e.g. high current power converters) using a beam of reduced intensity to ease the accessibility for the users, compared to other high-intensity facilities (see chapter 2). The test area has been setup during the first months of 2011 and has started operation in June 2011, using a secondary beam of 280 GeV/c (mainly) protons from SPS.

5.2.1 Area Construction

The implementation of the irradiation zone in the H4 area was a task that required many iterations and went through several modifications according to general irradiation area requirements and gradually evolving simulations (mostly covering the radiation protection issues and optimization of the radiation field in the testing locations) and users requests. The main modifications with respect to the original version concerned the external shielding configuration, the internal Fe lining as well as the installation of a new copper target and of

the respective movable table. Also the control cage outside the H4IRRAD shielding used by CERF facility [51] (installed in neighbouring H6 beam-line) was refurbished to H4IRRAD/CERF control cage. For the H4 area changes you can compare the horizontal technical drawing of the final layout in Figure 45 with the old area layout in Figure 33.

Figure 46 shows vertical cut through the installed 320 cm long iron beam dump, of the irradiation areas (with 160 cm thick iron roof) and the 20 cm thick concrete internal shielding. Some of the iron blocks can be removed (green hatched parts) in order to access the irradiation areas from the top and to install the beam pipe (instead of the beam dump) during the time periods when area is not operating. Two special platforms, able to carry the heavy test equipment, were designed in order to permit their lowering into the internal and external test areas from the top, using the overhead crane of the building. This semi-remote operation allows for the exchange of user equipment with limited access to the irradiation areas and resulting exposure to radiation. The cable gap in the removable roof is also visible in the lower drawing.

The irradiation area (detailed view in Figure 34) is divided into two irradiation zones. The internal one is located just downstream the target in the same area (between the target and the iron beam dump), while the external irradiation location, placed aside the target area, has been created by removing of few blocks of a concrete shielding and by replacing of a part of the old iron shielding with 20 cm thick concrete wall, called inner shielding, as a best configuration indicated by the generic studies (as mentioned above in section 5.1.1). The 100 cm long cylindrical copper target with a diameter of 7.5 cm is placed behind a present bending magnet (MBNV 410, currently not used) downstream of the old T24 target. The target is held on a vertically movable table visible in Figure 47. The vertical movement of the aluminium table is integrated in the CESAR control system of the North Area and allows remote movement and monitoring.

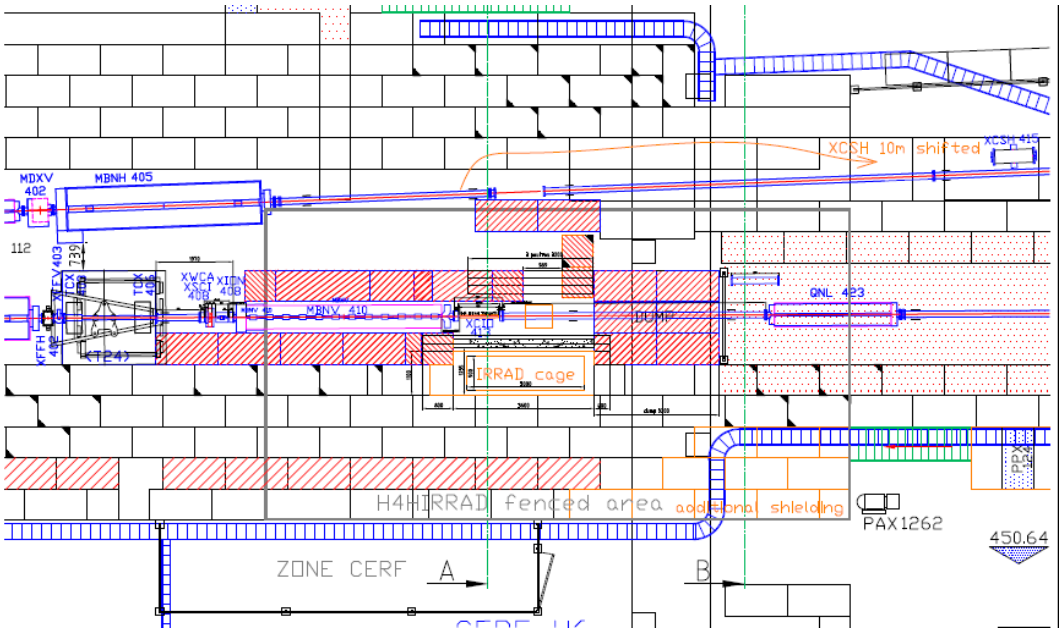

Figure 45: Technical drawing of a relevant part of the North Experimental Area with H4 area final layout (top view). The red hatched areas indicate iron blocks of the shielding while the white ones are concrete blocks [52].

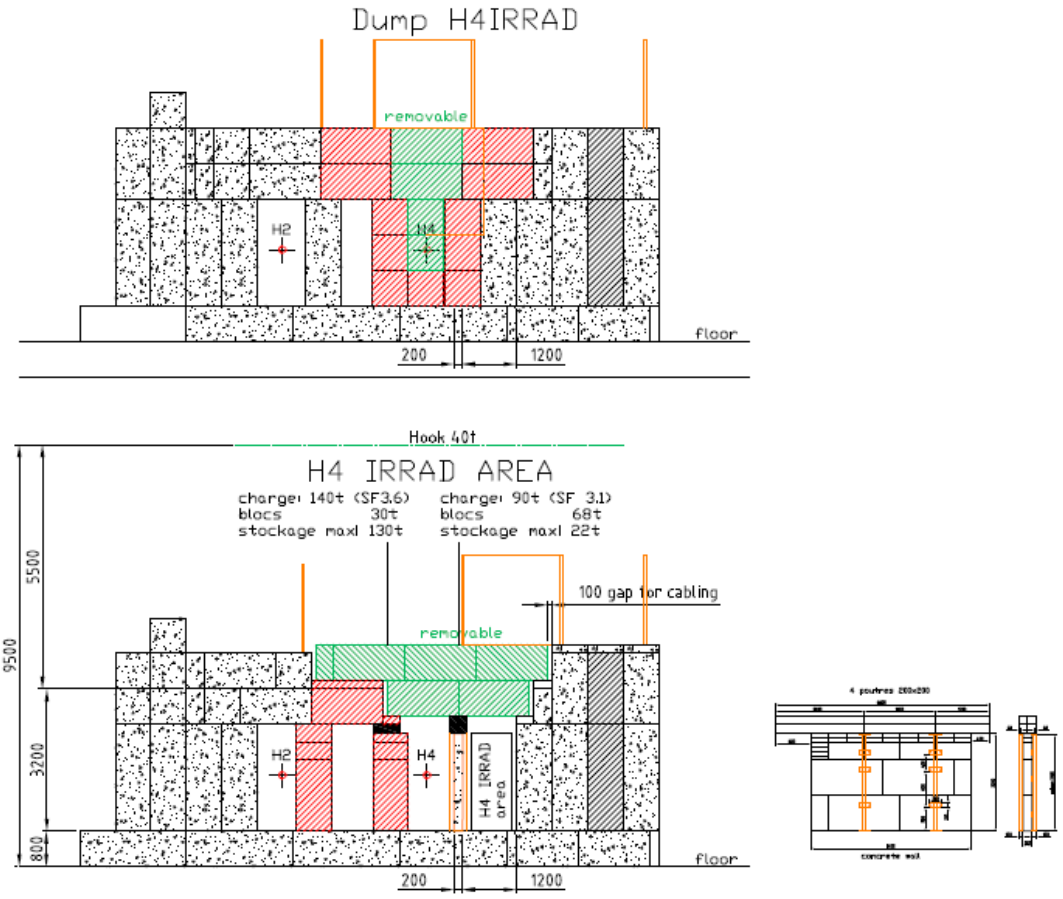

Figure 46: Technical drawing of H4IRRAD iron beam dump (upper plot) and irradiation areas (lower plot) with marked removable iron parts (vertical view from H4 upstream, dimensions in mm) [52].

Figure 47: H4IRRAD copper target on a movable table [53].

Assuming "generic studies" conditions (i.e. 320 GeV/c proton beam, target diameter 8 cm etc., see section 5.1.1), the total energy deposited in the H4IRRAD target is equivalent to 206.9 GeV/primary. If the area operates with an intensity of 10^9 protons/pulse, the total deposited energy per pulse is 33.5 J/pulse, equivalent to 0.75 W, assuming a supercycle of 44 s. Even with an intensity of 10^{10} protons/pulse the average deposited power will remain within very low limits, ~7.5 W. Given these low limits, no cooling system was envisaged for this setup. The peak power deposition, thanks to the large beam area, will not exceed 0.16 J/cm^3 for pulse of 10^9 protons [54].

5.2.2 Beam Conditions and Monitoring

The primary beam is extracted from the SPS at 400 GeV/c. The beam can be alternatively attenuated and used with the original energy and lower intensity (like during 2012 H4IRRAD operation), or it is steered towards the T2 target with an intensity of $6 \cdot 10^{12}$ (2011 H4IRRAD operation). The secondary beam with the energy of 280 GeV/c or the attenuated primary beam passes through H4 beam line various beam optics and collimators and impacts on the H4IRRAD copper target with an intensity of $1 \cdot 10^9$ particles/pulse or $3 \cdot 10^9$ particles/pulse, respectively, as seen in Figure 48. The beam particle composition (mainly protons with smaller contribution from pions and kaons) is listed in Table 8.

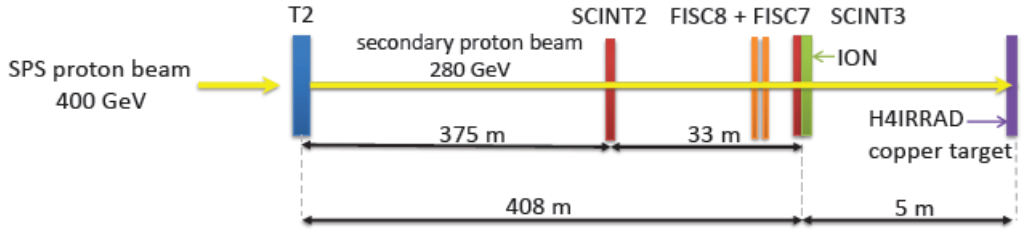

Figure 48: Sketch of the secondary H4 beam line showing the beam extraction from SPS on the T2 target to the H4IRRAD copper target with beam monitoring systems (SCINTs, FISCs and ION, see text) [45]. For the whole beam line layout see Appendix A.

Table 8: H4 secondary beam composition [55].

Particle	Content (%)
protons	94.27
pions	5.01
kaons	0.72

One of the crucial input parameters for the radiation field simulations is an accurate knowledge of the beam profile. In order to determine it, several tools are available. Filament scintillator (FISC) is a motorised wire scanner with a 0.2 cm wide filament. FISC8 and FISC7, located 402 m and 403 m downstream of the T2 target (see Figure 48), provide the horizontal and vertical profile of the secondary beam, respectively. Figure 49 shows these measurements for the first and second irradiation period of 2011. While the vertical profile follows a Gaussian shape, the horizontal one shows a double-peak pattern.

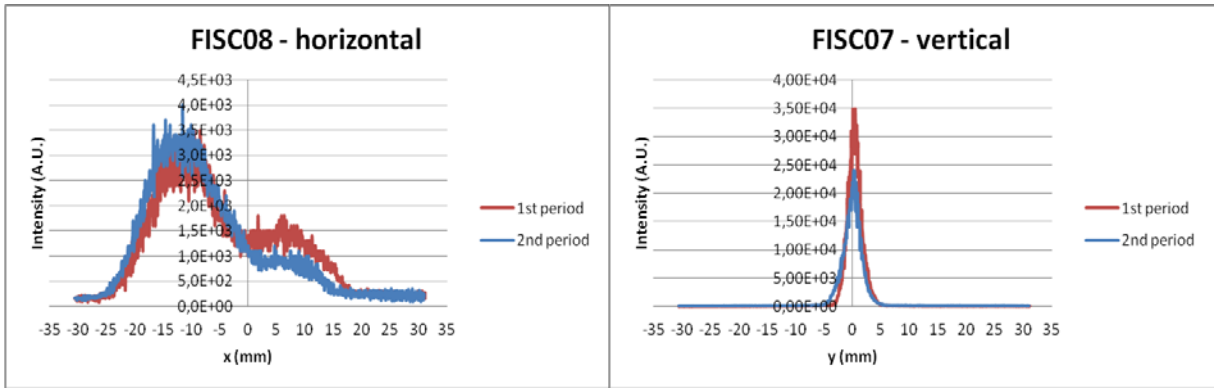

Figure 49: H4 beam profile measurements for the 2011 1st and 2nd irradiation slots provided by wire scanners FISC8 (left, horizontal profile) and FISC7 (right, vertical profile).

To visualize the beam profile and alignment directly at the H4IRRAD target position, a false aluminium hollow target with a possibility to attach a photographic plate to its each end has been constructed. Two different kinds of photographic plates have been used, i.e. Polaroid© film and Gafchromic EBT2© Dosimetry film. The resulting image of Polaroid film measurement from the front target end is shown in Figure 50 with superposed horizontal

FISC8 profile. The Polaroid film does not give a quantitative intensity evaluation due to high intensity of the beam, but a good qualitative agreement with the wire scanner output is observed. A special source routine (a user-written program) was programmed by the author as an input for FLUKA simulations using directly the output data from the wire scanner. The resulting simulated beam profile is depicted in the right part of Figure 50.

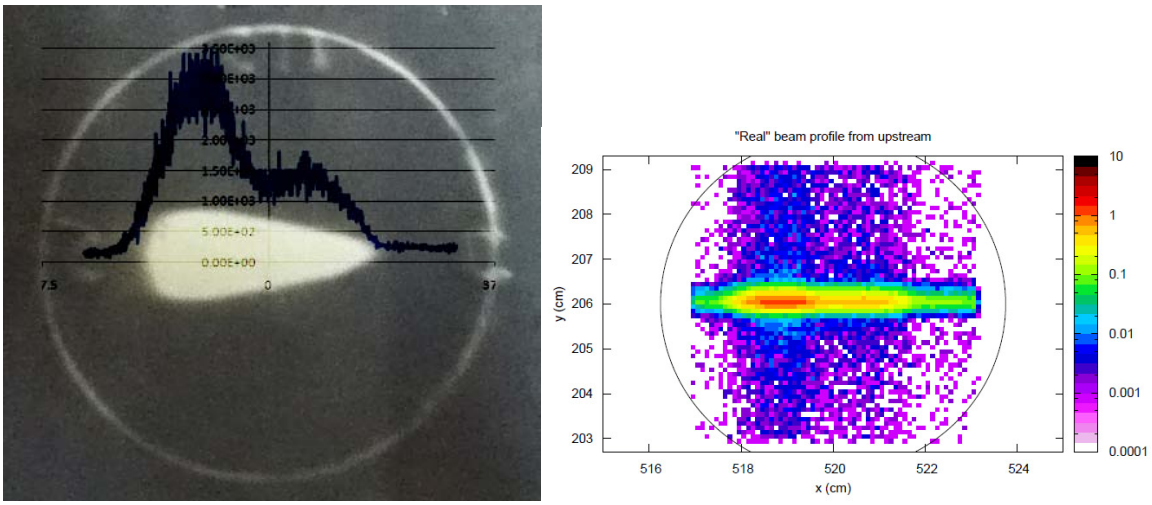

Figure 50: Superposition of the secondary beam profile measurement performed by the Polaroid film and by FISC8 (left) [48] and the beam profile representation by FLUKA simulation (right).

For the 2012 operation year a new tool was available. The GEM (Gas Electron Multiplier), a special type of gaseous ionization detector, was installed approximately 30 cm upstream of the H4IRRAD target front end, giving both horizontal and vertical beam profile. Its close proximity to the target is a useful improvement, thus the GEM profile was used (instead of FISC7/8) as a FLUKA simulation input for 2012 test periods. The attenuated primary beam has a single-peak profile in both horizontal and vertical projections (contrary to the secondary beam) as visible in Figure 51.

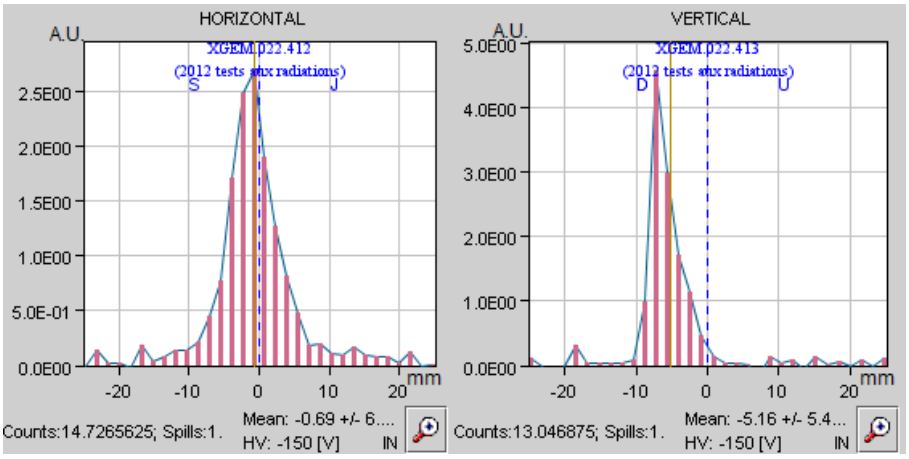

Figure 51: The horizontal (left) and vertical (right) attenuated primary beam profile measured by GEM detector (~30 cm upstream the H4IRRAD target).

For better understanding of the beam profiles in different beam monitors, the whole H4 beam line was simulated by G4beamline [40] tool. It reproduced well the measured profiles, however the double-peak observed during 2011 operation was not visible in the simulated results.

The other essential simulation input parameter is the number of particles impinging the target ($N_{p.o.t.}$; p.o.t. – particle on target), measured by the beam monitoring system. This system consists of an ionisation chamber (ION), two scintillators (SCINT2 and SCINT3) and a precision ionisation chamber (PIC).

The ION, filled with pure argon slightly above atmospheric pressure, consists of stainless steel cylinder, two thin windows and 21 parallel 2 μm thick aluminium electrodes. These detectors are widely used at CERN secondary beams for their long term stability and linear response to fluxes raging from 10^5 to 10^9 charged particles/spill (bridging the range of scintillators and high flux e.g. foil activation techniques). A detailed description can be found in [56].

Plastic scintillators are a common tool in the North Area for monitoring the secondary beam lines. For the H4IRRAD beam monitoring SCINT2 and SCINT3 (see Figure 48) are used in coincidence. They are 4 mm thick with a diameter of 100 mm and are sensitive to fluxes raging from 10^5 to 10^7 charged particles with a high efficiency. While they cannot be used to measure the nominal intensity, they are very useful for calibration as described below.

The PIC is a transmission-type parallel plate ionisation chamber with a diameter of 185 mm. It contains five parallel Mylar electrodes with a thickness of 2.5 mg/cm^2 and inter-plate spacing of 16 mm. The central electrode works as a collector and the other ones as polarity electrodes. The PIC was mounted approximately 2 m downstream from the H4IRRAD target centre and was used only during commissioning period when the target was removed.

While the ION, which measures the beam intensity in counts (ION counts), has a linear response up to the nominal H4IRRAD intensities (order of 10^9 p.o.t./spill), the scintillators, which measure directly the number of charged particles, have linear response only up to order of 10^7 p.o.t., as described above. The overlapping intensity region between a few 10^5 and 10^7 p.o.t./spill with a linear response of both detectors was used to relate the ION

counts to the $N_{p.o.t.}$ measured by SCINT2 and SCINT3 in coincidence. This calibration was performed during the area commissioning in June 2011 resulting in a calibration factor of 6600 p.o.t./(ION count). The crosscheck of the calibration was performed several times during the first weeks of operation and showed a degradation of the scintillator response (decreasing calibration factor was measured) due to its aging caused by the high received cumulative dose. The scintillators were replaced before the third irradiation slot (October 2011) and could be used again for the ION calibration.

To receive a precise beam intensity measurement a further calibration was performed using the PIC. As a first step it had to be also calibrated to measure directly $N_{p.o.t.}$. Its calibration was performed in the past using scintillators (as described above) and verified by an activation technique. The activation of calibrated aluminium (Al) foil, based on induced γ activity of ^{24}Na produced in the Al foil through $^{27}Al(p,x)^{24}Na$ reaction, was performed at CERF (details about this experiment and PIC calibration given in [57]) and repeated in July 2011 for H4IRRAD area. The results from these PIC calibrations showed an agreement within 5 %. The cross-calibration between PIC and ION was performed afterwards on the intensity interval from 10^5 to 10^9 p.o.t./spill.

During irradiation slots the $N_{p.o.t}$ is obtained by multiplying the ION counts by the ION calibration factor. For example during the first 2011 irradiation slot a total of $12.7 \cdot 10^{12}$ p.o.t. was delivered (for the other slots it was generally more, especially during 2012 with the beam intensity increase). For the periods when the ION was not operating properly (due to the misconfiguration of a bending magnet), the radiation monitors (see the next section) were used as a beam intensity indicator. Detailed information about the beam monitoring calibration is given in [48].

5.2.3 Radiation Field Monitoring

The radiation levels in the test areas produced by the particle shower created by the H4 beam hitting the H4IRRAD target are measured by the radiation monitoring system. It consists of online radiation field monitors, RadMons, and beam loss monitors, BLMs. Both detector systems use the monitors of the same type as in the critical zones of the LHC underground areas.

RadMon system is widely used in the LHC for online monitoring of radiation levels. Around 330 of RadMon modules are installed in the LHC tunnel and shielded areas and serve

as an early warning system to protect the electronic equipment. The detectors can operate on two different sensitivities (3V and 5V bias) and can independently measure three components of the radiation field and thus separate the three different radiation damage effects (see section 1.2). This is achieved by combining three types of sensors (nine sensors in total) in each monitor. These are two radiation sensitive MOSFETs ("Radfets") to measure the total ionizing dose (TID), three photodiodes to measure Si 1 MeV neutron equivalent fluence and four 4Mbit static RAM to measure the thermal neutron and HEH fluence. At H4IRRAD, five RadMons were used at different positions for each slot (sometimes the position was changed even within one slot) to obtain the information about the radiation field over the test locations as complete as possible [58, 59].

The LHC-BLM system consists of around 4000 detectors, protecting the superconducting elements by generating a beam abort trigger if beam losses are recognised (cumulated dose in the chamber exceeds a predefined threshold). The BLM type used in LHC is a cylindrical parallel-plate ionisation chamber with a length of 50 cm and a diameter of 9 cm filled with nitrogen at 1.1 bar. The sensitive part with 61 aluminium electrodes is 38 cm long and the remaining part is used for readout electronics [60]. Two of these BLMs are installed at H4IRRAD close to the target position (at the same height as the target), one aligned horizontally (hBLM) and the other one vertically (vBLM). Their size and position makes them very sensitive to the radiation field gradient.

Several other types of detectors were operated at H4IRRAD, but usually just in a role of tested equipment without a significant benefit for the radiation field monitoring. Some of them will be mentioned in the following sections.

5.3 H4IRRAD Radiation Field Benchmark

The FLUKA simulation results were tuned by the measured $N_{p.o.t}$ in order to obtain the real radiation field levels for detectors and tested equipment positions. The simulated quantities have been compared to the values measured by detectors. In the two following sections, such comparison studies are described.

5.3.1 High Energy Hadron and Thermal Neutron Fluence Benchmark

The RadMon SRAM sensor is used as a Single Event Upset (SEU) monitor. Its response to SEU is estimated using Eq. 5.

$$N_{SEU} = \sigma_{thn} \cdot \Phi_{thn} + \sigma_{HEH} \cdot \Phi_{HEH}\,, \tag{5}$$

where σ and Φ denote the failure cross section and fluence of thermal neutrons and high energy hadrons, respectively. The cross sections, listed in Table 9, depend on a voltage bias of the RadMon detector and were measured using monoenergetic proton beams, quasi-monoenergetic neutron beams and epithermal neutron beams [46].

Table 9: SEU cross sections for the two voltage settings. The associated uncertainties of 10 % are dominated by beam monitoring [46].

Bias	σ_{thn} (cm^2/bit)	σ_{HEH} (cm^2/bit)	$\sigma_{thn}/\sigma_{HEH}$
3 V	1.7E-13 ±10%	7.0E-14 ±10%	2.4
5 V	3.1E-15 ±10%	3.0E-14 ±10%	0.1

In this section, there are presented two comparisons for simulated results and measured data from the first and second 2011 irradiation periods. The RadMon positions during these first two slots are presented in Figure 52 and Appendix B). During the first period, the number of responses to SEU (N_{SEU}) was measured on both biases. Taken the Eq. 5 and cross sections from Table 9, the fluences Φ_{HEH} and Φ_{thn} were extracted and compared with the FLUKA simulation results. Since the RadMons are sensitive also to the neutrons with lower energies than 20 MeV (contrary to charged hadrons), an additional correction had to be applied to the simulated HEH fluence using a Weibull function as described in [61]. The comparison for both uncorrected and corrected results is presented in Table 10. The simulated values of Φ_{HEH} are slightly overestimated, while the values of Φ_{thn} are overestimated by a factor of 2.5 to 3 compared to the measured data. This overestimation could be partially caused by the complicated setup containing many different materials (mainly in the tested equipment, not always known or included in the simulation) as well as the unknowns related to the concrete and iron shielding composition. Another source of the overestimation might be the RadMon voltage inaccuracy. As visible from Table 9, the factor between the cross sections for two voltages is ~55 for thermal neutrons while only ~2.3 for high energy hadrons. Also a potential small uncertainty in the thermal neutron cross section libraries for the surrounding (mainly shielding) materials would cause a large effect on the thermal neutron fluence due to a nature of the thermal neutron behaviour. Taking the average fluence overestimation from this comparison, the simulations for the following irradiation slots were corrected, showing much better agreement between simulation and measurement.

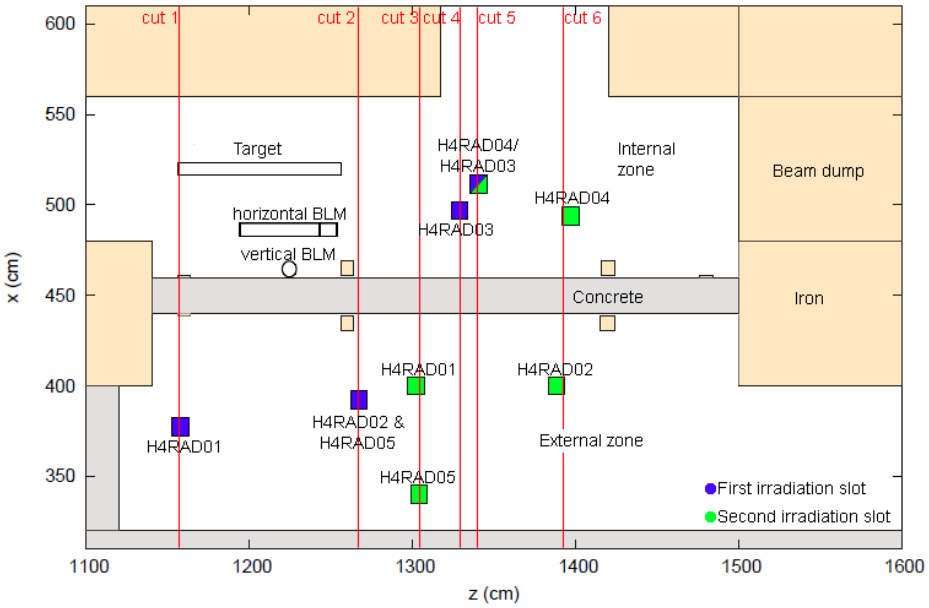

Figure 52: Top view of RadMon positions during the 1st (blue) and 2nd (green) 2011 irradiation periods. The vertical positions (six cut views) are shown in the Appendix B [48].

For the second 2011 irradiation slot, the measurements only on one bias voltage were available. Therefore the measured N_{SEU} was compared to the N_{SEU} calculated from simulated Φ_{HEH} and Φ_{thn} values (using again the Eq. 5 and cross sections from Table 9). The comparison is presented in Table 11, using again the Φ_{HEH} correction on neutrons below 20 MeV and the Φ_{thn} correction based on simulation overestimation, as mentioned in the previous paragraph. After the aforementioned corrections we find a good agreement between the simulation and the measurement (within an error dominated by the uncertainty of the SUE cross section measurement) except for the RadMon5. The simulation overestimation for this device is caused by a radiation attenuation in the tested equipment material in front of the RadMon5 which is not included in the simulation.

Table 10: Comparison of measured (RadMons – notation H4RAD0X) and simulated HEH and thermal neutron fluences (Φ_{HEH} and Φ_{thn}) per particle on target (p.o.t.) for the first 2011 irradiation slot. The high experimental data errors are dominated by the possible variation of cross-section between memory chips. The statistical errors of simulations are negligible, but the position uncertainty could extend these errors up to ~10%. For RadMon positions see Figure 52.

Detector	Measurement	Simulation	Sim./Meas.	Simulation corr.	Sim./Meas. Corr.
	Φ_{HEH} (10^{-3}/cm^2/p.o.t.)				
H4RAD01	0.37±43%	0.32±1.3%	0.85±43%	0.45±1.1%	1.20±43%
H4RAD02	0.37±43%	0.36±1.7%	0.98±43%	0.45±1.2%	1.24±43%
H4RAD03	3.93±43%	4.78±0.4%	1.22±43%	5.07±0.4%	1.29±43%
H4RAD04	1.89±43%	1.65±0.7%	0.87±43%	1.96±0.6%	1.04±43%
H4RAD05	0.69±43%	0.69±1.1%	1.00±43%	0.85±0.8%	1.23±43%
	Φ_{thn} (10^{-3}/cm^2/p.o.t.)				
H4RAD01	0.99±43%	2.90±0.5%	2.93±43%		
H4RAD02	0.95±43%	2.84±0.4%	2.98±43%		
H4RAD03	1.15±43%	3.04±0.6%	2.63±43%		
H4RAD04	1.21±43%	3.29±0.4%	2.71±43%		
H4RAD05	0.99±43%	2.87±0.4%	2.90±43%		

Table 11: Comparison of measured (RadMons – notation H4RAD0X) and simulated number of SEU counts (N_{SEU}) per particle on target (p.o.t.) for the second 2011 irradiation slot.

Detector	N_{SEU} (10^{-10}/p.o.t.)		
	Measurement	Simulation corr.	Sim./Meas. corr.
H4RAD01	5.00±1.1%	4.16±19%	0.83±19%
H4RAD02	3.36±1.4%	3.81±20%	1.13±20%
H4RAD03	8.94±0.8%	8.82±20%	0.99±20%
H4RAD04	5.64±1.0%	5.76±20%	1.02±20%
H4RAD05	1.53±2.0%	2.50±18%	1.63±18%

5.3.2 Dose Benchmark

The dose in the internal test location was measured by two beam loss monitors (BLMs). Their position close to the H4IRRAD target (as described in section 5.2.3 and visible in Figure 52 and Figure 34) remained the same over all irradiation slots (with only 2 cm horizontal shift for 2012 operation year). The measured dose of each BLM has been integrated over several different time periods, when beam conditions were nominal and stable, and corrected for the time-dependent offset (caused by a low current applied for the device functionality feedback). The resulting dose values for the first two 2011 irradiation slots are normalized per respective $N_{p.o.t.}$ and compared with the simulated dose in Table 12.

A very good agreement between simulation and measurement is observed for the horizontal BLM during the 1st slot, while for the vertical one the simulated dose is

overestimated by 10-20 %. This is caused by the fact that the horizontal BLM and its support is placed directly in front of the vertical BLM. This additional material is not fully considered in the simulation. For the 2nd irradiation period comparison a systematic shift to a worse agreement is obvious for both BLMs. This deviation most probably relates to the longer time intervals for the dose cumulation inside the BLMs which are more affected by uncertainties due to time-dependent offset correction.

Table 12: Comparison of simulated and measured dose (in nitrogen) for horizontal (hBLM) and vertical (vBLM) beam loss monitors during the 1st and 2nd 2011 irradiation slots. Statistical uncertainties are negligible, thus not indicated.

Interval	Duration	hBLM dose (10^{-12}.Gy/p.o.t.)			vBLM dose (10^{-12}.Gy/p.o.t.)		
		Simulated	Measured	Sim./meas.	Simulated	Measured	Sim./meas.
1st 2011 irradiation slot							
#1	5 h	10.39	10.22	1.02	4.15	3.65	1.14
#2	15 h		9.75	1.07		3.48	1.19
#3	48 h		10.40	1.00		3.72	1.12
#4	30 h		9.52	1.09		3.48	1.19
2nd 2011 irradiation slot							
#1	37.2 h	10.39	8.90	1.17	4.15	3.24	1.28
#2	65.4 h		9.00	1.15		3.26	1.27
#3	40.1 h		9.48	1.10		3.43	1.21
#4	21.1 h		9.39	1.11		3.40	1.22

5.4 Equipment Tests

During the 2011 and 2012 irradiation periods, several types of power converters and over fifty electronic components/equipment were irradiated as requested either in the internal or the external irradiation zone. They were usually installed inside one of the special platforms (see Figure 53).

For each irradiation slot, the positions of all tested units were implemented to the FLUKA geometry. A dose, HEH fluence, thermal neutron fluence and Si 1 MeV neutron equivalent fluence (Φ_{neq}) were simulated for each of them. After scaling by measured $N_{p.o.t.}$ and normalizing by the correction factors obtained by the comparisons between simulation and measurement (see section 5.3), these values were distributed to the users. Comparing these values with the observed mean time between failures, the failure cross section of the equipment can be obtained as the most important outcome of the H4IRRAD tests.

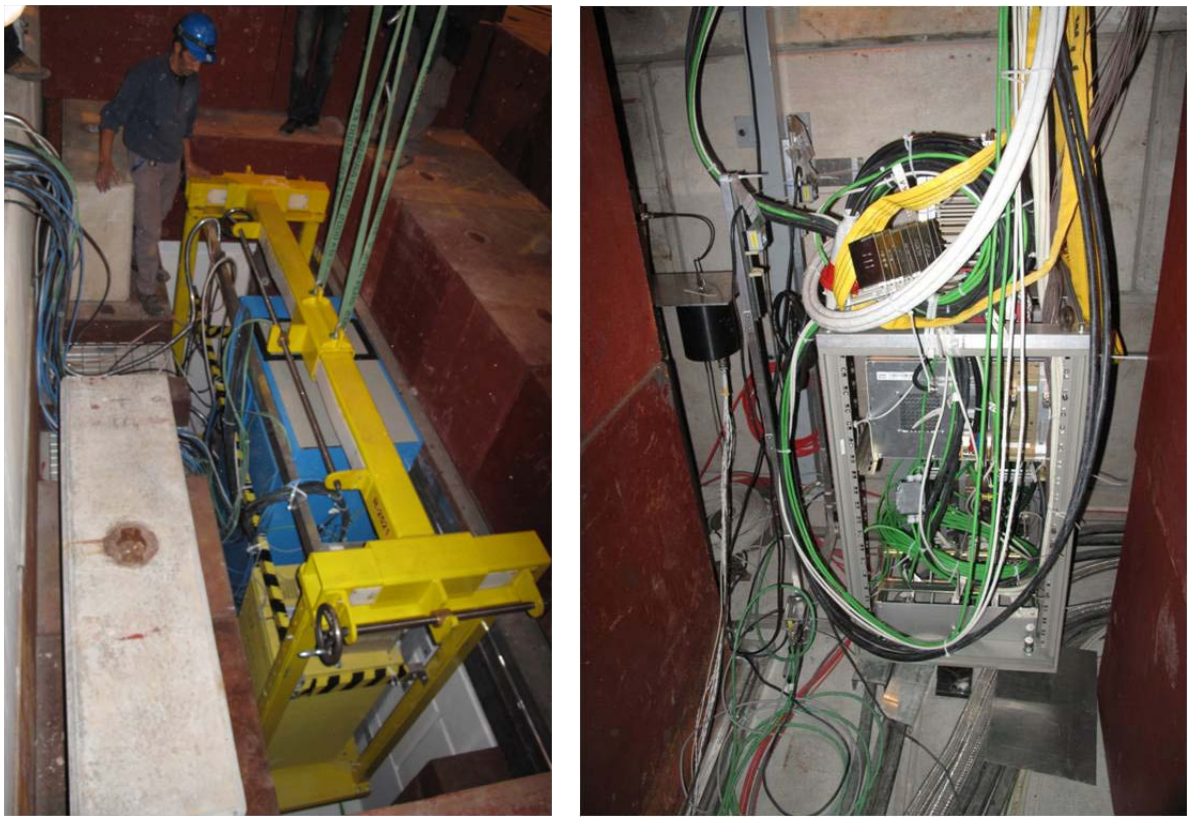

Figure 53: The platform with power converters lowered to the external zone (left) and the internal zone platform with tested equipment [53].

As an example of the simulation output there are presented results for equipment tests during the first and second 2011 irradiation slots, when the area was not fully occupied. The equipment positions are depicted in Figure 54 and Appendix C and the respective simulation results with statistical uncertainties are given in Table 13. Appendix D then brings the equipment positions during the third 2011 irradiation slot.

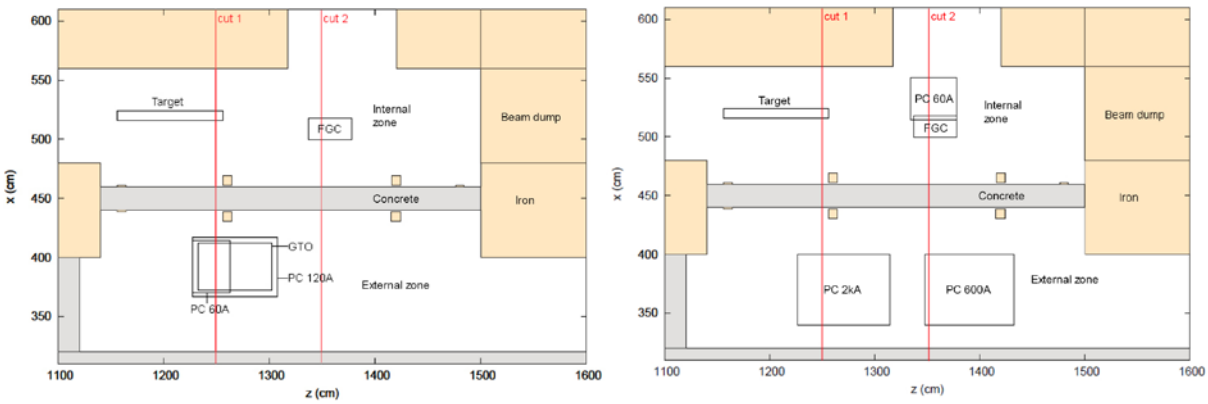

Figure 54: Top view of equipment position during the 1st (left) and 2nd (right) 2011 irradiation periods. The vertical positions (2x2 cut views) are shown in the Appendix C [48].

The importance of the radiation field gradient over the tested equipment volume was discussed already in the section 5.1.2. As a complementary information to Table 13, Table 14

gives a simulated variations of Φ_{HEH} ($\Delta\Phi_{HEH}$) as a relative variation of minimal (-) and maximal (+) fluence from the average Φ_{HEH} in all three dimensions. Taking into account the equipment dimensions, this analysis indicates that the strongest gradient should be expected in the internal zone especially along the vertical y-axis (e.g. function generator controller FGC) and in the external zone along the horizontal x-axis (e.g. power converter PC600A). The high gradient in vertical axis for the external power converter PC2kA is caused by its height of 124 cm. For this device the gradient in x-axis was verified by RadMon measurements performed by RadMon1 and RadMon5 which were mounted on the front and back side, respectively. The discrepancy between the measurement and FLUKA simulation was discussed already in section 5.3.1. Although in this case only the measured N_{SEU} is available, it is obvious that the real Φ_{HEH} gradient over the equipment volume will be higher than the simulated one due to attenuation in the equipment material which is not included in the simulations.

The summary of all tested equipment during both operation years, 2011 and 2012, is given in Appendix E. Several examples of these tests with their feedback are described in the following sections.

Table 13: Simulated dose (in air), HEH fluence, thermal neutron fluence and Si 1 MeV neutron equivalent fluence for equipment positions during the 1st and 2nd 2011 irradiation slots with statistical uncertainties. FGC – function generator controller, GTO – gate turn-off thyristor, PC – power converter. For equipment positions see Figure 54 [48].

	1st 2011 irradiation slot			
Equipment/zone	FGC int	GTO ext	PC60A ext	PC120A ext
Dose (10^{-13}.Gy/p.o.t.)	8.63±0.4%	1.05±1.5%	2.17±1.1%	2.43±0.7%
Φ_{HEH} (10^{-3}/cm^2/p.o.t.)	1.49±0.2%	0.30±0.5%	0.63±0.2%	0.70±0.3%
Φ_{thn} (10^{-3}/cm^2/p.o.t.)	3.21±0.1%	2.81±0.2%	3.15±0.2%	3.05±0.1%
Φ_{neq} (10^{-3}/cm^2/p.o.t.)	7.71±0.1%	1.44±0.2%	2.69±0.2%	2.80±0.2%
	2nd 2011 irradiation slot			
Equipment/zone	FGC int	PC2kA ext	PC60A int	PC600A ext
Dose (10^{-13}.Gy/p.o.t.)	as in 1st slot	1.78±0.3%	11.7±0.4%	1.89±0.7%
Φ_{HEH} (10^{-3}/cm^2/p.o.t.)		0.48±0.2%	2.12±0.2%	0.47±0.3%
Φ_{thn} (10^{-3}/cm^2/p.o.t.)		2.93±0.1%	2.72±0.2%	2.32±0.1%
Φ_{neq} (10^{-3}/cm^2/p.o.t.)		2.18±0.1%	8.54±0.1%	1.63±0.2%

Table 14: Simulated Φ_{HEH} gradient inside the equipment tested during the 1st and 2nd 2011 irradiation slots as a relative variation from average Φ_{HEH} (in Table 13). For equipment positions see Figure 54 [48].

	1st 2011 irradiation slot			
Equipment/zone	FGC int	GTO ext	PC60A ext	PC120A ext
$\Delta\Phi_{HEH}$ in x (%)	+7 -0	+4 -9	+29 -13	+27 -22
$\Delta\Phi_{HEH}$ in y (%)	+36 -17	+4 -9	+14 -2	+11 -12
$\Delta\Phi_{HEH}$ in z (%)	+15 -3	+10 -0	+11 -5	+6 -7
	2nd 2011 irradiation slot			
Equipment/zone	FGC int	PC2kA ext	PC60A int	PC600A ext
$\Delta\Phi_{HEH}$ in x (%)	as in 1st slot	+32 -0	+1 -8	+27 -20
$\Delta\Phi_{HEH}$ in y (%)		+23 -32	+3 -15	+2 -0
$\Delta\Phi_{HEH}$ in z (%)		+4 -8	+18 -18	+9 -4

5.4.1 Power Converter Radiation Tests

One of the most important tested equipment are power converters (PC). In the LHC there are approximately 1700 of them and some of them were never tested before for radiation tolerance. The reason is that the H4IRRAD, apart from other advantages, is the only available test area which can provide for example water for cooling of the PCs such as LHC600A-10V or LHC4-6-8kA-8V. During the first two irradiation slots of 2011, four full-size PCs (with some components installed in the H4IRRAD/CERF cage) were tested. No dose (TID) effect was observed during tests for any PC. While the LHC60A-08V and LHC4-6-8kA-08V PCs showed very low SEE sensitivity (for both PCs only one event observed during tests), the LHC120A-10V underwent five events (always on the same card). This failure level was not critical for 2011 and 2012 LHC operation, but would become a limiting factor for a nominal operation after LS1 (long shutdown of CERN accelerator chain). Thus this PC underwent a partial redesign. LHC600A-10V was tested without its AC-DC internal module, which was replaced by a radiation tolerant external AC-DC module, since known to be highly sensitive. Under these conditions no event was recorded [62, 63].

FGC (Function Generator Controller), tested during first two 2011 slots in the internal zone, is used with all aforementioned PCs except the LHC60A-08V (which uses another type of internal FGC). It suffered several crashes during tests and its failure cross section was estimated to be $2 \cdot 10^{-10}$ $HEH^{-1} \cdot cm^{-2}$ for LHC tunnel areas which makes FGC the second most problematic PC's componnent (after LHC600A-10V's AC-DC). Since the radiation test evaluation, several software improvements of ADC filter have been done which should

partially prevent from crashes. As a next step, the replacement of approximately 1050 FGCs by FGClite devices (rad-tolerant, less complicated architecture) is sheduled [63].

5.4.2 Non-PC Equipment Tests

GTO (gate turn-off thyristor) rad-tolerance is of crucial importance for reliable operation of the beam abort system for LHC security. A GTO failure can provoke an asynchronous dump with associated beam loses and machine down time necessary for generator replacement and system re-calibration (~1 day). The tests of two GTO families, Dynex and ABB, revealed significant difference in SEB (Single Event Burnout) sensitivity. Dynex is approximately 10 times more sensitive, therefore only ABB GTOs will be used in LHC as much radiation harder and more reliable.

LHC cryogenics Schneider PLC system was tested to clarify if the LHC downtime due to unexpected PLC crashes was caused by radiation. Tests showed a high SEU (Single Event Upset) sensitivity ($2 \cdot 10^6$ HEH/cm^2/failure) of PLCs, therefore their partial relocation was performed during 2011/2012 winter shutdown and full relocation was projected.

Failures were observed neither on TITAN 400VAC Circuit Breakers (2 of previous generation and 3 of new generation) nor on Ackerman 48VDC Battery Charger, which provide an auxiliary source for a lot of equipment (e.g. Command Circuits, interlocks, Exit Lighting system etc.).

Schneider Premium & Twido PLCs are used on surface. The aim of the tests was to verify if they could be used in underground areas. Several problems occurred during irradiation and SEU induced failure cross section was estimated to be $1 \cdot 10^7$ HEH/cm^2/failure [63].

ST SPLargeUHD SRAMs (4 Mbit) manufactured by STMicroelectronics were tested observing no permanent radiation damage. The SEU cross section for three test runs has been evaluated to be $6.9 \cdot 10^{-14}$, $6.0 \cdot 10^{-14}$ and $6.1 \cdot 10^{-14}$ cm^2/HEH/bit and the MBU (Multiple Bit Upset) cross section was calculated to be $7.7 \cdot 10^{-17}$, $1.5 \cdot 10^{-15}$ and $1.6 \cdot 10^{-15}$ cm^2/HEH/bit [64].

The 1-wire Dallas Communication components (DS2401 and DS18B20) were tested as candidates for the FGClite project (see section 5.4.1) use. No permanent damages have been observed. Nevertheless several problems with thermometer DS18B20 were detected. The observed SEE cross section for the thermometer communication is

$5.1 \cdot 10^{-10}$ cm^2/HEH/component and for the temperature reading it is $9.2 \cdot 10^{-11}$ cm^2/HEH/component [65].

Another candidate considered for the FGClite project is the Texas Instrument High-Resolution Analog-to-Digital Converter (ADC) ADS1218. No permanent damages have been observed. No glitches have been detected by a dedicated software which scanned output files with filtered values from the modulator output of the ADS1218 [66].

MAXIM 16-bit digital-to-analog converter (DAC) MAX5541 is also a component which could be used for the FGClite project if sufficiently radiation hard. Three units were tested up to 135, 123 and 118 Gy with neither SEE, nor any significant power consumption increase during or after irradiation observed [67].

5.4.3 Detector Tests

The European Space Agency's (ESA) SEU Standard Monitor, which is e.g. part of the Technology Demonstration Module on-board the PROBA-II satellite, was tested in H4IRRAD where the hadron spectra reach much higher energies than in standard facilities (in which this device was tested before). It is a 16 Mbit SRAM Multi-Chip Module consisting of four Atmel 4 Mbit memories. The ESA Monitor measurements were compared with FLUKA simulations and with RadMon (which has a similar SEU cross section) measurements with a good agreement. For more details see [68].

Thermoluminescent detectors (TLD) are used for dose measurement covering a wide range of 0.1 Gy to few kGy. Several different types of TLDs were tested in H4IRRAD during most of irradiation slots (therefore not listed in Appendix E). These detectors are based on LiF using various dopes which influence detection sensitivity to the field components (e.g. to heavy charged particles). Different isotopic ratio between ^{6}Li and ^{7}Li influences sensitivity to thermal neutrons. The aim of the tests was to study the TLD response to complex radiation fields and to determine calibration factors for evaluation of HEH and thermal neutron fluence from measured dose. These factors were applied to estimate the HEH and thermal neutron fluence in LHC. The results showed an agreement within a factor of two compared to the RadMon measurements and FLUKA simulations [69, 70].

5.5 Summary

This chapter dealt with the design, optimization, construction and operation of the H4IRRAD irradiation area used for LHC electronics radiation tests. In the scope of the doctoral work the author performed all the Monte Carlo design and optimization studies, participated in the area installation, commissioning and operation as well as the detector benchmarks and equipment tests. The optimization of the area comprised of two main tasks. The first one was to optimize the geometry of the test zones to be representative of the LHC tunnel and shielded locations. This was achieved by dividing the test area to the internal and external zone by a shielding and by optimizing of this shielding material and thickness. The other task was to assure the radiation safety outside the shielding. Based on the author's simulations, the existing concrete shielding was partially replaced by iron blocks and prolonged and several existing cable passages had to be shielded. The calculated radiation above the roof resulted in blocking the access to the roof during operation. The instrumentation, equipment and air activation was simulated as well in order to define access conditions and equipment handling after the irradiation period. During the area commissioning in June 2011 the author participated mainly in the proton beam setup involving also simulations of the whole H4 beam line and it's comparison with the measured beam profiles at several positions. During the 2011 and 2012 area operation the author was again responsible for all the Monte Carlo studies. This involved programming of a special beam source routine reproducing the measured non-Gaussian beam profile to be used as the simulation input, upgrading the FLUKA model and characterizing the radiation environment inside the whole area. Detailed simulations at several detector positions allowed a direct comparison of the Monte Carlo prediction with the measurement and the simulated values could be tuned to better represent reality. The author participated in the installation of tested equipment and the radiation detectors including the measured data analysis. During six irradiation periods in two years over fifty devices/components were tested. For all of them the author provided the simulated and corrected dose, HEH fluence, thermal neutron fluence, Si 1 MeV neutron equivalent fluence and on request also particle spectra. This allowed to the users to obtain the failure cross section and for the LHC equipment to decide on a potential equipment replacement, relocation or additional shielding.

6. Medipix Tests

This chapter deals with the measurements performed by Medipix/Timepix (MPX/TPX) detectors in H4IRRAD. These devices, used e.g. in ATLAS detector, are well calibrated for radiation fields only up to around 30 MeV. The aim of these tests is to study the MPX/TPX behaviour in a well characterized high energy mixed particle environment which is provided by H4IRRAD.

6.1 Medipix Detector

Medipix2 [71], a hybrid silicon pixel detector, was developed at CERN by the Medipix2 Collaboration [72]. It can be efficiently used for real-time measurements of the complex radiation field composition by distinguishing of particle groups based on the recognition of tracks generated by ionizing radiation in the chip. The device consists of a ~2 cm^2, 300 µm thick silicon sensor matrix of 256 × 256 elements, each with an area of 55 µm × 55 µm, bump-bonded to a readout chip. Each of the 65536 cells is connected to its readout chain integrated on the chip. When an incoming particle hits the silicon sensor, it deposits energy creating free charge carriers. If the generated signal exceeds the set threshold, the pixel is activated. Depending on the physics of the interaction and on the process of charge collection, a single particle can activate one or several pixels forming a cluster. An example of different cluster shapes recorded during operation of H4IRRAD area is shown in Figure 55, right [71, 73].

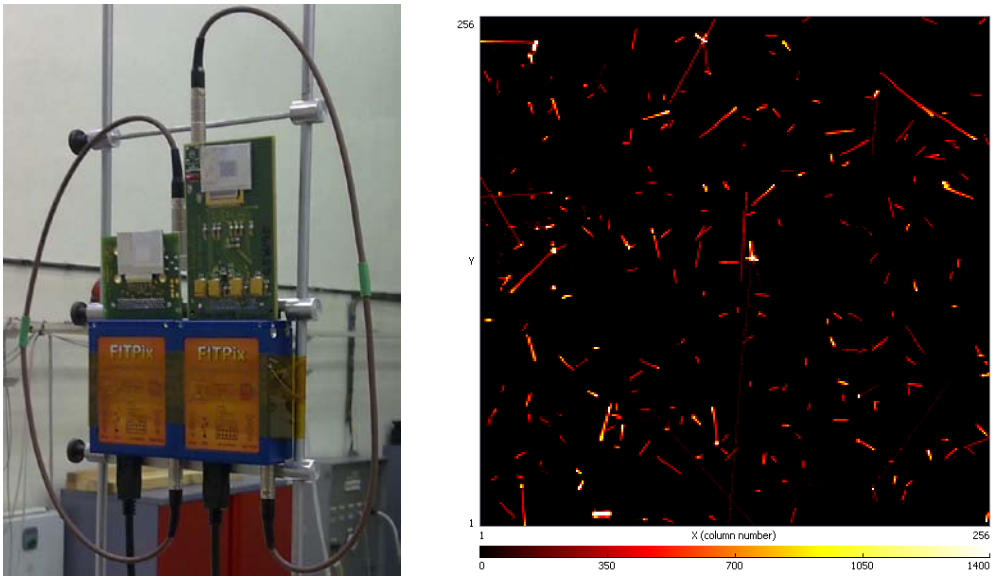

Figure 55: The TPX and MPX detector with FITPix interface for data readout and acquisition control (left) and radiation field in H4IRRAD measured by TPX detector with an exposure time of 0.1 s (right).

To measure neutron fields, the MPX detector is divided into several regions by a mask of converter materials covering its surface. The mask structure is visible in Figure 56. The ^{6}LiF layer (1) under aluminium foil is used for detection of thermal neutrons through the $^{6}Li(n,\alpha)^{3}H$ reaction. Fast neutrons are detected either directly through their nuclear interaction in silicon or with a better efficiency (especially in MeV range) under the polyethylene (PE) layer (2) through recoil protons. The aluminium support above the polyethylene serves as an energy threshold and under this region (3) only neutrons with energies above 3.5 MeV are detectable. The aluminium foil (4) acts as an attenuator of low energy muons, electrons and X-rays (since recoil protons from neutrons with lower energy than 3.5 MeV are stopped). These are additionally attenuated in the region 5. The uncovered area (6) is exposed to all incoming radiation. The typical internal detection efficiencies are approximately 100 % for charged particles with energies above 8 keV, 90 % for 10 keV X-rays, 2 % for 60 keV X-rays, 0.5 % for 662 keV γ-rays and 0.1 % for γ-rays with energy above 1 MeV. Slow neutrons with energy below 1 eV are detected under the ^{6}LiF converter typically with the efficiency of 1% and neutrons with energies 1-15 MeV with 0.1% efficiency below the PE converter. The detection efficiency for minimum ionizing particles (MIPs) is 100 %, but their recognition depends on the incidence angle. More details on the converters, detection efficiency and its measurement are given in [73].

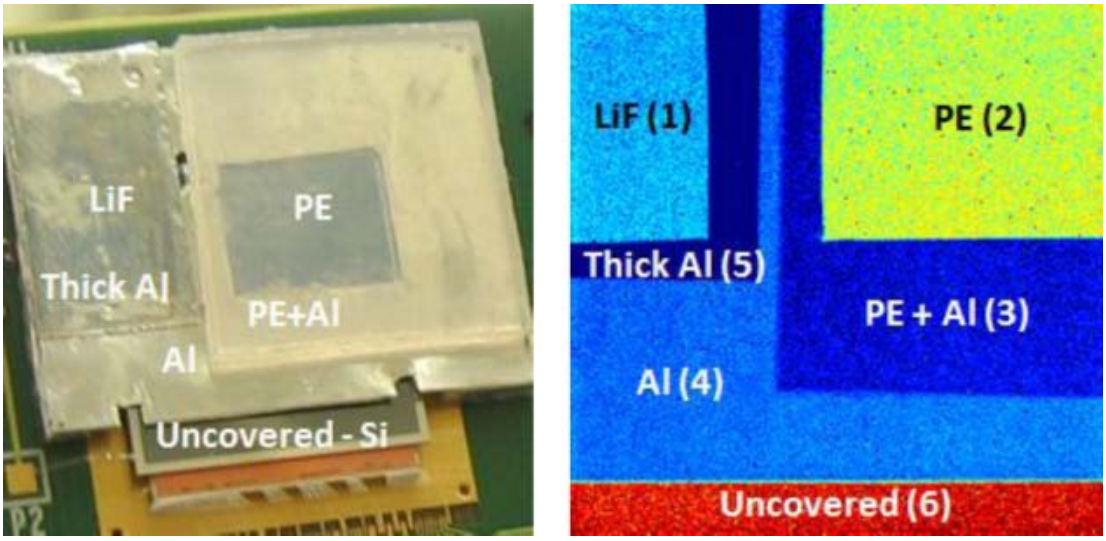

Figure 56: The MPX detector covered with conversion layers (left) and its X-ray radiogram (right) [73].

The detector can be operated either in pixel-hits counting mode or cluster-tracking mode. The counting mode is based on frame analysis by summing all hits registered in pixels (summed for each region and the full detector) and is used in radiation environment with high particle fluxes. The tracking mode is based on the analysis of the shapes of individual

clusters. The clusters are analyzed by pattern recognition algorithm using their characteristics like area, roundness, linearity and width of the track. The analysed clusters are sorted into six categories corresponding to the types of interacting particles as visualised in Figure 57:

1) Dot – low energy X-rays and electrons;
2) Small blob – more energetic photons and electrons;
3) Curly track – energetic photons and electrons (MeV range);
4) Heavy blob – energetic particles with low range (alpha particles);
5) Heavy track – energetic charged heavy particles;
6) Straight track – energetic charged light particles (protons, muons...) [73, 74].

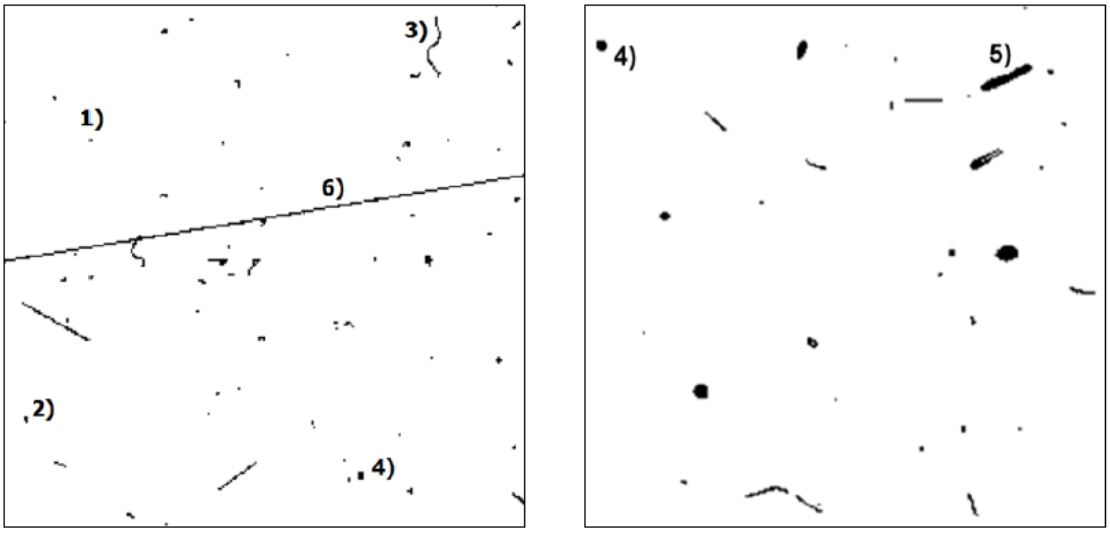

Figure 57: Examples of cluster categories as described in the text. Frames are from MPX measurement performed in the Atlas cavern (left) and in a cyclotron beam (right) [73].

The Timepix (TPX) chip is an evolution from the Medipix2 chip developed at CERN by Medipix collaboration. The main difference is that the TPX chip uses an external reference clock to generate the clock in each pixel that increments the counter depending on the selected operation mode. Each pixel can be configured in one of three different modes: Medipix mode (counter counts incoming particles), Timepix mode (counter works as a timer and measures time of the particle detection) and Time over threshold (TOT) mode (counter is used as Wilkinson type ADC allowing direct energy measurement in each pixel) [75].

For the studies described in this chapter two detection modules were used: one MPX detector (G05 with FITPix interface W0045) and one TPX detector (E07 with FITPix W0097). The units were operated using Pixelman [76] software package for Medipix2 acquisition control with Java graphical user interface and its plugins.

6.2 Medipix Calibration

Since each of the 65536 independent channels has slightly different response it is crucial to perform an energy calibration of each pixel. In addition the efficiency of neutron detection depends significantly on the neutron convertor mask properties and positioning above the sensitive area. Therefore the efficiency calibration must be performed for each device using known neutron sources. The two abovementioned detectors were calibrated in September 2012 during author's visit in Prague.

6.2.1 Energy Calibration

The energy calibration was performed in the Institute of Experimental and Applied Physics (IEAP), Czech Technical University in Prague [77]. This phase was conducted without the converter layer. The first step is threshold equalization used to compensate the pixel to pixel threshold variations. The procedure, automated and fully integrated in Pixelman plugin, finds distribution for each of the 16 adjustment values and for each pixel selects such adjustment to make its threshold as near as possible to the average of the threshold distribution mean values as described in [78]. This procedure also masks pixels which give value too far from the mean threshold (e.g. 260 pixels for our TPX chip as visible in Figure 58, this corresponds to one defective column and four other pixels).

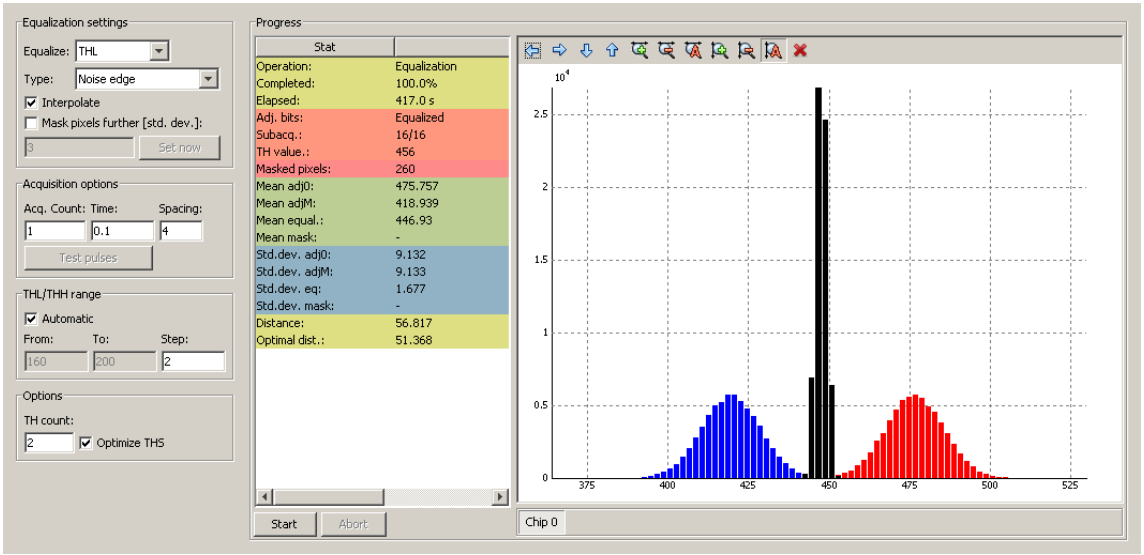

Figure 58: Threshold equalization result for TPX E07- W0097.

The energy calibration translates the ADC threshold units of the MPX/TPX device to its corresponding energy. The detectors, placed in a light shielded box, were uniformly exposed to two radioactive sources (also inside the box): ^{55}Fe producing X-rays of 5.8 keV and ^{241}Am producing gamma photons of 13.9 keV and 59.5 keV. The threshold scan was

performed during irradiation by both sources and from the Gaussian fits of the peaks in the scans the calibration curve was calculated and saved. More information about the energy calibration can be found in [78] and [79].

After the energy calibration of the detectors the converter layer was attached to the detectors and by the X-ray radiography the exact geometry was recorded (visible from Figure 56, right).

6.2.2 Neutron Detection Efficiency Calibration

The neutron detection efficiency calibration was performed in the Czech Metrology Institute (CMI) [80] with a set of known neutron sources. The threshold was set high enough to filter tracks induced by light particles in silicon and the acquisition time was set such that approximately 100 events per time frame were registered.

Thermal neutron efficiency was measured in an isotropic field of neutrons from ^{238}PuBe source moderated in a graphite prism (setup in Figure 59, left). The fluence in the detector position was $3.2 \cdot 10^4$ (±5 %) $n_{th} \cdot cm^{-2} \cdot s^{-1}$.

For the fast neutron efficiency measurements a setup using a rod with a neutron source tip pointing to the detectors (photo in Figure 59, right) was used. Measurements with two sources were performed: one with ^{252}Cf (spontaneous fission spectrum with an average energy of 2.1 MeV and an emission of $1.082 \cdot 10^8$ (±0.7 %) $n \cdot s^{-1}$) and the other one using ^{241}AmBe (spectrum with an average energy of 4.5 MeV and an emission of $2.159 \cdot 10^7$ (±0.7 %) $n \cdot s^{-1}$).

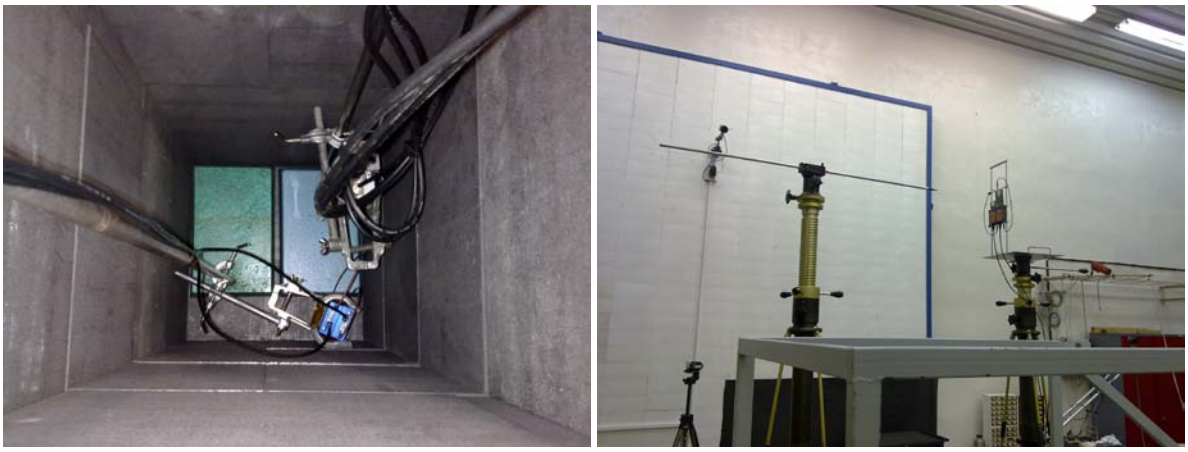

Figure 59: Calibration set-ups in CMI: A graphite prism with thermal neutron field (left) and a rod with a fast neutron source tip (right).

The neutron detection efficiencies can be then calculated using the following equation:

$$\varepsilon_{A-Si} = \frac{\frac{N_A}{S_A} - \frac{N_{Si}}{S_{Si}}}{\Phi \cdot t}, \tag{6}$$

where N_A and N_{Si} are numbers of clusters detected during the given measurement in a region A (i.e. ^{6}LiF region for thermal neutrons and PE region for fast neutron measurement) and in the uncovered region (Si); S_A and S_{Si} are the areas corresponding to these regions; Φ is the incident neutron flux and t is the time of measurement [73]. Here the clusters detected in the uncovered region are subtracted to count only the reactions caused by the conversion layer. For the efficiency evaluation see section 6.4.1.

6.3 Medipix Measurement in H4IRRAD

The MPX/TPX tests in H4IRRAD area were performed during the third irradiation period of 2012 (15th November – 3rd December). Due to a high dose inside the irradiation zones and access restrictions during tests, the detectors were installed behind the 3.2 m long iron beam dump as visible from Figure 60. The access to the MPX/TPX position was possible through the tunnel from the downstream safety door PPE124 directly after beam stop without any restrictions.

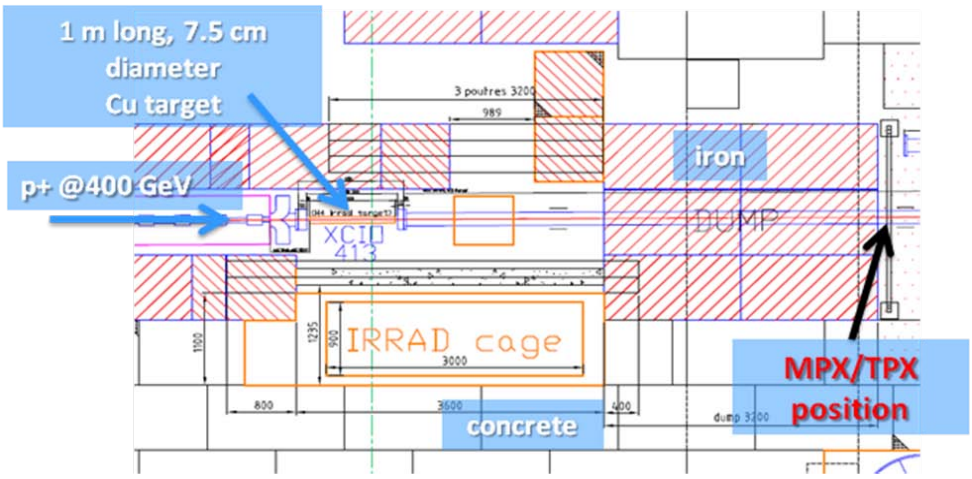

Figure 60: Layout technical drawing of the H4IRRAD irradiation area with marked MPX/TPX detector position downstream the iron beam dump [81].

An aluminium support, visible in Figure 61, was constructed to allow the MPX and TPX sensors to be positioned exactly at the beam line height. Horizontal position for the main measurement was set such that the beam line was exactly in the middle of two sensors.

During this irradiation period an attenuated primary proton beam of 400 GeV/c from SPS (supercycle of 44 s) with nominal intensity up to ~3·10^9 p+/spill was used. In order to

perform specific radiation tests on sensitive electronic equipment, the area operated at low intensity during the first part of the irradiation slot (15th to 21st November). Due to a very unstable beam conditions and low statistics the data from this time interval could not be used for analysis. The main measurement with both detectors facing upstream (front side irradiation, i.e. the conversion layer facing the beam dump; the beam line axis between the detectors) was performed during a first half of the high (nominal) intensity operation (22nd November to 27th November afternoon) with delivered $1.56 \cdot 10^{13}$ (±5 %) p.o.t. During the rest of the area operation (27th November afternoon to 3rd December) several different positions were set up to test detector response (back side irradiation and irradiation under 84°) and to confirm the measured beam line position (lateral shifts).

Figure 61: A detail of the aluminium support/holder with attached MPX and TPX detectors (left) and its position during measurements behind the beam dump (right).

Figure 62 shows the simulated neutron, proton, pion, kaon and muon spectra at the TPX position for the front side irradiation. The energies behind the iron beam dump still reach several tens of GeV (neutron energies go up to 20 GeV). The high energy part of spectrum is dominated by muons which reach up to ~300 GeV.

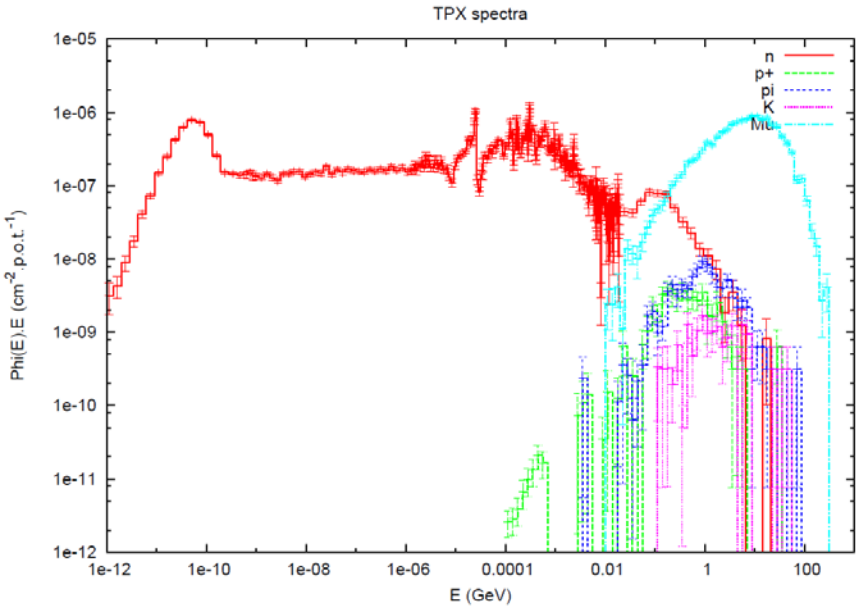

Figure 62: Simulated particle spectra per proton on target at the TPX detector position during the front side irradiation [81].

6.4 Medipix Data Analysis

Due to the TPX information about the measured particle energy, the analysis of TPX data is much more precise than for MPX data. Therefore only the TPX data analysis will be described in this chapter (the MPX data have been used only for a rough verification of the results). The analysis focused mainly in determination of thermal neutron fluence at the detector position and in its comparison with the corresponding FLUKA simulations.

6.4.1 Thermal Neutron Fluence Analysis

For the thermal neutron fluence analysis the data measured below the ^{6}LiF convertor were used. As a first step, the background (signal from the rest of the detector) must be minimized. This can be done by searching for the best cluster criteria using e.g. pattern recognition Pixelman plugin [76]. The best separation of the TPX signal below LiF was obtained for the following (energy and shape dependent) criteria:

- Min. cluster size: 8
- Cluster volume: 2000-2850 keV
- Cluster height: 600-1000 keV
- Min. cluster roundness: 0.9

The same criteria were applied on the data recorded in CMI during thermal neutron calibration (see chapter 6.2.2) and the analysis was performed on the resulting data sets. In the

image of the filtered data from both H4IRRAD and CMI measurements, displayed in Figure 63, the LiF area is well visible. For the 3088 s long CMI measurement, the average cluster count under the LiF convertor is 8.3 ±0.5 % (after background subtraction), i.e. $2.7 \cdot 10^{-3}$ (±0.5 %) s^{-1}. By dividing this value by the fluence in the detector position, which is $3.2 \cdot 10^{4}$ (±5 %) $n_{th} \cdot cm^{-2} \cdot s^{-1}$, we obtain a factor of $8.4 \cdot 10^{-8}$ (±5 %) $n_{th}^{-1} \cdot cm^{2}$. The thermal neutron detection efficiency of 0.28 %, calculated from equation (6), is lower than 1 % (mentioned in section 6.1) due to the strict cluster criteria.

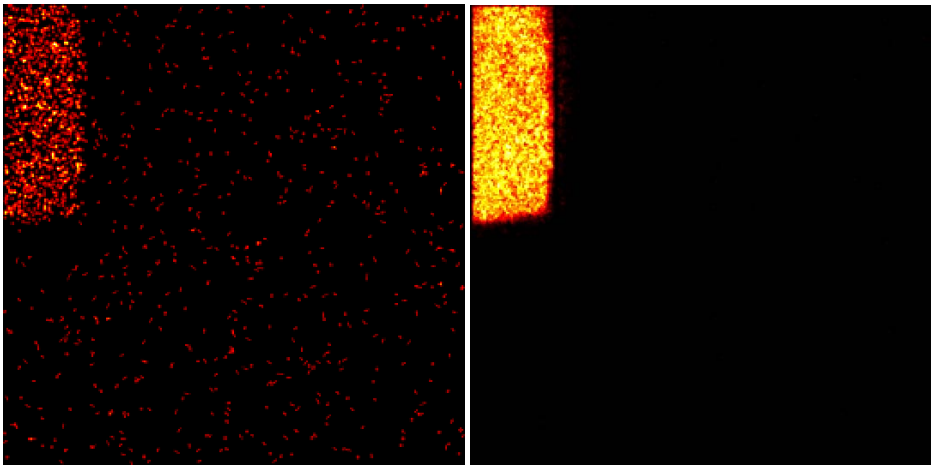

Figure 63: Images of integrated response of the TPX device after application of thermal neutron filter cluster criteria for the measurement in H4IRRAD (left) and CMI (right) [81].

For the H4IRRAD measurement (with $1.56 \cdot 10^{13}$ p.o.t.) the average cluster count (without background) under the LiF layer is 0.22 ±3 %. Using the factor calculated from the calibration data, we obtained the thermal neutron fluence in H4IRRAD of $2.6 \cdot 10^{6}$ (±6 %) $n_{th} \cdot cm^{-2}$. Since the detector operated with different (factor of ten) acquisition times in CMI and H4IRRAD, also the dead time was different for both measurements. After applying a dead-time correction [73], the fluence of $1.04 \cdot 10^{7}$ (±6 %) $n_{th} \cdot cm^{-2}$ was obtained.

As described in section 6.1, thermal neutrons are detected through $^{6}Li(n,\alpha)^{3}H$ reaction. Although the cross section of this reaction is very high for thermal neutrons, it is not negligible for higher energies (see Figure 64 for $^{6}Li(n,\alpha)^{3}H$ interaction cross section). This leads to an overestimation of measured thermal neutron fluence (caused by registered epithermal and fast neutrons) which needs to be corrected using resonance integrals:

$$I = c \sum_{i} N_i \times \sigma_i \,, \tag{7}$$

where c is normalization constant, N_i is number of neutrons in *i-th* energy bin of neutron spectral distribution (used simulated spectra, see Figure 62) and σ_i is cross section of interaction $^{6}Li(n,\alpha)^{3}H$ (presented in Figure 64) corresponding to the neutron energy of *i-th* bin. Two resonance integrals are calculated: I_{th} for thermal neutrons (0 – 0.532 eV corresponding to the FLUKA energy group #239 as defined in the simulations) and I_0 (0 eV – infinity) for all neutrons. The ratio $I_{th}/I_0 \leq 1$ is used as a correction factor for measured thermal neutron fluence [73].

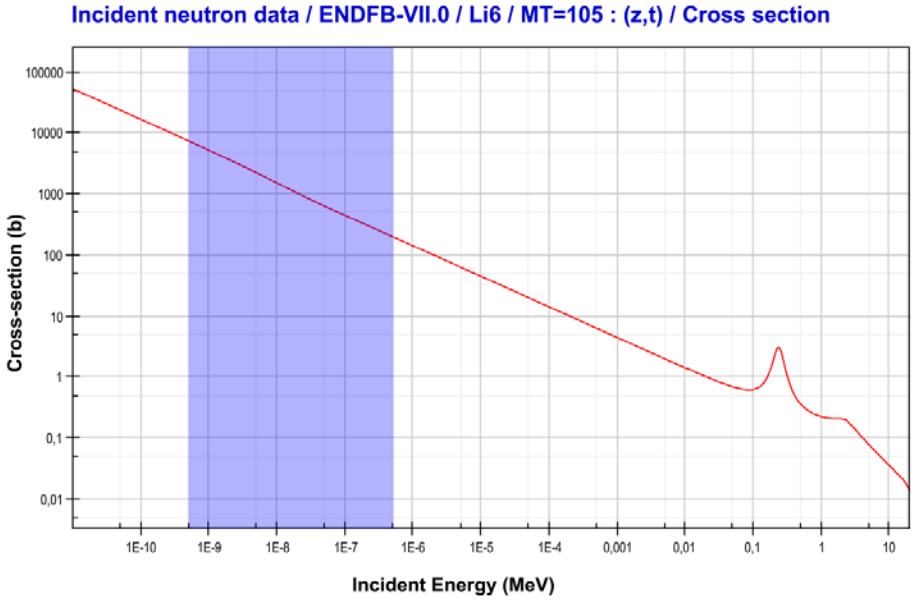

Figure 64: Cross-section for (n,α) interaction on ^{6}Li. Energy region of thermal neutrons (E < 0.5 eV) is highlighted by blue colour [73].

For the measurement in the H4IRRAD the resonance integral ratio $I_{th}/I_0 = 0.95$ (i.e. the correction for epithermal and fast neutrons is approximately 5 %). By multiplying the uncorrected measured fluence with this ratio we obtain a thermal neutron fluence of $9.9 \cdot 10^{6}$ (±6 %) $n_{th} \cdot cm^{-2}$. The respective fluence calculated by the FLUKA Monte Carlo simulation is $2.6 \cdot 10^{7}$ (±5 %) $n_{th} \cdot cm^{-2}$. Comparison of the simulated and measured results shows that the simulation overestimates the thermal neutron fluence by a factor of $\Phi_{sim}/\Phi_{meas} = 2.6$ (±8 %). This ratio is consistent with the comparison between simulation and RadMon measurement presented in section 5.3.1. Potential causes of this disagreement will be discussed in the following section.

6.4.2 Shielding influence on thermal neutron fluence

Comparison of simulated and measured (RadMon, MPX) thermal neutron fluence shows a significant disagreement (see section 5.3.1 and 6.4.1). One of the main potential sources of this discrepancy is the shielding properties. Since the concrete and iron shielding composition is not known (the shielding blocks have various age and origin), a "standard" composition and density is commonly used within CERN for the radiation Monte Carlo studies.

A standard cast iron used in the simulations contains 95 % (mass) of iron and 5 % of carbon and has a density of 7.2 g·cm^{-3} (using a special card for thermal neutron cross sections in iron). As a standard concrete, a Portland concrete predefined in the Flair tool with a composition listed in Table 15 and with a density of 2.3 g·cm^{-3} was used. A simplified geometry of H4IRRAD (see Figure 65) was modelled for the purpose of studies of different shielding material compositions. This simplification allowed to run many different scenarios with reasonable statistics.

Table 15: Portland concrete composition as used in the original FLUKA simulation.

Element	H	C	O	Na	Mg	Al	Si	K	Ca	Fe
Mass %	1	0.1	52.9107	1.6	0.2	3.3872	33.7021	1.3	4.4	1.4

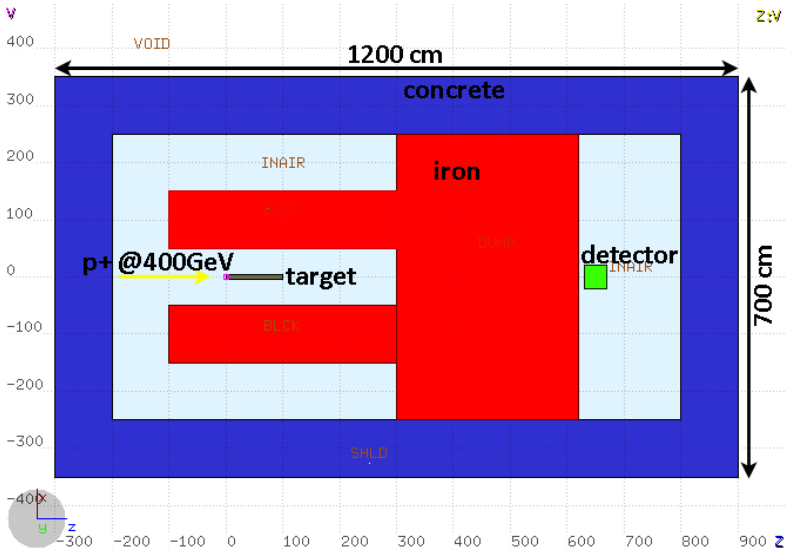

Figure 65: Simplified H4IRRAD FLUKA model (top view) for shielding influence studies. Real shielding and iron beam dump thickness is used.

Since there is 3.2 m of iron between the H4IRRAD target and the TPX detector while the concrete blocks are placed only around the setup (see Figure 60), the first task was to study the influence of iron composition. After several initial simulations there was decided to

analyse iron blocks composition. Four samples from two different iron shielding blocks were extracted by slow drilling and analysed in VUHZ, a.s. laboratory [82] (Czech Republic). The analysis report in Appendix F shows that the content of impurities can differ by up to approximately 30% even within the same (0.8×0.8×1.6) m shielding block (e.g. manganese content in samples 8430-3 and 8430-4 from the same block). The average values listed in Table 16 were implemented to the simulation as the real iron composition (with the iron content of 94.74075 %).

Table 16: Analysed impurities content in the shielding cast iron – average values from the report in Appendix F.

Element	C	S	Si	P	Mn	Cr	Ni
Mass %	2.265	0.1725	1.53	0.7125	0.3675	0.125	0.08675

The simulated thermal neutron fluences in the detector position for the new (real) and the old iron composition were compared resulting in a ratio of $\Phi_{simReal}/\Phi_{simOld}$ = 1.5 (±9 %) increasing the disagreement between simulation and measurement to Φ_{sim}/Φ_{meas} = 3.9 (±12 %).

The density range of standard cast iron can vary approximately from 6.8 g·cm^{-3} to 7.8 g·cm^{-3} (e.g. [83]). The laboratory was not able to measure this quantity, therefore a simulation with the highest possible density was carried out. In case of the iron density of 7.8 g·cm^{-3} instead of 7.2 g·cm^{-3} (used in the original simulation) the ratio between simulation and measurement would significantly decrease to Φ_{sim}/Φ_{meas} = 1.85 (±13 %).

The previous paragraphs demonstrate that the difference in the iron composition does not solve the discrepancy between simulation and measurement. For the studies of the concrete composition influence, the real (measured) iron composition with the density of 7.2 g·cm^{-3} was considered. Since until now the extraction and analysis of the concrete samples (which is more challenging than for the iron case) have not been performed, this chapter will concentrate just to the simulation of potential scenarios.

Several available standard concrete compositions (see e.g. [84, 85]) were implemented into the Monte Carlo model and compared with the original setup without significant differences between the thermal neutron fluence values. Neither studies of different water contents showed variation in thermal neutron fluxes higher than few percent. The only promising solution of simulation overestimation found is a possible content of elements with a high cross section for thermal neutron reactions, namely boron and lithium. The

approximate amount of these two elements needed to achieve a simulation-measurement agreement has been optimized to be 0.1 % of boron or 1 % of lithium (natural abundance). For the boron doped concrete the ratio between simulation and measurement would be Φ_{sim}/Φ_{meas} = 0.96 (±13 %) and for the lithium one Φ_{sim}/Φ_{meas} = 1.07 (±18 %). The thermal neutron peak suppression caused by boron is visible in Figure 66. Different concrete densities have also been studied, but even the extreme values do not have a significant effect on thermal neutron levels.

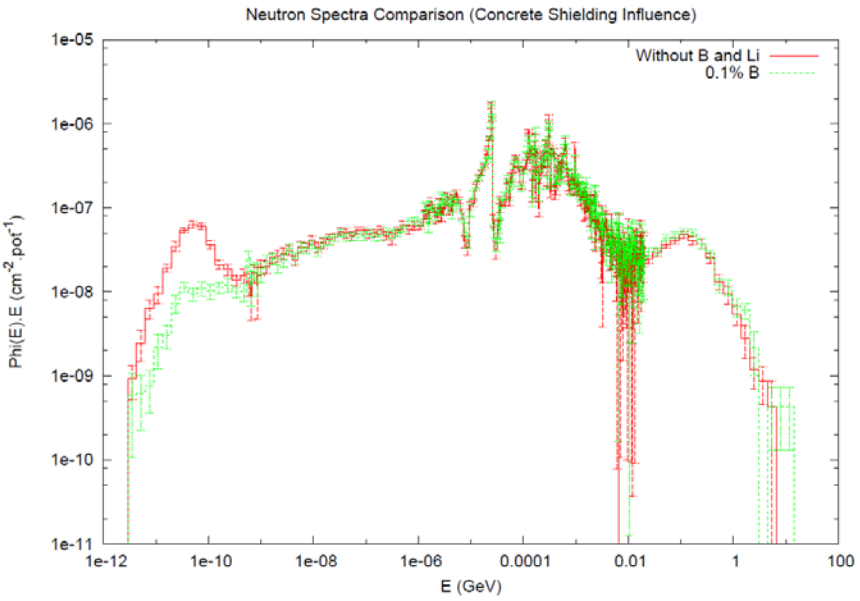

Figure 66: Simulated neutron spectra at the detector position for the simplified geometry – comparison for the standard Portland concrete without and with added boron [81].

After the original assumption about the lead role of iron (due to the area geometry) the strong influence of concrete composition was surprising. This effect can be understood from Figure 67. While the thermal neutrons are strongly suppressed in the iron, their level increases by a factor of almost 3 directly after the beam dump. From the left plot the higher thermal neutron level in the concrete floor and roof is visible.

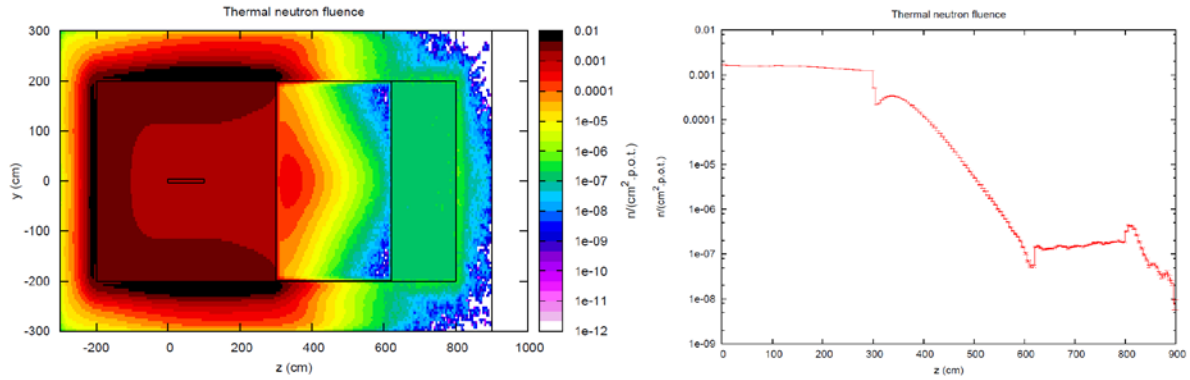

Figure 67: Simulated thermal neutron fluence: 2D vertical cut averaged over ±10 cm vertically around the central plane (left) and a longitudinal profile averaged over ±5 × ±5 cm around the beam line axis (right).

6.4.3 High Energy Particle Fluence Analysis

As described in the section 6.2.2 the calibration was performed also for the "fast" neutrons using ^{252}Cf and ^{241}AmBe source. For this MeV energy range the signal below the area with the polyethylene filter is clearly dominating. In H4IRRAD we encounter energies much higher (for the spectra at the TPX detector position see Figure 62), up to several tens of GeV. For such energetic hadrons the thin polyethylene filter is invisible while they interact directly with the silicon of the sensor. This nuclear interaction has very similar cross section for different hadrons, therefore the detector cannot distinguish between e.g. proton and neutron. For this reason it was not possible to separate the signal below polyethylene layer from the background and to use the calibration data for fast neutron analysis.

The muon fluence was analysed from the data set recorded by the TPX detector positioned under 84° in respect to the beam line by extracting the straight tracks (visible in Figure 68). The resulting measured muon fluence is $2.496 \cdot 10^7$ (±0.005 %) μ·cm^{-2}. The corresponding simulated value is $2.03 \cdot 10^7$ (±7 %) μ·cm^{-2}. Comparison between the simulated and measured results shows that the simulation slightly underestimates the muon fluence by a factor of Φ_{sim}/Φ_{meas} = 0.81 (±7 %).

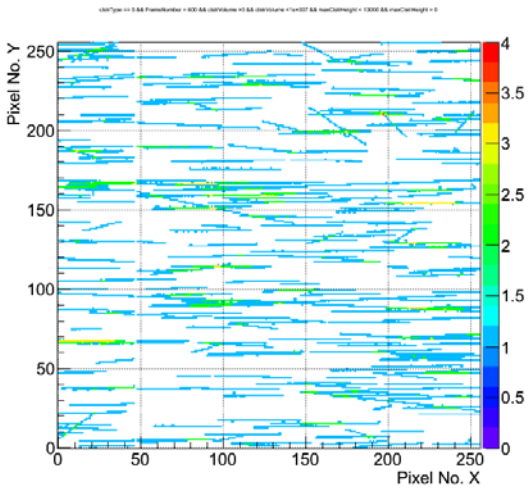

Figure 68: Image of integrated response of the TPX device: "straight tracks" representing muon signal.

6.5 Summary

The topic of this chapter were the tests of the Medipix (MPX) and Timepix (TPX) detectors in the H4IRRAD area which was described in the previous chapter. Before the measurement itself the author participated in the energy and neutron detection efficiency calibration of several MPX/TPX units in Prague. Another important step before the measurement was to identify a suitable test location in H4IRRAD by FLUKA simulations. A position behind the 3.2 m long iron beam dump was chosen for its moderate radiation level and easier access conditions. The author then installed one MPX and one TPX detector at the aforementioned position and carried out several sets of measurements during one H4IRRAD irradiation period of 19 days. He performed a measured data analysis and compared with his Monte Carlo simulations. The simulation overestimated the measured value for thermal neutron fluence by a factor of 2.6, which is consistent with the comparison between the simulation and RadMon measurements presented in the section 5.3.1. Additional studies to better understand this phenomenon were presented. The agreement between measured and simulated muon fluence is within 20 %.

7. Conclusion

This thesis explains the motivation for creating two new irradiation facilities at CERN, GIF++ (a future upgrade of a current Gamma Irradiation Facility for testing LHC detectors) and H4IRRAD (a new mixed-field irradiation area designed for testing LHC electronic equipment). The theoretical background of radiation effects on detectors and electronics is briefly clarified, followed by a few examples of current test facilities used by CERN detector and electronics communities. The overview of the most important software tools used for the studies in the framework of the thesis is given as well. The GIF++ and H4IRRAD facilities together with the specific pixel detector tests are introduced in the last three chapters.

The optimization studies of originally proposed GIF++ facility were completed in 2010. After the approval of the facility in 2012 and the design upgrade, the final optimization has been performed using FLUKA Monte Carlo code. After all modifications, the simulation confirmed that operation of the GIF++ facility is compliant with the dose rate limits which are applicable in a supervised radiation area. GIF++ construction has been finalized in August 2014 and has been operating since March 2015.

The design and optimization Monte Carlo studies of H4IRRAD area were completed in 2011. These studies lead to the successful construction of the H4IRRAD area and its commissioning in June 2011. The radiation field and spectra were evaluated for the purpose of electronic equipment tests and Radiation Protection (RP) issues during 2011 and 2012 area operation, as well as for the comparison between FLUKA simulation results and measurements performed by several types of detectors. The comparison showed a good agreement for high energy hadron fluence and for dose (in both cases disagreement within 30%), while the simulated thermal neutron fluence is overestimated by a factor of 2.5 to 3. These benchmark test results have been used for a correction of simulated radiation field in the test equipment locations. The radiation tests of several types of power converters and extensive number of other electronic equipment gave a valuable feedback to R2E task force and the area proved its crucial role in minimizing the radiation induced failure rate in LHC and its future upgrades.

As a last part of activities within the frame of PhD studies, a measurement by Medipix/Timepix (MPX/TPX) detectors was carried out in H4IRRAD in November 2012. The measured data were analysed and compared with simulation. Analogously to the

aforementioned comparison, also in this case the simulation overestimates thermal neutron fluence by a factor of 2.6. Therefore, an investigation of this discrepancy has been conducted. The most probable reason was assumed to be unknown composition and density of shielding materials. While the iron analysis has not solved this problem, potential content of boron or lithium in the concrete would suppress significantly the thermal neutron level. Assuming 0.1 % of boron or 1 % of lithium (natural abundance), the simulation agrees with measurement within 10 %. The extraction and analysis of concrete samples exceeds the time frame of the PhD thesis.

The tasks of this thesis were fulfilled by completing the design and optimization Monte Carlo studies for two irradiation facilities leading to their construction. The author also participated on the H4IRRAD commissioning and operation, mainly by simulations of the radiation fields inside the test areas. As an extra task the author prospered from his involvement in the H4IRRAD team and performed a measurement with a Medipix/Timepix detector, as well as comparison with simulations.

References

[1] S. Agosteo et al. *A facility for the test of large area muon chambers at high rates*. Nucl. Instr. and Meth. A 452 (2000) 94-104.

[2] The X5 Irradiation Facility.
URL: <http://sba.web.cern.ch/sba/BeamsAndAreas/GIF/irrad.html>

[3] Irradiation facilities at CERN. URL: <http://irradiation-facilities.web.cern.ch/irradiation-facilities/>

[4] The GIF++ Irradiation Facility. URL: <http://cern.ch/gifpp>

[5] M. Capeans et al. *A GIF++ Gamma Irradiation Facility at the SPS H4 Beam Line*. CERN-SPSC-2009-029 / SPSC-P-339: 1-12.
URL: <https://cds.cern.ch/record/1207380/files/SPSC-P-339.pdf>

[6] M. Brugger et al. "The CERN R2E Project". URL: <https://r2e.web.cern.ch/R2E/>

[7] M. Brugger, *Radiation Damage to Electronics at the LHC*. Conf. Proc. C1205201 (2012) 3734-3736, IPAC-2012-THPPP006.

[8] H4IRRAD, URL: <http://www.cern.ch/h4irrad>

[9] *Proceedings of the International workshop on Aging Phenomena in Gaseous Detectors*. Nucl. Instr. and Meth. A 515 (2003).

[10] M. Capeans-Garrido et al. *About aging of gas detectors: a compilation of some validation studies carried out for LHC*. CERN-PH-EP-TECH-NOTE-2009-002 (2009).

[11] M. Capeans, *Aging and materials: lessons for detectors and gas systems*. Nucl. Instr. and Meth. A 515 (2003) 73-88.

[12] M. Binkley et al. *Aging in large CDF tracking chambers*. Nucl. Instr. and Meth. A 515 (2003) 53-59.

[13] A. G. Holmes-Siedle and L. Adams, *Handbook of Radiation Effects; 2nd ed*. Oxford Univ. Press. Oxford (2002) 61-128. ISBN 019850733X, 9780198507338.

[14] A. G. Holmes-Siedle and V. A. J. van Lint, *Radiation Effects in Electronic Materials and Devices*. in: R. A. Meyers (Ed.), Encyclopedia of Physical Science and Technology (3rd ed.), Academic Press, New York (2003) 523-559, ISBN 9780122274107.

[15] ECSS-E-10-12, *Space Engineering: Methods for the calculation of radiation received and its effects, and a policy for design margins*. ESA Requirements & Standards Division, The Netherlands (2008) Draft v0.20, ISSN 1028-396X.

[16] A. Vasilescu, *The NIEL scaling hypothesis applied to neutron spectra of irradiation facilities and in the ATLAS and CMS SCT*. ROSE/TN/97-2. URL: <http://cern.ch/rd48>

[17] G. Lindström, M. Moll and E. Fretwurst, *Radiation hardness of silicon detectors – a challenge from high-energy physics*. Nucl. Instrum. Methods Phys. Res. A 426, (1999) 1-15.

[18] R. Gaillard, *Single Event Effects: Mechanisms and Classification*. in: M. Nicolaidis (Ed.), Soft Errors in Modern Electronic Systems, Frontiers in Electronic Testing, Springer (2011) 27-54, ISBN 978-1-4419-6992-7.

[19] ECSS-E-HB-10-12A, *Space Engineering: Calculation of radiation and its effects and margin policy handbook*. ESA Requirements & Standards Division, The Netherlands (2010).

[20] E. G. Stassinopoulos et al. *Charge generation by heavy ions in power MOSFET's, burnout space predictions, and dynamic SEB sensitivity*. IEEE Trans. Nucl. Sci. 39 (1992) 1704-1711.

[21] S. Duzellier, *Radiation effects on electronic devices in space*. Aerospace Science and Technology 9 (2005) 93-99, ISSN 1270-9638.

[22] K. Hajdas et al. *Radiation effects testing facilities in PSI during implementation of the Proscan project*. Radiation Effects Data Workshop, 2002 IEEE (2002) 516-523.

[23] PIF, URL: <http://pif.web.psi.ch/>

[24] K. Roeed et al. *Method for measuring mixed field radiation levels relevant for SEEs at the LHC*. RADECS 2011, IEEE (2011) 516-523, ISBN 978-1-4577-0587-8.

[25] CEA-VALDUC, URL: <http://www-dam.cea.fr>

[26] J. Morin and P. Zyromski, *The PROSPERO and CALIBAN neutron irradiation facilities*. RADECS 91, 1992 IEEE (1992) 574-576, ISBN 0-7803-0208-7.

[27] X. Jacquet et al. *Characterization of a fast to thermal neutron spectrum converter on PROSPERO reactor*. ANIMMA, 2009 IEEE (2009) 1-6, ISBN 978-1-4244-5208-8.

[28] G. Spiezia and X. Jacquet, *RADMON test - CEA*. CERN-EN-STI-EC-NOTE (2010).

[29] CNRAD, URL: <http://cngs-rad-facility.web.cern.ch>

[30] CNGS, URL: <http://proj-cngs.web.cern.ch/proj-cngs/>

[31] J. Mekki et al. *Mixed Particle Field Influence on RadFET Responses Using Co-60 Calibration*. IEEE Trans. Nucl. Sci. to be published (2013).

[32] G. Battistoni, S. Muraro, P. R. Sala, F. Cerutti, A. Ferrari, S. Roesler, A. Fasso, J. Ranft, *The FLUKA code: Description and benchmarking*. Proceedings of the Hadronic Shower Simulation Workshop 2006, Fermilab 6-8 September 2006, M. Albrow, R. Raja eds., AIP Conference Proceeding 896 (2007) 31-49.

[33] A. Ferrari, P. R. Sala, A. Fasso, and J. Ranft, *FLUKA: a multi-particle transport code (Program version 2008)*. CERN-2005-10, INFN/TC_05/11, SLAC-R-773 (2005).

[34] P.R. Sala et al. *The physics of the fluka code: Recent developments*. Radiation Effects Adv. Space Res., vol. 40, no. 9 (2007) 1339-1349, ISSN 0273-1177.

[35] A. B. Migdal, *Bremsstrahlung and pair production in condensed media at high energies*. Phys. Rev. 103 (1956) 1811-1820.

[36] D.E. Cullen et al. *EPDL97: the Evaluated Photon Data Library, '97 Version*. UCRL-50400, Vol. 6, Rev. 5 (1997).

[37] V.Vlachoudis, “FLUKA Advanced Graphical Interface”. URL: <http://www.fluka.org/FLAIR>

[38] V.Vlachoudis, *FLAIR: A Powerful But User Friendly Graphical Interface For FLUKA*. Proc. Int. Conf. on Mathematics, Computational Methods & Reactor Physics (M&C 2009), Saratoga Springs, New York (2009).

[39] C. Theis, K.H. Buchegger, M. Brugger, D. Forkel-Wirth, S. Roesler, H. Vincke, *Interactive three dimensional visualization and creation of geometries for Monte Carlo calculations*. Nucl. Instrum. Methods Phys. Res. A 562 (2006) 827-829.

[40] G4beamline, URL: <http://www.muonsinc.com/muons3/G4beamline>

[41] D. Forkel-Wirth and T. Otto, *Area Classification*. EDMS No. 810149, 2006.

[42] V. Clerc, *EHN1 GIF Assembly Shielding*. EDMS No. 1312173, 2013.

[43] B. Biskup et al. *Shielding Optimization for the New Gamma Irradiation Facility at CERN*. Submitted to Nucl. Instrum. Methods Phys. Res (2016).

[44] EHN1 Technical Drawings,
URL: <https://dfsweb.web.cern.ch/dfsweb/Services/DFS/DFSBrowser.aspx/Workspaces/s/SBA/NORTH/EHN1/Drawings/>

[45] B. Biskup et al. *Design and Operation of the H4IRRAD Mixed-Field Test Area at CERN*. Progress in Nuclear Science and Technology (PNST), vol.4 (2014) 218-222.

[46] K. Roeed et al. *FLUKA Simulations for SEE Studies of Critical LHC Underground Areas*. IEEE Transactions on Nuclear Science, 58, No. 3 (2011) 932-938.

[47] K. Roeed, M. Brugger, G. Spiezia. *An overview of the radiation environment at the LHC in light of R2E irradiation test activities*. CERN, 2011. CERN ATS-Note-2011-077 TECH.

[48] B. Biskup et al. *Commissioning and Operation of the H4IRRAD Mixed-Field Test Area*. CERN, 2011. CERN ATS-Note-2011-121 PERF.

[49] H. Vincke, C. Theis. *Airborne radioactivity development during and after beam operation in vented areas of accelerators*. CERN, 2015. CERN-RP-2015-046-REPORTS-TN v.1. EDMS No. 1511145 v.1.

[50] C. Theis et al. *Assessment of the impact of ^{110m}Ag on the activation of electronics boards in the CMS cavern*. CERN, 2009. CERN-DG-2009-104-RP-TN,
URL: <https://edms.cern.ch/file/1052205/1/CMS_electronics-part2.pdf>

[51] CERF Home Page, URL: <http://tis-div-rp-cerf.web.cern.ch/tis-div-rp-cerf/>

[52] S. Girod, *H4IRRAD Layout Drawings*, EDMS No. 1134001, 2011,
URL: <https://edms.cern.ch/document/1134001/2>

[53] H4IRRAD collaboration photos,
URL: <https://dfsweb.web.cern.ch/dfsweb/Services/DFS/DFSBrowser.aspx/Projects/R2E/H4IRRAD/Photos/>

[54] M.Calviani and M. Brugger, *Generic evaluation of residual dose rates and deposited energy for the proposed H4IRRAD and EAIRRAD targets*, EDMS No. 1134360, 2011,
URL:

<https://edms.cern.ch/file/1134360/2/H4IRRAD_EAIRRAD_target_activation_note_finc.pdf>

[55] I. Efthymiopoulos, *H4IRRAD Test Area in the EHN1 for LHC Components - Discussion on Intensity*, EDMS No. 1151181, June 2011, URL: <https://edms.cern.ch/file/1151181/1/ie-H4IRRAD_30Jun11.pdf>

[56] V. Agoritsas, *A Sealed Metal Argon Ionization Chamber (Argonion)*. IEEE Transactions on Nuclear Science, NS–28, No. 3, (1981).

[57] F.P. La Torre, G.P. Manessi, F. Pozzi, C.T. Severino, M. Silari, *Al activation experiment for the calibration of the CERF beam monitor*, CERN-DGS-2011-071-RP-TN, EDMS No. 1163587, 2011, URL: <https://edms.cern.ch/file/1163587/1/PIC_calibration_with_Al_foil.pdf>

[58] T. Wijnands, C. Pignard, R. Tesarek, *On line radiation monitoring for the LHC machine and experimental caverns*. CERN, 2006. CERN-TS-2006-009, URL: <https://edms.cern.ch/file/790663/1/TS-Note-2006-009.pdf>

[59] G. Spiezia et al. *The LHC accelerator Radiation Monitoring System – RadMON*. 10th International Conference on Large Scale Applications and Radiation Hardness of Semiconductor Detectors, PoS(RD11)024 (2012).

[60] C. Zamantzas et al. *The LHC Beam Loss Monitoring System Commissioning for 2010*. Evian 2010 Workshop on LHC Commissioning, Evian-les-Bains, France (2010) 57-66.

[61] K. Roeed et al. *Method for Measuring Mixed Field Radiation Levels Relevant for SEEs at the LHC*. IEEE Transactions on Nuclear Science, 59, No. 4 (2012) 1040-1047.

[62] Y. Thurel, V. Barbet and B. Favre, *R2E TE-EPC H4IRRAD 2011 Campaign Results*, EDMS No. 1158874, 2011, URL: <https://edms.cern.ch/file/1158874/1/R2E-TE-EPC_H4IRRAD-Test_Results.pdf>

[63] R2E Review, 21-24 Nov. 2011, CERN, URL: <https://indico.cern.ch/conferenceDisplay.py?confId=157386>

[64] S. Uznanski, *H4IRRAD Radiation Test – ST SPLargeUHD9 SRAM (HCMOS9 130nm)*, EDMS No. 1251607, 2012, URL: <https://edms.cern.ch/document/1251607/1>

[65] S. Uznanski, *H4IRRAD Radiation Test – 1-Wire DALLAS Communication*, EDMS No. 1251605, 2012, URL: <https://edms.cern.ch/document/1251605/1>

[66] S. Uznanski, *H4IRRAD Radiation Test – ADS1281 ADC*, EDMS No. 1251604, 2012, URL: <https://edms.cern.ch/document/1251604/1>

[67] S. Uznanski, *H4IRRAD Radiation Test – MAX5541 DAC*, EDMS No. 1251606, 2012, URL: <https://edms.cern.ch/document/1251606/1>

[68] R. Garcia Alia, B. Biskup et al. *SEU Measurements and Simulations in a Mixed Field Environment*. IEEE Transactions on Nuclear Science, 60, No. 4 (2013) 2469-2476.

[69] P. Mala, B. Biskup et al. *Thermoluminescent Detectors in Mixed Fields*. CERN, 2012. CERN ATS-Note-2012-086 TECH.

[70] P. Mala, B. Biskup et al. *Use of TL Detectors in Mixed Particle Energy Environment*. Presented at NEUDOS-12 (2013).

[71] X. Llopart et al. *Medipix2: a 64-k Pixel Readout Chip With 55-μm Square Elements Working in Single Photon Counting Mode*. IEEE Transactions on Nuclear Science, 49, No. 5 (2002) 2279-2283. doi:10.1109/TNS.2002.803788.

[72] CERN Medipix2 collaboration, URL: <http://www.cern.ch/medipix>

[73] Z. Vykydal et al. *Analysis of the Radiation Field in ATLAS Using 2008-2011 Data from the ATLAS-MPX Network*. CERN, 2013. CERN ATL-GEN-PUB-2013-001.

[74] J. Solc et al. *Comparison of Measurement and Simulation of ATLAS Cavern Radiation Background*. CERN, 2013. ATL-COM-GEN-2013-003.

[75] X. Llopart et al. *Timepix, a 65k programmable pixel readout chip for arrival time, energy and/or photon counting measurements*. Nucl. Instr. and Meth. A 581 (2007) 485-494.

[76] D. Turecek et al. *Pixelman: a multi-platform data acquisition and processing software package for Medipix2, Timepix and Medipix3 detectors*. Journal of Instrumentation 6 C01046 (2011).

[77] IEAP, CTU, URL: <http://www.utef.cvut.cz/en/>

[78] C. Lebel et al. *Energy calibration measurements of MediPix2*. Nucl. Instr. and Meth. A 591 (2008) 75-79.

[79] J. Jakubek, *Precise Energy Calibration of Pixel Detector Working in Time-Over-Threshold Mode*. Nucl. Instr. and Meth. A 633 (2011) 262-266.

[80] CMI, URL: <http://www.cmi.cz/?lang=2>

[81] B. Biskup et al. *Thermal Neutron Measurements by Timepix Detector in H4IRRAD at CERN*. Submitted to Nucl. Instrum. Methods Phys. Res (2016).

[82] VUHZ, a.s. URL: <http://vuhz.cz/pages/en/about-vuhz/about-vuhz/about-vuhz.php?lang=EN>

[83] S. Viswanathan, *ASM Handbook: Volume 15: Casting*. American Society of Metals, Materials Park, Ohio (2008) 785-795, ISBN 978-0871707116.

[84] S. H. Kosmatka, B. Kerkhoff, W. C. Panarese, *Design and Control of Concrete Mixtures*. Portland Cement Association (14th ed.), Skokie, Illinois (2002), ISBN 978-0893122171.

[85] Portland Cement Association. URL: <http://www.cement.org/>

Appendix A – H4 Beam Line Layout

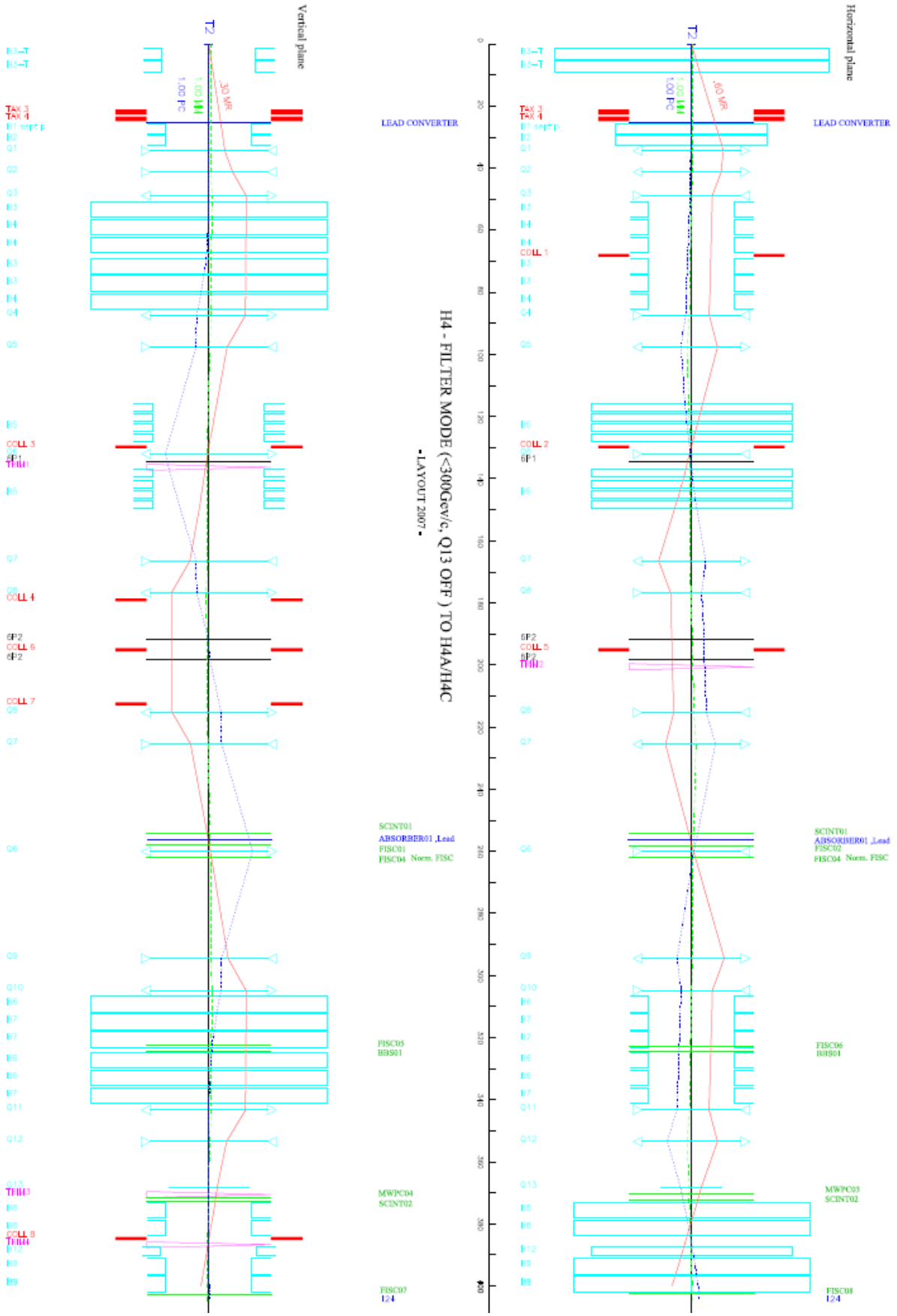

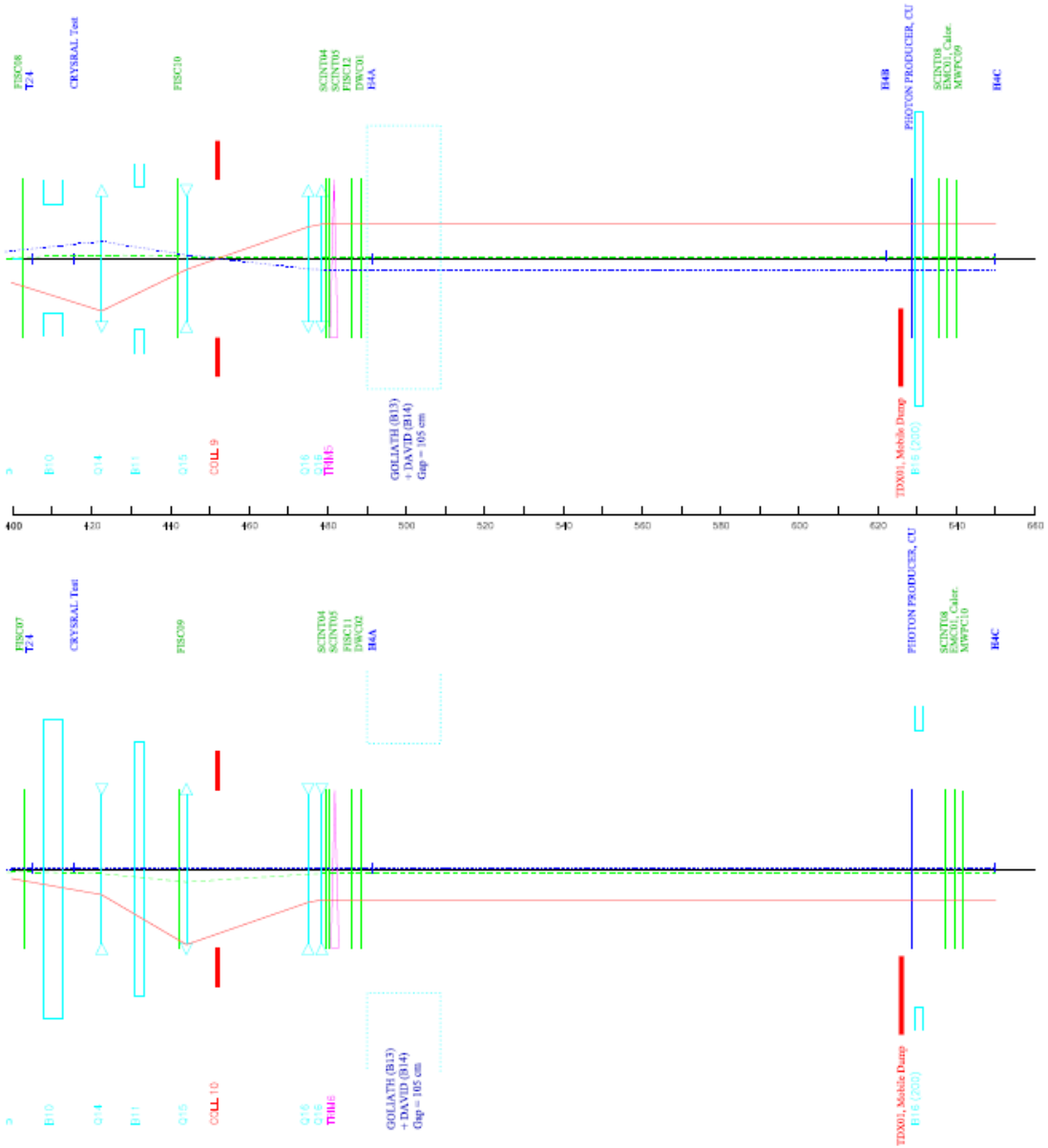

Filter Mode Optic (FM)

The Filter Mode Optics is the basis for all files presently being used for tests in the H4A and H4C area.
In the most used version the beam is parallell from the Q16 ownwards to the H4C area.

COLL 1 : Horizontal acceptance
COLL 2 : Horizontal intermediate focus
COLL 3 : Momentum definition (vertical) : ± 3mm →±1 ‰ Δp/p
COLL 6 : Vertical acceptance
COLL 8 : Vertical intermediate focus

20.00 MM
10.00 M

Le 19/02/07

Appendix B – RadMon Vertical Positions

The vertical views of the RadMon position during the 1st (blue) and 2nd (green) 2011 irradiation slots – the six vertical cuts (view from upstream) as indicated in Figure 52 [47].

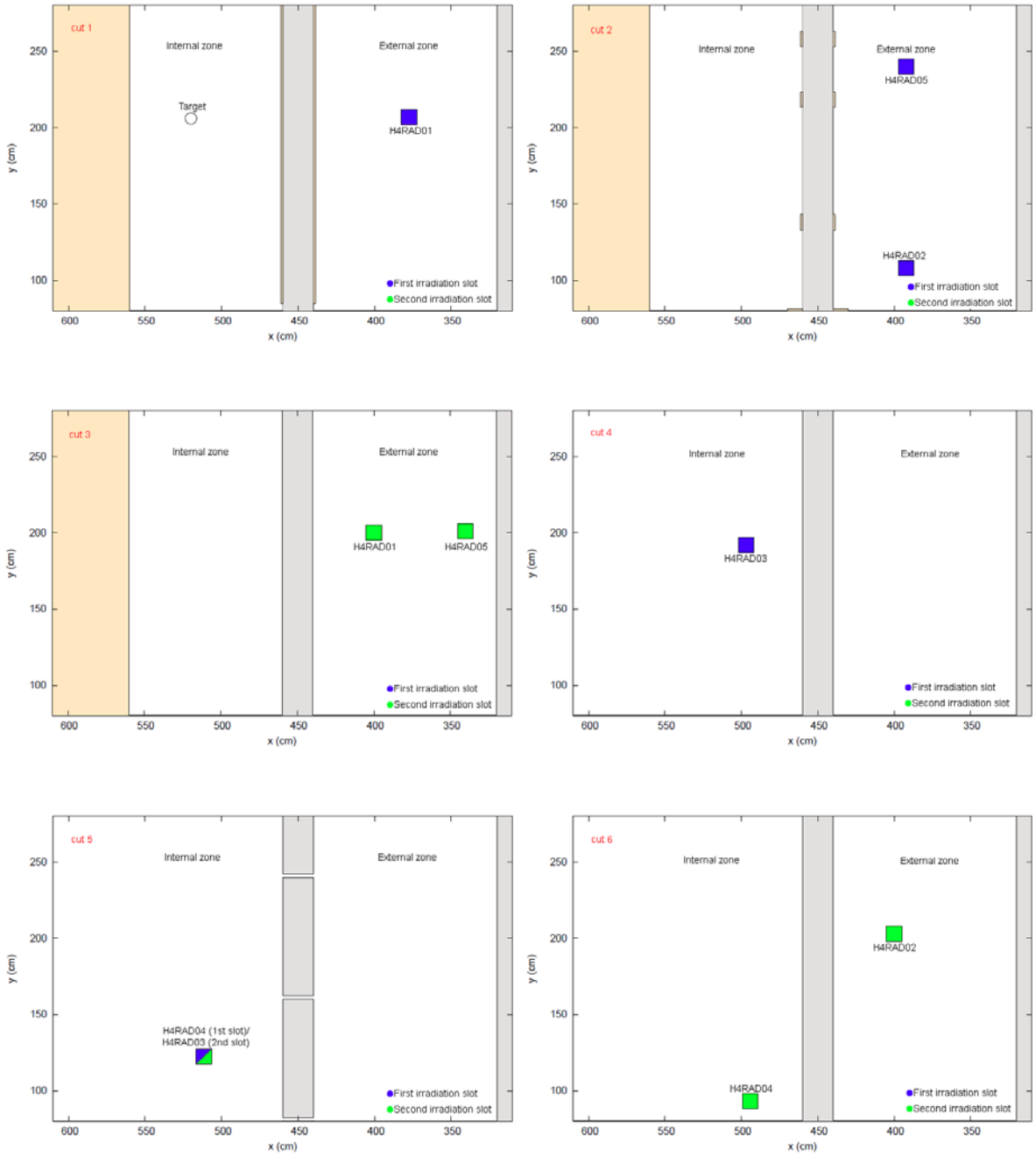

Appendix C – Equipment Vertical Positions

The vertical views of the equipment position during the 1st (left column) and 2nd (right column) 2011 irradiation slots – the 2×2 vertical cuts (view from upstream) as indicated in Figure 54 [47].

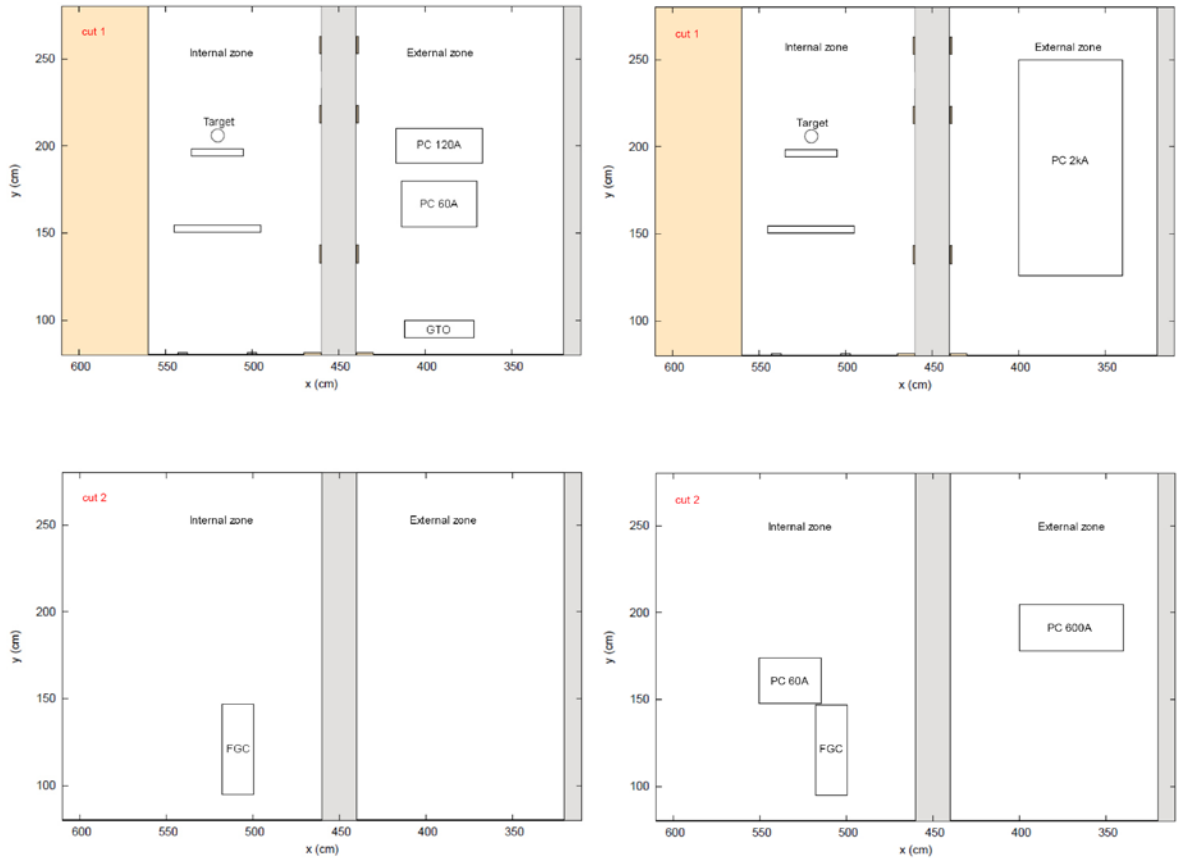

Appendix D – Equipment Positions

The horizontal (first left) and vertical views (from upstream) of the equipment position during the 3rd 2011 irradiation slot.

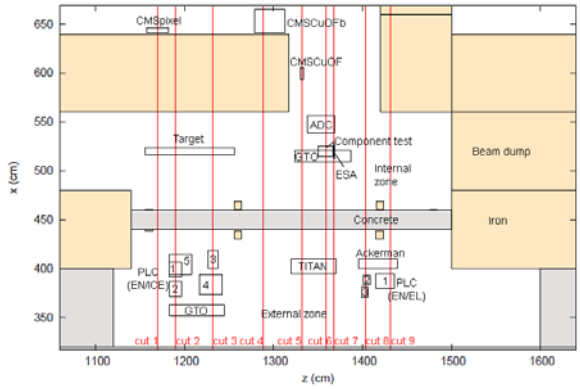

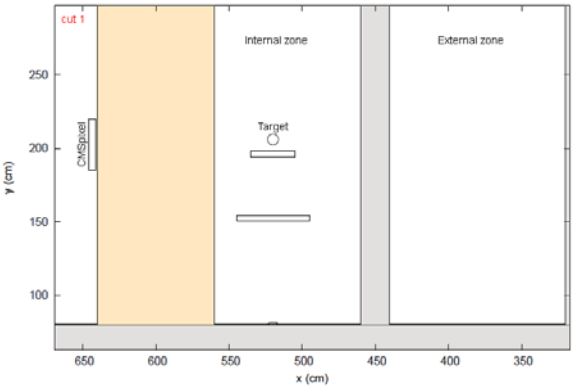

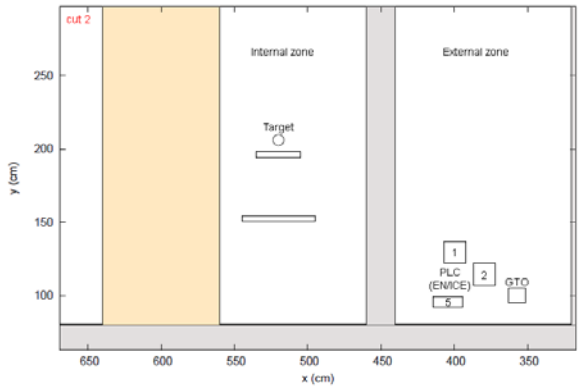

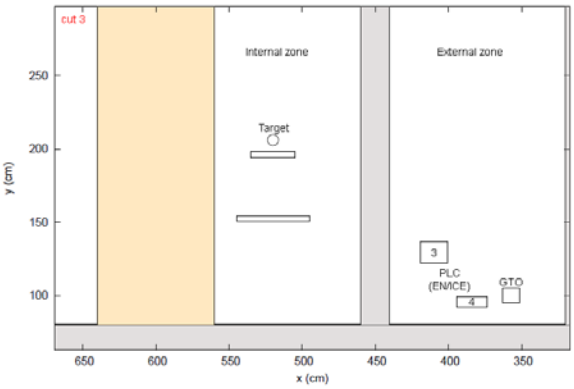

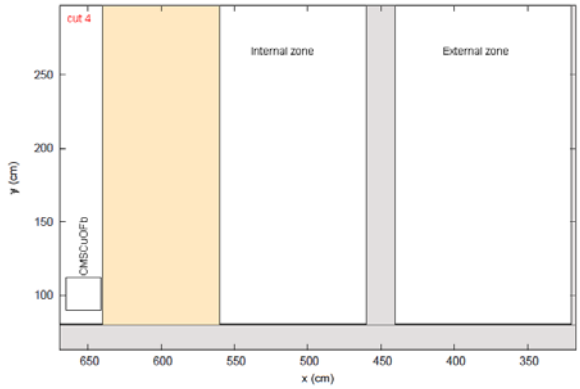

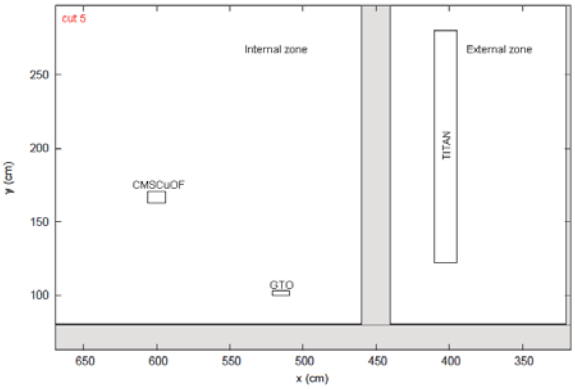

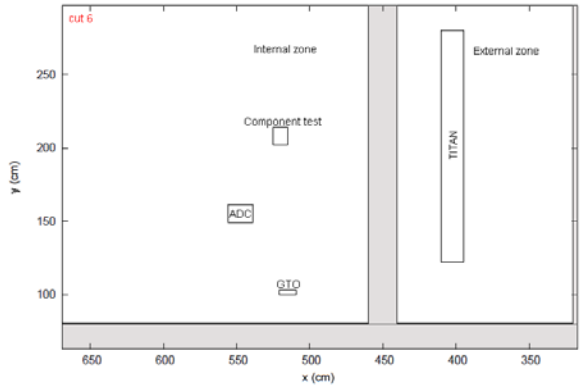
cut 6
Internal zone
External zone
Component test
TITAN
ADC
GTO
y (cm)
x (cm)

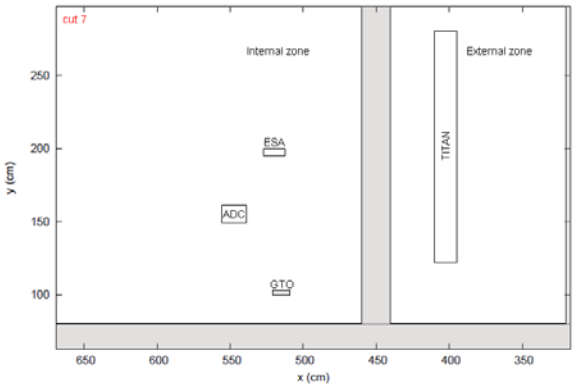
cut 7
Internal zone
External zone
ESA
TITAN
ADC
GTO
y (cm)
x (cm)

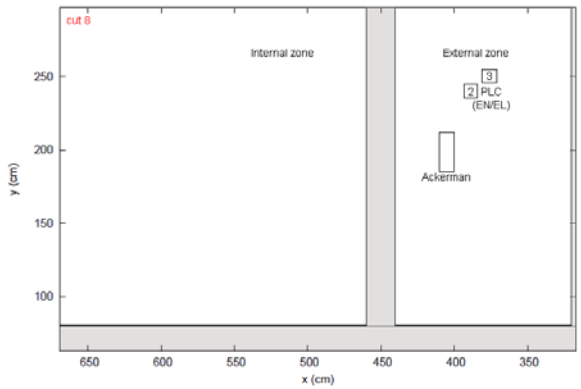
cut 8
Internal zone
External zone
3
2 PLC
(EN/EL)
Ackerman
y (cm)
x (cm)

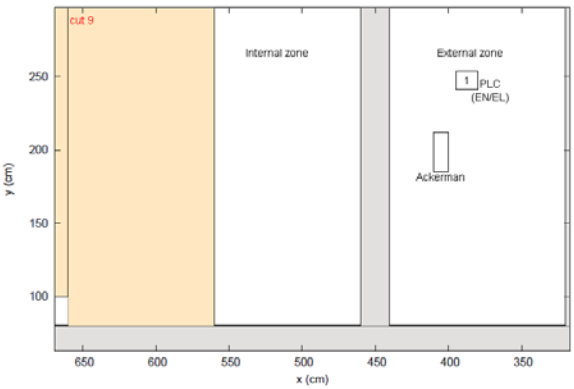
cut 9
Internal zone
External zone
1 PLC
(EN/EL)
Ackerman
y (cm)
x (cm)

Appendix E – Summary of tested equipment (2011 & 2012)

Year	Slot	Zone	Equipment
2011	1st	Int	Digital Controller (FGC) Converter Digital Electronic
		Ext	GTO (gate turn-off thyristor) Power Switch LHC60A-08V Air-Cooled Power Converter LHC120A-10V Air-Cooled Power Converter
	2nd	Int	Digital Controller (FGC) Converter Digital Electronic LHC60A-08V Air-Cooled Power Converter
		Ext	LHC4-6-8kA-08V Water-Cooled Power Converter (several Modules) LHC600A-10V Water-Cooled Power Converter
	3rd	Int	GTO Power Switch ADC ESA SEU Monitor RadMon Components CMS silicon pixel system CMS CuOF 2 units
		Ext	GTO Power Switch Schneider PLC system for cryogenics 5 units TITAN 400VAC Circuit Breakers with electronic protection Ackerman 48VDC Battery Charger Schneider Premium & Twido PLC 3 units
2012	1st	Int	ST SPLargeUHD SRAM 2 units 1-wire Dallas Communication Board Texas Instrument High-Resolution ADC ADS1218 3 units Maxim 16-bit DAC MAX5541 3 units CMS CuOF unit
		Ext	IGBT (insulated-gate bipolar transistor) Power Switch 2 units
	2nd	Int	CLIC components 5 units CLIC Digital DAC 3 units Volt. Reg. MIC 37302BR 3 units
		Ext	GTO Power Switch
	3rd	Int	BNL chip FGC 3 units FGClite prototype 3 units ADC 2 units SA Samsung chip 3 units ESE chip (CERN-designed RAM chip) USB repeater Montpellier SRAM 2 units
		Ext	UPS (uninterrupted power supply) 48V DC new commutation system TE/CRG equipment (Active magnetic bearing test) Montpellier SRAM 2 units EN-ICE equipment (Siemens PLC, M340 fieldtest + ethernet) RP components/samples

Appendix F – Shielding iron analysis report

VUHZ

LABORATOŘE A ZKUŠEBNY
Zkušební laboratoř č. 1053 akreditovaná ČIA
LABORATOŘ CHEMICKÁ A RADIOIZOTOPOVÁ

VÚHŽ a.s., se sídlem 739 51 Dobrá 240
vedená u KS v Ostravě, oddíl B, vložka 3030, IČ 27768953
tel.: 558 601 254 fax: 558 601 211 email: rehova@vuhz.cz

Protokol č. 8430/13

Zakázka č.: 625 513 144 **Objednávka č.:** 3520130119
Počet stran: 1 **Počet příloh:** 0

Objednatel: ČVUT, Ústav technické a experimentální fyziky, Praha, Ing. Biskup

Předmět zkoušení: 4 vzorky litiny
Datum převzetí vzorku 09. 08.2013
Datum a místo provedení zkoušky: 12.-29.08.2013, laboratoř chemická
Způsob odběru vzorků: Vzorky odebral zadavatel
Informace zadavatele o předmětu zkoušení: vzorky litiny ze stínění v CERNu
Požadavek: Stanovení obsahu C, S, Si, P, Mn, Cr, Ni
Popis metodiky zkoušení: Zkušební metody jsou uvedeny v tabulce výsledků .

Výsledky zkoušení:

Položka	Metoda	Rozměr	Označení vzorku			
			8430-1	8430-2	8430-3	8430-4
C	PP 621-1.1 (ČSN ISO 9556)	hm.%	2,26	2,31	2,40	2,09
S	PP 621-1.1 (ČSN ISO 4935)	hm.%	0,13	0,17	0,18	0,21
Si	PP 621-1.6 (ČSN 42 05 12)	hm.%	1,72	1,71	1,33	1,36
P	PP 621-1.4 (ČSN EN 10184)	hm.%	0,69	0,67	0,84	0,65
Mn	PP 621-1.3 (ČSN EN ISO 10700)	hm.%	0,41	0,48	0,25	0,33
Cr	PP 621-1.3 (ČSN EN10188)	hm.%	0,10	0,10	0,15	0,13
Ni	PP 621-1.3 (ČSN EN 10136)	hm.%	0,094	0,10	0,075	0,078

Výsledky zkoušení, uvedené v protokolu, se týkají pouze zkoušeného předmětu a jsou platné ve vztahu k popsané metodice zkoušení.

Protokol může zadavatel reprodukovat pouze jako celek, jinak jen s písemným souhlasem zkušebny.

Protokol vystaven dne: 29. srpna 2013
Vypracoval: Ing. Eva Řehová
Kontroloval: Ing. Roman Gabor

Schválil:
Ing. Karel Malaník, CSc.
ředitel Laboratoří a zkušeben

ZKUŠEBNÍ LABORATOŘE AKREDITOVANÉ ČIA
VÚHŽ a.s. DOBRÁ LABORATOŘE a ZKUŠEBNY
1053